EFFECTIVE HAMILTONIANS OF THE PYROCHLORE ANTIFERROMAGNET

A Dissertation

Presented to the Faculty of the Graduate School

of Cornell University

in Partial Fulfillment of the Requirements for the Degree of

Doctor of Philosophy

by

Uzi Hizi

August 2006

EFFECTIVE HAMILTONIANS OF THE PYROCHLORE ANTIFERROMAGNET

Uzi Hizi, Ph.D.

Cornell University 2006

The pyrochlore lattice Heisenberg antiferromagnet is a highly frustrated model, and possesses, classically, a macroscopic continuous ground state degeneracy. We study the semiclassical limit of large spin length S and examine the effect of quantum fluctuations on the energy within various theories. In each of these theories, we focus on deriving an effective Hamiltonian, as a function of a small number of degrees of freedom. The effective Hamiltonian gives us a simple formula for calculating the energy and facilitates the search for a unique ground state among the large number of classical ground states.

First, we consider the harmonic spin-wave theory, in which we keep only the lowest order (in $1/S$) correction to the classical Hamiltonian. We perform a detailed analysis of the harmonic order spin-wave modes and, using a real-space loop expansion, produce an effective Hamiltonian, in which the degrees of freedom are Ising variables representing products of the classical spin directions around loops in the lattice. We find a family of exactly degenerate collinear ground states, related by gaugelike Z_2 transformations and provide bounds for the zero-temperature entropy.

We carry the spin-wave calculation to the next –anharmonic– order in the $1/S$ expansion, utilizing a a self-consistent variational Hamiltonian approach, equiv-

alent to Hartree-Fock approximation. We find that the harmonic degeneracy is broken, but there remain a large number of seemingly degenerate ground states.

We develop an alternative approximation, employing the widely used, but not well controlled generalization of the $\mathrm{SU}(2) \cong \mathrm{Sp}(1)$ theory to $\mathrm{Sp}(N)$, in the limit of infinite N. We develop an effective Hamiltonian for this mean-field theory, using an analytical loop-expansion. We find that in this case, the ground state of the large-N theory cannot possibly be the physical ground state in the limit $S \gg 1$, since it is not a harmonic spin-wave ground states. Nonetheless, when restricted to the manifold harmonic spin-wave ground states, both the anharmonic spin-waves and the large-N theory result in similar effective Hamiltonian.

We further demonstrate that the harmonic theory can readily be applied to determine the harmonic-order ground state manifolds of the Heisenberg Hamiltonian on related lattices, and to field-induced collinear magnetization plateau states.

BIOGRAPHICAL SKETCH

The author was born on September 27, 1972, in Israel, the second of three children of Raya and Amnon Hizi. He spent his early years in Israel and in the United States, and went to high school in Tel-Aviv. After graduating from high school in 1990, he went on to study Mathematics and Physics at the Tel-Aviv University, where he received a B.Sc. in 1993. During the next four years, the author served in the army and concurrently took graduate courses in Physics at Tel-Aviv University. After being released from the army in 1997, the author spent a year completing his master's thesis under the supervision of David J. Bergman, earning an M.Sc. degree in 1998.

The subsequent years were spent working as a circuit designer at National Semiconductor's design center in Herzeliya, Israel. After three years at National, the author decided to return to graduate school to complete his Ph.D. He accepted an offer from Cornell University, and moved to Ithaca, with his family, in August of 2001. During his first year at Cornell, he joined the research group of Christopher L. Henley, with whom he has been working since.

The author is married to Sonia and has to sons, Eyal (born in December 2000) and Itai (born in August of 2003).

ACKNOWLEDGEMENTS

First and foremost, I would like to thank my advisor Christopher L. Henley, for his tireless help and guidance. I thank the members of my special committee Veit Elser and J. C. Davis for their insightful comments on my thesis and A exam questions. I would also like to thank the original members of my special committee Carl Franck, Jim Sethna and Don Hartill. During the past few years I enjoyed conversations with many Cornell faculty members, most notably Rob Thorne and Piet Brouwer. I am indebted to David J. Bergman of Tel-Aviv university for his advice during my master's studies, as well as useful advice on pursuing Ph.D. studies.

I would like to thank Prashant Sharma for insightful conversations and collaboration in the work included here. Of the many graduate students and postdocs with whom I interacted during my years at Cornell, I would like to particularly thank Yuval Yaish, Mikhail Polianski, Siew Ann Cheong, Shaffique Adam, Dan Goldbaum, Stephan Braig, and Saar Rahav.

I acknowledge the physics department, particularly John Miner and Deb Hatfield, for TA appointments and the NSF for financial support, under grant grant DMR-0240953.

TABLE OF CONTENTS

LIST OF TABLES

LIST OF FIGURES

LIST OF SYMBOLS

Symbol	Description.
$\langle ij \rangle$	Nearest neighbors
$\langle \sigma\sigma \rangle$	Correlation function.
a, b, ...	Complementary lattice site index (Ch. 5).
i, j, ...	Lattice site index.
α, β, ...	Simplex (diamond) lattice site index.
x, y, z	Real space (lattice) coordinates.
x, y, z	Coordinates of spin directions.
$\tilde{x}$, $\tilde{y}$, $\tilde{z}$	Local coordinates for spin operators.
M_{ij}	Element of any matrix $\mathbf{M}$
v_i	Element of any vector $\mathbf{v}$
$a_i^\dagger$, a_i	Holstein-Primakoff boson operators.
$\mathbf{a}^\dagger$, $\mathbf{a}$	Vector of Holstein-Primakoff boson operators.
A	Arbitrary parameter used in the expansion of Eq. (4.4).
A_{ij}	Sp(N) bond operators (Ch. 7).
$A_l(S)$	Coefficients in gauge-invariant effective quartic Hamiltonian (6.51).
$b_m^\dagger$, b_m	Spinon creation and annihilation operators.
$b_{i\sigma}^\dagger$, $b_{i\sigma}$	Schwinger boson operators.
$b_{i\sigma,m}^\dagger$, $b_{i\sigma,m}$	Generalized Sp(N) Schwinger boson operators (Ch. 7).
$\mathbf{b}^\dagger$, $\mathbf{b}$	Vector of Schwinger boson operators $b_{i\sigma,m}^\dagger$, $b_{i\sigma,m}$.
$\mathcal{B}$	Complementary lattice effective Hamiltonian "field" term (Ch. 5).
$\vec{B}$	Magnetic field (in Ch. 5).
B_{ij}	Ferromagnetic bond operators in large-N theory (Sec. 7.6).
c_m	Generalized norm of $\mathbf{v}_m$.
C_n	Coefficients in the loop expansion (4.4).
C_G^m	Projection of transformation G onto divergent mode m (Sec. 4.3).
$C(\varepsilon)$	Divergent fluctuation coefficient (Sec. 6.2.2).
$D_{\mathbf{q}}(\varepsilon, \delta)$	Trigonometric function in Sec. 6.2.
$E_{\text{harm}}^{\text{eff}}$	Effective harmonic zero-point spin-wave energy.
E_0	Spin-wave effective Hamiltonian constant term.
$\mathcal{E}_0$	Complementary lattice effective Hamiltonian constant term.
E_{MF}	Mean-field energy.
E_{cl}	Classical energy.
E_{harm}	Harmonic zero-point spin-wave energy.
E_{quart}	Quartic spin-wave energy.
$\overline{E}_{\text{quart}}$	Average quartic spin-wave energy among harmonic ground states.
E_q	Quantum part of energy in large-N theory (Ch. 7).
E_q^{eff}	Effective functional for quantum part of large-N energy E_q.
f_k, $\tilde{f}_k$	Combinatoric functions in spin-wave loop expansion (App. A).
$F(2m)$	Combinatoric functions in large-N loop expansion (App. A).
$\mathcal{F}, \mathcal{G}$	Generating functions in App. A.

Symbol	Description
g_k, $\tilde{g}_k$	Combinatoric functions in spin-wave loop expansion (App. A).
$G(2l, 2m)$	Combinatoric functions in large-N loop expansion (App. A).
$\mathbf{G}$, G_{ij}	Matrix of spin-mode fluctuations $G_{ij} = \langle \sigma_i^x \sigma_j^x \rangle = \langle \sigma_i^y \sigma_j^y \rangle$.
h_i	Local exchange field (Ch. 1).
$\mathcal{H}$	Hamiltonian.
$\mathcal{H}_{\rm cl}$	Classical Hamiltonian/energy.
$\mathcal{H}_{\rm harm}$	Harmonic spin-wave Hamiltonian/energy.
$\mathcal{H}_{\rm quart}$	Quartic order spin-wave Hamiltonian.
$\mathbf{H}$	Diagonal blocks in block-diagonal form of harmonic spin-wave Hamiltonian for collinear spins.
$H_{\rm MF}$	Mean-field Hamiltonian.
$i(\alpha, \beta)$	Lattice site shared by simplexes α, β.
J	Nearest neighbor coupling.
$\mathbf{J}$	Matrix of coupling.
$\mathcal{J}$, $\mathcal{J}'$, $\mathcal{J}_3$	Complementary lattice effective Hamiltonian "coupling" terms.
K_l	Spin-wave effective Hamiltonian (4.6) coefficients.
$\mathcal{K}_l$	Large-N effective Hamiltonian (7.15) coefficients.
L	Linear dimension of system, measured in units of the underlying cubic lattice constant.
$\mathbf{L}_\alpha$	Simplex spin operator.
$\mathcal{L}$	Arbitrary lattice loop.
M	Magnetization of each simplex, when magnetic field is applied.
$\mathbf{M}$	Hessian matrix, defined in Eq. (4.25).
N	Number of Sp(N) flavors.
N_s	Number of lattice sites.
N_s^c	Number of complementary lattice sites (Ch. 5).
N_M	Number of sites in magnetic lattice.
N_B	Number of sites in Bethe lattice.
N_z	Number of zero modes.
$n_{\rm div}$	Dimension of the divergent mode linear space.
$n_{\rm even}$	Dimension of the linear subspace of even divergent modes.
$\mathcal{N}_0$	The number of degenerate ground states.
$\mathcal{N}_{\rm even/odd}^{\rm (ref)}$	Number of even and odd gaugelike transformations on an arbitrary reference state.
$\mathcal{N}_G^{\rm (ref)}$	Number of possible gauge transformation on reference state.
$\mathbf{n}_i$	Classical spin direction (unit vector).
$\mathbf{P}$	Off-diagonal blocks in harmonic spin-wave Hamiltonian matrix for general (non-collinear) spins (Eq. (2.9)).
$\mathcal{P}_{2l}$	Loop variables in the anharmonic effective Hamiltonian (6.53).
$\tilde{\mathcal{P}}_{2l}$	Loop variables that go into large-N effective Hamiltonian (7.15).
$\mathbf{q}$	Brillouin zone vector.
$\mathbf{Q}$, Q_{ij}	Hubbard-Stratonovich bond field matrix and elements (Ch. 7).
Q_{ij}^c	Saddle-point (classical) value of Q_{ij}.

Symbol	Description
$\mathbf{R}^{\tilde{x}}$, $\mathbf{R}^{\tilde{y}}$	Diagonal blocks in harmonic spin-wave Hamiltonian matrix for general (non-collinear) spins (Eq. (2.9)).
$\mathbf{R}$, R_{ij}	Hubbard-Stratonovich bond field matrix and elements (Ch. 7).
R_{ij}^c	Saddle-point (classical) value of R_{ij}.
S	Spin length.
S_d	Support of a divergent mode $\mathbf{u}_d$.
$\mathbf{S}_i$, $S_i^{\pm}$	Spin operators, on site i.
$S(\mathbf{q})$	Neutron diffraction structure factor.
$S^{\perp}$	Spin component transverse to neutron diffraction wavevector.
$\mathbf{u}_m$	Simplex lattice spin-wave modes (i.e. eigenvalues of $\boldsymbol{\eta}\mathbf{W}^{\dagger}\mathbf{W}$).
$\mathbf{U}$	Unitary transformation matrix.
$\mathbf{v}_m$	Spin-wave modes = eigenvectors of $\boldsymbol{\eta}\mathbf{H}$.
$\mathbf{W}$	$N_s \times N_s$ matrix relating lattice sites to simplexes.
$\mathbf{w}_m$	Divergent spin-wave modes.
$x_{i\sigma}$	Expectation value of condensed boson operator $b_{i\sigma,1}$, in large-N theory (Ch. 7.
x	Variable of generating function.
z	Lattice coordination.

Symbol	Description
$\alpha_{\rm even}(i)$, $\alpha_{\rm odd}(i)$	Even (odd) tetrahedron to which site i belongs.
$\alpha_{\mathbf{q}}$, $\beta_{\mathbf{q}}$, $\gamma_{\mathbf{q}}$	Trigonometric functions (Ch. 6.2).
β	Inverse temperature in Metropolis algorithm (App. C.3).
Γ_{ij}	Bond variables (Ch. 6).
$\Gamma_{ij}^{(1)}$,$\Gamma_{ij}^{(2)}$	Two leading order terms in Γ_{ij}.
δ, ε	Variational parameters (Ch. 6).
$\boldsymbol{\Delta}_l$	Basis vector within the magnetic unit cell.
η_i	Ising variable labeling direction of collinear spins.
$\boldsymbol{\eta}$	Matrix of Ising variables defined in Eq. (2.14).
$\eta_{\alpha\beta}$	When α, β are next-nearest neighbor simplexes, with bond (ij) between them: $\eta_{\alpha\beta} = \eta_i\eta_j$.
$\tilde{\eta}_a$	Complementary lattice Ising variables (defined in (5.1).
θ_i	Spherical angle of classical spin direction.
$\theta_{\alpha\beta}$	For coplanar spins, when α, β are next-nearest neighbor simplexes, with bond (ij) between them: $\theta_{\alpha\beta} = \theta_i - \theta_j$.
κ	Generalized spin length ($\kappa = 2S$) in large-N theory.
λ_m	Eigenvalues of $\boldsymbol{\eta}\mathbf{H}$.
λ_i	Lagrange fields in Sp(N) theory (Ch. 7).
λ^c	Saddle-point (classical) value of λ_i.
$\boldsymbol{\Lambda}$	Diagonal matrix with elements $\delta_{ij}\lambda_i$
$\boldsymbol{\mu}$	$N_s/2 \times N_s/2$ matrix whose elements are defined in (4.2).
$\boldsymbol{\xi}_{lm}$	Vector connecting neighbors from sublattices l and m.
ρ_z	Fraction of z-polarized checkerboard "tetrahedra" (Sec. 6.2).
$\rho(\lambda)$	Tight bonding density of states (Sec. 4.1.1).
σ	Index to Schwinger boson flavor $\sigma \in \{\uparrow, \downarrow\}$.
$\vec{\sigma_i}$	Spin deviation operators at site i.
$\vec{\sigma_{\mathbf{r}}^l}$	Spin deviation operators at lattice vector $\mathbf{r}$, sublattice l.
$\vec{\sigma_{\mathbf{q}}^l}$	Fourier transformed pin deviation operators.
$\vec{\boldsymbol{\sigma}} = (\boldsymbol{\sigma}^x, \boldsymbol{\sigma}^y)^T$	Vector of spin deviation operators.
$\boldsymbol{\tau}$	Gaugelike transformation vector, defined on simplex lattice [$\tau(\alpha) = \pm 1$].
$\boldsymbol{\tau}_{\rm even/odd}$	Even and odd gaugelike transformations.
$\overline{\tau}$	Inverse of gaugelike transformation.
ϕ_i	Spherical angles of classical spin direction.
ϕ_{ij}	$\phi_i - \phi_j$.
φ_{ij}	Argument of Q_{ij} (Ch. 7).
Φ_i	U(1) gauge field in large-N theory.
Φ_{2l}	Sum of fluxes of loops of length $2l$, defined in Eq. (4.7).
$\Psi_{\rm var}$	Variational wavefunction (Ch. 6).
$\boldsymbol{\Psi}_m$	Vector of Schwinger boson operator after unitary. transformation, defined in Eq. (7.27).
ω_m	Frequencies associated with spin-wave mode $\mathbf{v}_m$.

Chapter 1

Introduction

1.1 Geometrical frustration

In recent years, there have been many theoretical studies of geometrically frustrated systems [1, 2, 3]. These are systems in which not all of the spin bonds can be satisfied simultaneously, due to the connectivity of the lattice. The frustration may lead to unconventional magnetic ordering, or even to a complete absence of long-range order.

In general, an antiferromagnetic model on any lattice that includes triangular loops is frustrated. Since each spin would like to be opposite to both its neighbors, not all of the bonds can be satisfied simultaneously. Consider, for example, the triangular lattice. An Ising model on this lattice would have, as a ground state, any configuration in which each triangle has two spins of the same kind, i.e., $\uparrow\uparrow\downarrow$ or $\uparrow\downarrow\downarrow$. It is easy to see that there is a *macroscopic* degeneracy of such ground states, i.e., the number of ground states $\mathcal{N}_0$ is exponential in N_s, the number of sites, and the *residual entropy* (at zero temperature), defined as $\ln \mathcal{N}_0$ is *extensive*. Suppose, on the other hand, that we consider the classical x-y model or the classical Heisenberg model

$$\mathcal{H} = \sum_{ij} J_{ij} \mathbf{S}_i \cdot \mathbf{S}_j \,, \tag{1.1}$$

where $J_{ij} = 1$ for nearest neighbors $\langle ij \rangle$. and $\mathbf{S}_i$ is a spin at site i (of two or three dimensions, for the x-y or Heisenberg model, respectively). Here we we find that, up to global spin rotation and lattice symmetries, there is one unique ground state on the triangular lattice, a state in which the spins are *coplanar* and are at

120° angles to each other. Thus, although not all bonds are satisfied, there is one unique ground state. In the following, we will focus on *highly frustrated models* – models in which the frustration leads to a massive ground state degeneracy.

Models that lead to strong frustration are nearest-neighbor antiferromagnets on *bisimplex* [4] lattices composed of corner sharing *simplexes* [5, 4]. Examples include the two-dimensional kagomé and three-dimensional garnet lattices, each composed of triangular simplexes, and lattices composed of corner sharing "tetrahedra": the two-dimensional checkerboard, layered SCGO [2], and three-dimensional pyrochlore.

In bisimplex models, the Heisenberg Hamiltonian (1.1), can be recast in the form

$$\mathcal{H} = \frac{1}{2} \sum_{\alpha} |\mathbf{L}_\alpha|^2 + \text{const.}\,, \tag{1.2}$$

where $\mathbf{L}_\alpha \equiv \sum_{i \in \alpha} \mathbf{S}_i$, is an operator that resides on a simplex α (we reserve Greek indices for simplexes - and roman indices for the spin sites). Alternatively, α is a site on the lattice composed of the centers of the simplexes, e.g., a triangular lattice for the kagomé case, and $\mathbf{L}_\alpha$ is a spin operator acting on the sites of that lattice.

The classical result is a macroscopic continuous degeneracy among all states satisfying

$$\mathbf{L}_\alpha = 0\,. \tag{1.3}$$

for all α. The entropy associated with the degeneracy is extensive.

Much of the theoretical work on such highly frustrated models has been aimed at the extreme quantum limit, of $S = 1/2$ [6, 7, 8, 9, 10, 11, 12, 13], in hopes of understanding the nature of the disordered spin states and in search of exotic new states of matter. We, on the other hand, focus on the semiclassical $S \gg 1$ regime.

Given the large classical degeneracy, one would like to know what physical mechanisms can break the degeneracy and choose a unique ground state. In experimental system, one usually finds that there are either lattice distortions [14, 15] [that break the symmetry of the lattice – vary J_{ij} along different directions] or additional interactions, including dipolar interaction [16], Dzyaloshinsky-Moriya interaction [17, 18], and spin-orbit interactions, due to orbital ordering [19, 20, 14] or single-ion anisotropies [15]. Nevertheless, it is still a valid question to ask: what is the ground state of the pure, undistorted Heisenberg model on one of these lattices? The answer is rather counterintuitive: it turns out that often ordering can be induced by classical thermal fluctuations, or (zero temperature) quantum zero-point fluctuation, a phenomenon known as *order due to disorder* [21, 22].

Among the bisimplex lattices, the most studied theoretically has been, until recently, the kagomé lattice (shown in Fig. 1.1) [23, 24, 25, 26, 27, 28, 29, 30]. In the Heisenberg model on this lattice, thermal fluctuations have been shown to favor a coplanar state –the so-called $\sqrt{3} \times \sqrt{3}$ state (shown in fig. 1.1) [24, 26]. In the zero temperature *semiclassical* (i.e. spin length $S \gg 1$) case, one only considers the lowest order, in $1/S$, quantum correction to the classical energy. The result is a harmonic *spin-wave* theory, and in the kagomé case it turns out that *all* coplanar configurations are exactly degenerate *harmonic ground states*.

Why are the coplanar states preferred by quantum fluctuations? A general argument can be given to suggest that in many frustrated lattices the ground states should actually be *collinear* [31, 32, 22]: each spin $\mathbf{S}_i$ feels the effects of a local field due to its neighbors $\mathbf{h}_i = \sum_j J_{ij}\mathbf{S}_j$. The classical ground state is such that all spins align with the local exchange field $\mathbf{h}_i \parallel \mathbf{S}_i$. Now, once fluctuations are considered, each spin deviates from its ground state direction by $\delta\mathbf{S}_i \perp \mathbf{S}_i$,

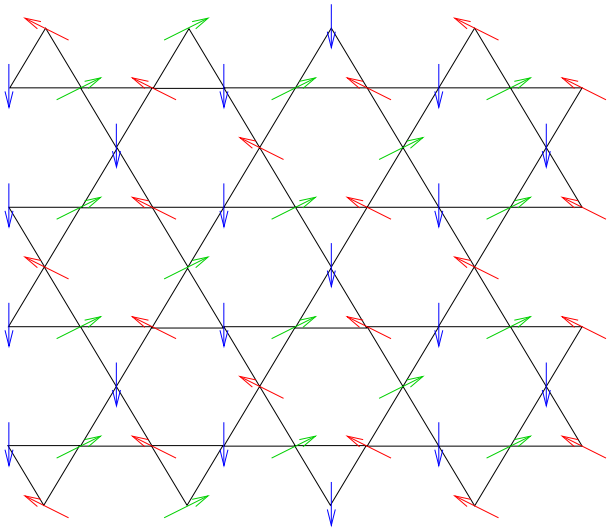

Figure 1.1: The $\sqrt{3} \times \sqrt{3}$ kagomé state

and the local field changes by $\delta \mathbf{h}_i = \sum_j J_{ij} \delta \mathbf{S}_j$ Since each spin would like to be aligned with the direction of the local magnetic field, then it is preferred to have $\delta \mathbf{h}_i \parallel \delta \mathbf{S}_i$. Since the deviations of $\mathbf{S}_i$ and $\mathbf{h}_i$ are perpendicular to the classical directions, the result is that quantum fluctuations prefer collinear classical ground states. [A similar argument can also be given for classical thermal fluctuations.]

In the kagomé lattice, though, due to the odd number of spins in a simplex, there is no way of satisfying the constraint (1.3) with collinear spins. The kagomé system settles for the next best thing: the spins align in a coplanar configuration.

To break the harmonic degeneracy in the kagomé model, one has to go on to higher orders in the $1/S$ expansion. The results of self-consistent anharmonic calculations have been that the $\sqrt{3} \times \sqrt{3}$ state is the unique zero temperature large-S ground states [29, 30, 33].

An established alternative to the spin-wave approach is to generalize the Heisenberg spins [with SU(2) $\cong$ Sp(1) symmetry] to Sp(N) symmetry [34, 35]: here N is

the number of flavors of Schwinger bosons whose bilinear form represents a *generalized spin* [34, 35], with length $\kappa = 2S$. The resulting mean-field theory (valid in the $N \to \infty$ limit) is popular as an analytic approach to the $S = 1/2$ limit, since the *small-*κ limit captures various disordered and exotic ground states [34, 35, 36]. The large-N mean-field theory is also useful for *large-*κ (large-S) problem, because it gives a simple analytical prescription for ground state selection: unlike the spin-wave expansion, here all degeneracies are (typically) broken at the lowest order [$\mathcal{O}(1/\kappa)$] quantum correction [28, 34, 35]. This method has been applied to the kagomé case, at about the same time as the anharmonic spin-wave theory [28], and resulted in the same $\sqrt{3} \times \sqrt{3}$ ground state.

1.2 The pyrochlore antiferromagnet

The pyrochlore lattice, in which the centers of the tetrahedra form a diamond lattice[1] (see Fig. 1.2), is of interest because it is realized in many experimental systems, in both $A_2B_2O_7$ oxides and in B sites of AB_2O_4 spinels [37], and because, by the analysis of Ref. [38], bisimplex lattices composed of tetrahedra are less susceptible to ordering than lattices with triangle simplexes. In fact, the prevailing view is that thermal fluctuations do not facilitate ordering [39, 38] in this lattice.

Because of the tetrahedron simplexes (with even number of spins) in the pyrochlore, the classical spin configurations can satisfy the constraint (1.3) and also be collinear, and therefore, by the arguments given before, one expects that the states preferred by quantum (or thermal) fluctuations would be collinear. In recent work, Henley has demonstrated [40] that the classical degeneracy is not fully

[1] Alternatively, the lattice may be viewed as an FCC lattice of disjoint tetrahedra.

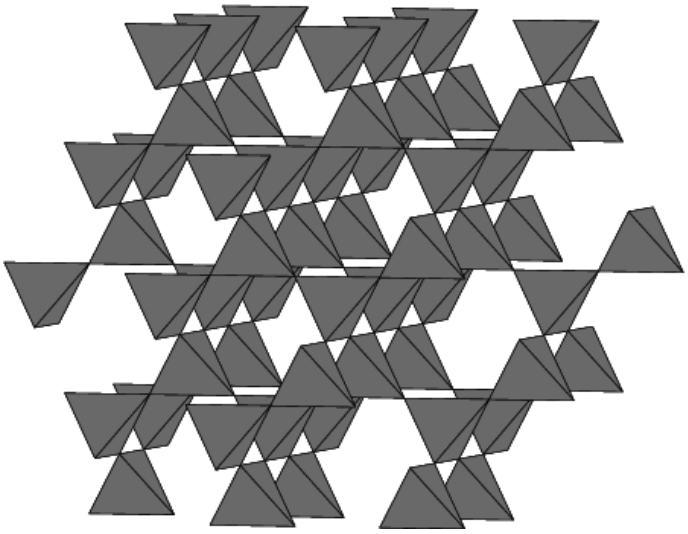

Figure 1.2: The pyrochlore lattice

lifted by the lowest order (in $1/S$) non-interacting spin-wave theory, assuming a collinear spin arrangement. Here we recover this result using the more rigorous Holstein-Primakoff transformation, and provide a detailed study of various aspects in the linear spin-wave theory, as well as a study of the anharmonic spin-waves and of a large-N mean field theory.

Lately, there have been various works designed to search for a ground state of the pyrochlore in the large-S limit. These include work on two-dimensional analogs of the pyrochlore [41, 42] (see also Sec. 5.2) and on ground state selection due to lattice distortions and spin-orbit coupling in Vanadium spinels [19, 20, 15]. Another body of work is on the closely related problem of the ordering in the pyrochlore in the presence of a magnetic field, which allows, at a special value of the field, a collinear pattern with nonzero magnetization [43, 44, 45] (see also Sec. 5.1).

We note that, beyond a search for the large-S ground states, our results can

serve as a starting point for a study of intermediate values of S, by allowing for tunneling among the various semiclassical ground states, with appropriate tunneling matrix elements. The result could be a selection of one particular ground state to a mixture of superposition of several ordered states, or to disorder [44, 46].

1.3 Outline

The rest of this thesis is organized as follows: In Ch. 2 we derive the large-S expansion of the Hamiltonian (1.1):

$$\mathcal{H} = \mathcal{H}_{\rm cl} + \mathcal{H}_{\rm harm} + \mathcal{H}_{\rm quart} + \cdots , \tag{1.4}$$

where $\mathcal{H}_{\rm cl}$ is the classical Hamiltonian , of order S^2, $\mathcal{H}_{\rm harm}$ is the harmonic, non-interacting spin-wave, Hamiltonian (of order S) and $\mathcal{H}_{\rm quart}$ is the next order [$\mathcal{O}(1)$] interaction term [47]. We diagonalize the harmonic part of the expansion, assuming fluctuation around a *collinear* classical ground state, where each state can be parameterized by an Ising variable $\eta_i = \pm 1$ on each lattice site, such that $\mathbf{S}_i = \eta_i \hat{z}$.

In Ch. 3 we study the properties of the various spin-wave modes: *zero modes* that do not contribute to the zero-point energy, *non-zero modes* that can be expressed entirely in terms of the diamond lattice sites, and *divergent zero modes* that carry divergent fluctuations. We use this formalism to demonstrate a key result of Ref. [40]: that collinear classical ground states related by Ising *gaugelike* transformations are exactly degenerate.

In Ch. 4 we consider the zero-point energy of the harmonic fluctuations and derive an *effective Hamiltonian* [4], where we parameterize the energy only in terms *flux* variables (using the terminology of Ref. [41]) through all *loops* in the diamond lattice (where the pyrochlore spins sit bond centers). The flux $\varphi_{\mathcal{L}}$ through a loop

$\mathcal{L}$ with bond centers at $(i_1, i_2, \ldots, i_n)$ is defined as

$$\varphi_{\mathcal{L}} = \eta_{i_1}\eta_{i_2}\eta_{i_3}\cdots\eta_{i_n}\,. \tag{1.5}$$

And the effective harmonic-order zero-point energy is found to be

$$E^{\text{eff}}_{\text{harm}} = E_0 + K_6\Phi_6 + K_8\Phi_8 + \cdots\,, \tag{1.6}$$

where K_n are numerical coefficients that we evaluate using a real-space *loop expansion*, and Φ_n are sums of the fluxes $\varphi_{\mathcal{L}}$ through all loops of length n.

$$\Phi_n \equiv \sum_{|\mathcal{L}|=n} \varphi_{\mathcal{L}}\,. \tag{1.7}$$

We numerically evaluate the zero-point energy of a large number of collinear classical ground states and find that the effective Hamiltonian does a good job of evaluating the energy with just a few terms. We find a family of ground states and obtain bounds for the residual entropy, using a correspondence between gaugelike transformations and divergent zero modes. In Sec. 4.4 we argue that the collinear states have lower energy than closeby non-collinear states obtained by rotating loops of spins out of collinearity, thereby making the assumption of collinearity plausible. However, we have not been able to rigorously prove that within the space of all classical ground states, the global energy minimum must occur at a collinear state.

In Ch. 5 we apply the loop expansion to some closely related models including the case of non-zero magnetization plateaus and other lattices. We find that the effective Hamiltonian approach is useful in predicting the ground states in many cases.

In Ch. 6 we go beyond the harmonic approximation to the next order in the Holstein-Primakoff spin-wave expansion. We derive a mean field theory for the

anharmonic Hamiltonian, and apply it to both the checkerboard lattice and the pyrochlore. Although most of the degeneracy is broken, there remain a large family of harmonic ground states that remain, within our numerical precision, degenerate at all (large) values of S. We do not know whether this degeneracy is exact.

In Ch. 7 we employ a different mean field theory, the large-N Sp(N) theory. This is a widely used method that is believed to capture the physics of frustrated systems. In particular, the common lore is that the large-N theory always breaks the classical degeneracy at the lowest order in the $1/N$ expansion, and selects the correct large-S ground state. We find, both numerically and analytically, using a loop expansion, that the large-N theory does indeed break all classical degeneracies. However, the large-N ground state is not a harmonic spin-wave ground state. Since, in the $S \to \infty$ limit the harmonic spin-wave theory becomes exact, this means that the large-N calculation produces an unphysical result. Nevertheless, we find that when the discussion is restricted to harmonic ground states, the large-N and the anharmonic spin-wave mean field theories yield similar results.

Most of the work in this thesis has appeared previously in Ref. [48] (chapters 2–5), Ref. [49] (Ch. 6), and Ref. [50] (Ch. 7).

BIBLIOGRAPHY

[1] R. Moessner and A. P. Ramirez, Phys. Today **59**, 24 (2006).

[2] A. P. Ramirez, Annu. Rev. Mater. Sci. **24**, 453 (1994).

[3] *Frustrated spin Systems*, edited by H. T. Diep (World Scientific, Singapore, 2005).

[4] C. L. Henley, Can. J. Phys. **79**, 1307 (2001).

[5] R. Moessner, Can. J. Phys. **79**, 1283 (2001).

[6] E. Berg, E. Altman, and A. Auerbach, Phys. Rev. Lett. **90**, 147204 (2003).

[7] M. Hermele, M. P. A. Fisher, and L. Balents, Phys. Rev. B **69**, 064404 (2004).

[8] H. Tsunetsugu, Phys. Rev. B **65**, 024415 (2002).

[9] H. Tsunetsugu, J. Phys. Chem. Sol. **62**, 1325 (2002).

[10] O. Tchernyshyov, R. Moessner, and S. L. Sondhi, Europhys. Lett. **73**, 278 (2006).

[11] B. Canals, Phys. Rev. B **65**, 184408 (2002).

[12] B. Canals and C. Lacroix, Phys. Rev. B **61**, 1149 (2000).

[13] O. A. Starykh, A. Furusaki, and L. Balents, Phys. Rev. B **72**, 094416 (2005).

[14] Y. Motome and H. Tsunetsugu, Prog. Theor. Phys. Suppl. **160**, 203 (2005).

[15] O. Tchernyshyov, Phys. Rev. Lett. **93**, 157206 (2004).

[16] M. J. P. Gingras and B. C. den Hertog, Can. J. Phys. **79**, 1229 (2001).

[17] V. N. Kotov, M. Elhajal, M. E. Zhitomirsky, and F. Mila, Phys. Rev. B **70**, 214401 (2004).

[18] M. Elhajal, B. Canals, R. Sunyer i Borrell, and C. Lacroix, cond-mat/0503009 (unpublished).

[19] H. Tsunetsugu and Y. Motome, Phys. Rev. B **68**, 060405(R) (2003).

[20] Y. Motome and H. Tsunetsugu, Phys. Rev. B **70**, 184427 (2004).

[21] J. Villain, R. Bidaux, J. P. Carton, and R. Conte, J. Phys (Paris) **41**, 1263 (1980).

[22] C. L. Henley, Phys. Rev. Lett. **62**, 2056 (1989).

[23] C. Zeng and V. Elser, Phys. Rev. B **42**, 8436 (1990).

[24] J. T. Chalker, P. C. W. Holdsworth, and E. F. Shender, Phys. Rev. Lett. **68**, 855 (1992).

[25] A. B. Harris, C. Kallin, and A. J. Berlinsky, Phys. Rev. B **45**, 2899 (1992).

[26] D. A. Huse and A. D. Rutenberg, Phys. Rev. B **45**, R7536 (1992).

[27] I. Ritchey, P. Chandra, and P. Coleman, Phys. Rev. B **47**, R15342 (1993).

[28] S. Sachdev, Phys. Rev. B **45**, 12377 (1992).

[29] A. Chubukov, Phys. Rev. Lett. **69**, 832 (1992).

[30] C. L. Henley and E. P. Chan, J. Magn. Magn. Mater. **140**, 1693 (1995).

[31] E. F. Shender, Sov. Phys. JETP **56**, 178 (1982).

[32] C. L. Henley, J. Appl. Phys. **61**, 3962 (1987).

[33] E. P. Chan, Ph.D. thesis, Cornell University, 1994.

[34] N. Read and S. Sachdev, Phys. Rev. Lett. **66**, 1773 (1991).

[35] S. Sachdev and N. Read, Int. J. Mod. Phys. B **5**, 219 (1991).

[36] J.-S. Bernier, Y.-J. Kao, and Y. B. Kim, Phys. Rev. B **71**, 184406 (2005).

[37] J. E. Greedan, J. Mater. Chem. **11**, 37 (2001).

[38] R. Moessner and J. T. Chalker, Phys. Rev. B **58**, 12049 (1998).

[39] J. N. Reimers, Phys. Rev. B **45**, 7287 (1992).

[40] C. L. Henley, Phys. Rev. Lett. **96**, 047201 (2006).

[41] O. Tchernyshyov, H. Yao, and R. Moessner, Phys. Rev. B **69**, 212402 (2004).

[42] O. Tchernyshyov, O. A. Starykh, R. Moessner, and A. G. Abanov, Phys. Rev. B **68**, 144422 (2003).

[43] K. Penc, N. Shannon, and H. Shiba, Phys. Rev. Lett. **93**, 197203 (2004).

[44] D. L. Bergman, R. Shindou, G. A. Fiete, and L. Balents, cond-mat/0510202 (unpublished).

[45] S. R. Hassan and R. Moessner, cond-mat/0512594 (unpublished).

[46] J. von Delft and C. L. Henley, Phys. Rev. B **48**, 965 (1993).

[47] M. Kvale (unpublished).

[48] U. Hizi and C. L. Henley, Phys. Rev. B **73**, 054403 (2006).

[49] U. Hizi and C. L. Henley (unpublished).

[50] U. Hizi, P. Sharma, and C. L. Henley, Phys. Rev. Lett. **95**, 167203 (2005).

Chapter 2

Semiclassical spin-waves

In this chapter, we consider the effect of quantum fluctuations on the pyrochlore Heisenberg model, in the semiclassical, $S \gg 1$ limit. In 2.1 we perform a Holstein Primakoff transformation to expand the Hamiltonian in powers of $1/S$. In 2.2, we focus on collinear classical ground states. Next, in Sec. 2.3, we diagonalize the collinear harmonic Hamiltonian to find the spin-wave modes. The contents of this chapter, as well as Ch. 3, Ch. 4, and Ch. 5, were mostly published in Ref. [1].

2.1 Large-S expansion

We start from a given ordered classical state, where the spin directions are parameterized by angles (θ_i, ϕ_i), such that the classical spin direction is

$$\hat{\mathbf{n}}_i = (\sin\theta_i \cos\phi_i, \sin\theta_i \sin\phi_i, \cos\theta_i)\,. \tag{2.1}$$

We expand around this state, in powers of $1/S$, to account for quantum fluctuations, implicitly assuming here that the quantum fluctuations are small and do not destroy the local collinear order. Upon rotation to local axes $(\tilde{x}, \tilde{y}, \tilde{z})$, such that the classical spins are in the $\tilde{z}$ direction (parallel to $\hat{\mathbf{n}}_i$), we apply the usual Holstein-Primakoff transformation. Note that there is an arbitrary angle in the choice of directions $\tilde{x}$ and $\tilde{y}$ and in the following we shall take $\tilde{y}$ to be perpendicular to the z axis. We define boson operators a_i, $a_i^\dagger$ such that

$$\begin{aligned} S_i^{\tilde{z}} &= S - a_i^\dagger a_i\,, \\ S_i^{+} &\equiv S^{\tilde{x}} + iS^{\tilde{y}} = \sqrt{2S - a_i^\dagger a_i}\; a_i \approx \sqrt{2S} a_i\,, \\ S_i^{-} &\equiv S^{\tilde{x}} - iS^{\tilde{y}} = a_i^\dagger \sqrt{2S - a_i^\dagger a_i} \approx \sqrt{2S} a_i^\dagger\,. \end{aligned} \tag{2.2}$$

These operators satisfy the canonical bosonic commutation relations

$$[a_i, a_j^\dagger] = \delta_{ij}\,, \qquad [a_i, a_j] = 0\,, \qquad [a_i^\dagger, a_j^\dagger] = 0\,. \tag{2.3}$$

We obtain the spin-wave Hamiltonian (1.4), where the leading term is the classical Hamiltonian

$$\mathcal{H}_{\rm cl} = S^2 \sum_{ij} J_{ij} \hat{\mathbf{n}}_i \cdot \hat{\mathbf{n}}_j\,, \tag{2.4}$$

which is equivalent of Eq. (1.1), and whose degenerate ground states satisfy

$$\sum_{i\in\alpha} \hat{\mathbf{n}}_i = \mathbf{0}\,. \tag{2.5}$$

for all tetrahedra α. with energy

$$E_{\rm cl} = -N_s S^2\,, \tag{2.6}$$

where N_s is the number of lattice sites. Due to the large classical degeneracy, we must go on to the leading order, harmonic, quantum correction, in order to search for a ground state, while assuming that Eq. (2.5) is satisfied, i.e., that we are expanding around a classical ground state.

The linear spin-wave energy $E_{\rm harm}$ was calculated by Henley [2], using classical equations of motion. The results of that work were that the classical degeneracy is not fully lifted by quantum fluctuations, to harmonic order, and that the remaining degeneracy is associated with a *gaugelike* symmetry. Here we justify these results using the more rigorous Holstein-Primakoff approach, which allows us to gain a better analytic understanding of the degeneracy, as well as perform numerical diagonalization. Furthermore, the Holstein-Primakoff transformation allows for a controlled expansion in powers of $1/S$, including anharmonic order.

We find it convenient to change variables to *spin deviation operators*

$$\boldsymbol{\sigma}^{\tilde{x}} = \sqrt{\frac{S}{2}}(\mathbf{a} + \mathbf{a}^\dagger)\,, \qquad \boldsymbol{\sigma}^{\tilde{y}} = -i\sqrt{\frac{S}{2}}(\mathbf{a} - \mathbf{a}^\dagger)\,, \tag{2.7}$$

where $\mathbf{a}^\dagger = (a_1^\dagger, a_2^\dagger, \ldots, a_{N_s}^\dagger)$ is a vector of operators of length N_s. We shall, from now on, reserve boldface notation for such vectors and matrices. These operators satisfy the commutation relations

$$[\boldsymbol{\sigma}^{\tilde{x}}, \boldsymbol{\sigma}^{\tilde{y}}] = iS\mathbb{1}\,, \qquad [\boldsymbol{\sigma}^{\tilde{x}}, \boldsymbol{\sigma}^{\tilde{x}}] = [\boldsymbol{\sigma}^{\tilde{y}}, \boldsymbol{\sigma}^{\tilde{y}}] = 0\,. \tag{2.8}$$

The harmonic Hamiltonian can now be written in matrix notation

$$\mathcal{H}_{\text{harm}} = \left((\boldsymbol{\sigma}^{\tilde{x}})^\dagger, (\boldsymbol{\sigma}^{\tilde{y}})^\dagger\right) \begin{pmatrix} \mathbf{R}^{\tilde{x}} & \mathbf{P} \\ \mathbf{P}^T & \mathbf{R}^{\tilde{y}} \end{pmatrix} \begin{pmatrix} \boldsymbol{\sigma}^{\tilde{x}} \\ \boldsymbol{\sigma}^{\tilde{y}} \end{pmatrix} - SN_s\,, \tag{2.9}$$

where the block matrixes, with respect to lattice site index are

$$\begin{aligned} P_{ij} &= \frac{J_{ij}}{2}\cos\theta_i \sin\phi_{ij}\,, \\ R_{ij}^{\tilde{x}} &= \delta_{ij} + \frac{J_{ij}}{2}\left(\sin\theta_i \sin\theta_j + \cos\theta_i \cos\theta_j \cos\phi_{ij}\right)\,, \\ R_{ij}^{\tilde{y}} &= \delta_{ij} + \frac{J_{ij}}{2}\cos\phi_{ij}\,, \end{aligned} \tag{2.10}$$

where we defined $\phi_{ij} \equiv \phi_i - \phi_j$. These matrices depend on our arbitrary choice for the local transverse directions $\tilde{x}$ and $\tilde{y}$, and can therefore not be expressed solely in terms of the spin direction $\hat{\mathbf{n}}_i$. Note however, that in the case of *coplanar* spins, one can take, with no loss of generality, $\phi_i = 0$ for all sites, i.e. spins in the (x, z) plane, and find that $P_{ij} = 0$ and that the matrix in Eq. (2.9) is block diagonal.

2.2 Harmonic Hamiltonian for Collinear states

The preceding derivation (Eqs. (1.1-2.9)) is valid for *any* lattice composed of corner sharing simplexes. One can argue on general grounds [3, 4, 5, 6, 7] that the spin-wave energy has local minima for classically collinear states. In lattices that are composed of corner-sharing triangles, such as the kagomé, the classical constraint

[Eqs. (1.3,2.5)] is incompatible with collinearity. However, in the case of the pyrochlore lattice, or any other lattice composed of corner sharing tetrahedra, there is an abundance of collinear classical ground states. We will henceforth assume a collinear classical ground state, i.e. that each site is labeled by an Ising variable $\eta_i = \pm 1$, such that $\mathbf{S}_i = \eta_i \hat{z}$. We will return to the more general, non-collinear case in Sec. 4.4 to justify this assumption a posteriori.

For any classical collinear ground state, the Ising variables must satisfy the tetrahedron constraint

$$\sum_{i \in \alpha} \eta_i = 0 \,, \tag{2.11}$$

for any tetrahedron α. In each tetrahedron there are six bonds: four of which are satisfied antiferromagnetic bonds, with $\eta_i \eta_j = -1$. The other two bonds are unsatisfied ($\eta_i \eta_j = +1$). We call the satisfied and unsatisfied bonds *AFM bonds* and *FM bonds*, respectively.

In the collinear case ($\phi_i = 0$, $\theta_i \in \{0, \pi\}$), our definitions of the local axes for site i, are such that

$$\tilde{x} = \eta_i x \,, \qquad \tilde{y} = y \,, \qquad \tilde{z} = \eta_i z \,. \tag{2.12}$$

We may restore the x-y symmetry of the problem, by transforming the spin deviation operators back to the regular axes by the reflection operation

$$\boldsymbol{\sigma}^x \equiv \boldsymbol{\eta} \boldsymbol{\sigma}^{\tilde{x}} \,, \qquad \boldsymbol{\sigma}^y \equiv \boldsymbol{\sigma}^{\tilde{y}} \,, \qquad \vec{\boldsymbol{\sigma}} \equiv \begin{pmatrix} \boldsymbol{\sigma}^x \\ \\ \boldsymbol{\sigma}^y \end{pmatrix} \,, \tag{2.13}$$

where

$$\boldsymbol{\eta} \equiv \begin{pmatrix} \eta_1 & 0 & 0 & \cdots & 0 \\ 0 & \eta_2 & 0 & \cdots & 0 \\ 0 & 0 & \eta_3 & \cdots & 0 \\ \vdots & \vdots & \vdots & \ddots & \vdots \\ 0 & 0 & 0 & \cdots & \eta_N \end{pmatrix} . \tag{2.14}$$

The transformation (2.13) amounts to a reflection with respect to the y-z plane and makes the diagonal blocks in Eq. (2.9) equal to each other:

$$\mathcal{H}_{\text{harm}} = \vec{\boldsymbol{\sigma}}^{\dagger} \begin{pmatrix} \mathbf{H} & \mathbf{0} \\ \mathbf{0} & \mathbf{H} \end{pmatrix} \vec{\boldsymbol{\sigma}} - S \ \mathrm{Tr}\, \mathbf{H} \,, \tag{2.15}$$

where

$$\mathbf{H} = \mathbb{1} + \frac{\mathbf{J}}{2} = \frac{1}{2}\mathbf{W}^{\dagger}\mathbf{W} \,, \tag{2.16}$$

$\mathbf{J}$ is the matrix whose elements are J_{ij} and $W_{\alpha i}$ is an $N_s/2 \times N_s$ matrix that takes the value 1 if $i \in \alpha$, and 0 otherwise.

The transformation of Eq. (2.13) was chosen to explicitly show the symmetry between the x and y axes in the collinear case. It also causes the Hamiltonian (2.15) to appear independent of $\{\eta_i\}$. However, the particular collinear configuration does enter the calculation via the commutation relations

$$[\boldsymbol{\sigma}^x, \boldsymbol{\sigma}^y] = iS\boldsymbol{\eta} \tag{2.17}$$

Therefore, the equations of motion that govern the spin-waves *do* depend on the classical ground state configuration.

2.3 Diagonalization of harmonic Hamiltonian

Next we would like to Bogoliubov-diagonalize the Hamiltonian of Eq. (2.15), so that we can study its eigenmodes and zero-point energy. As a motivation, we write

the equations of motion

$$\frac{d\vec{\boldsymbol{\sigma}}}{dt} = -i[\vec{\boldsymbol{\sigma}}, \mathcal{H}_{\rm harm}] = 2S \begin{pmatrix} \mathbf{0} & \boldsymbol{\eta}\mathbf{H} \\ -\boldsymbol{\eta}\mathbf{H} & \mathbf{0} \end{pmatrix} \vec{\boldsymbol{\sigma}}\,. \tag{2.18}$$

These are the quantum equivalent of the classical equations of motion derived in Ref. [2]. Upon Fourier transforming with respect to time, and squaring the matrix, we obtain

$$\left(\frac{\omega}{2S}\right)^2 \vec{\boldsymbol{\sigma}} = \begin{pmatrix} (\boldsymbol{\eta}\mathbf{H})^2 & \mathbf{0} \\ \mathbf{0} & (\boldsymbol{\eta}\mathbf{H})^2 \end{pmatrix} \vec{\boldsymbol{\sigma}}\,. \tag{2.19}$$

The spin-wave modes are therefore eigenvectors of the matrix $(\boldsymbol{\eta}\mathbf{H})^2$, with eigenvalues $\lambda_m^2 = (\omega_m/2S)^2$. If the non-hermitian matrix $\boldsymbol{\eta}\mathbf{H}$ is diagonalizable then its eigenvectors $\{\mathbf{v}_m\}$ are the spin-wave modes with eigenvalues $\{\pm|\lambda_m|\}$. Here $\mathbf{v}_m$ is a vector of length N_s, whose indices are site numbers. Note that although we refer to the eigenvectors of $\eta\mathbf{H}$ as the spin-wave modes, strictly speaking, the quantum mechanical modes are pairs of conjugate operators $\boldsymbol{\sigma}^x = \mathbf{v}_m$, $\boldsymbol{\sigma}^y = i\mathrm{sgn}(\lambda_m)\mathbf{v}_m$.

Since $\{\mathbf{H}^{1/2}\mathbf{v}_m\}$ are eigenvectors of the Hermitian matrix $\mathbf{H}^{1/2}\boldsymbol{\eta}\mathbf{H}^{1/2}$, the complete basis of eigenvectors $\{\mathbf{v}_m\}$ can be "orthogonalized" by

$$(\mathbf{v}_m, \boldsymbol{\eta}\mathbf{v}_n) \equiv \mathbf{v}_m^\dagger \boldsymbol{\eta}\mathbf{v}_n = \frac{1}{\lambda_m}\mathbf{v}_m^\dagger \mathbf{H}\mathbf{v}_n = c_m\delta_{m,n}\,. \tag{2.20}$$

We shall henceforth refer to the operation $(\mathbf{v}_m, \boldsymbol{\eta}\mathbf{v}_n)$ as the *inner product* of modes $\mathbf{v}_m$ and $\mathbf{v}_n$. Note that $c_m \equiv (\mathbf{v}_m, \boldsymbol{\eta}\mathbf{v}_m)$ is not really a norm, since it can be zero or, if $\lambda_m < 0$, negative.

The Bogoliubov diagonalization involves transforming to boson operators

$$b_m = \frac{1}{\sqrt{2S|c_m|}}\left((\boldsymbol{\eta}\mathbf{v}_m)^\dagger \boldsymbol{\sigma}^x + i\,\mathrm{sgn}(c_m)(\boldsymbol{\eta}\mathbf{v}_m)^\dagger \boldsymbol{\sigma}^y\right)\,, \tag{2.21}$$

with canonical boson commutation relations, to obtain

$$\mathcal{H}_{\rm harm} = \sum_m \omega_m \left(b_m^\dagger b_m + \frac{1}{2}\right) - SN_s\,, \tag{2.22}$$

with the zero-point energy (setting $\hbar = 1$)

$$E_{\rm harm} = \frac{1}{2}\sum_m \omega_m = S\sum_m |\lambda_m| - SN_s\,. \tag{2.23}$$

The fluctuations of $\boldsymbol{\sigma}^{x,y}$ are now easy to calculate from the boson modes

$$\begin{aligned} \mathbf{G} \equiv \langle \boldsymbol{\sigma}^x (\boldsymbol{\sigma}^x)^\dagger \rangle = \langle \boldsymbol{\sigma}^y (\boldsymbol{\sigma}^y)^\dagger \rangle &= \sum_m \frac{S}{2|c_m|} \mathbf{v}_m \mathbf{v}_m^\dagger\,, \\ \langle \boldsymbol{\sigma}^x (\boldsymbol{\sigma}^y)^\dagger + \boldsymbol{\sigma}^y (\boldsymbol{\sigma}^x)^\dagger \rangle &= \mathbf{0}\,. \end{aligned} \tag{2.24}$$

Note that this is a matrix equation, where $\boldsymbol{\sigma}^{x/y}(\boldsymbol{\sigma}^{x/y})^\dagger$ are $N_s \times N_s$ matrices. The matrix $\mathbf{G}$ has elements $G_{ij} = \langle \sigma_i^x \sigma_j^x \rangle = \langle \sigma_i^y \sigma_j^y \rangle$.

BIBLIOGRAPHY

[1] U. Hizi and C. L. Henley, Phys. Rev. B **73**, 054403 (2006).

[2] C. L. Henley, Phys. Rev. Lett. **96**, 047201 (2006).

[3] E. F. Shender, Sov. Phys. JETP **56**, 178 (1982).

[4] C. L. Henley, Phys. Rev. Lett. **62**, 2056 (1989).

[5] C. L. Henley, Can. J. Phys. **79**, 1307 (2001).

[6] B. E. Larson and C. L. Henley (unpublished).

[7] N.-G. Zhang, C. L. Henley, C. Rischel, and K. Lefmann, Phys. Rev. B **65**, 064427 (2002).

Chapter 3

Spin-wave modes

We now examine the spin-wave modes that we found in Sec. 2.3 to study their properties. In 3.1 we classify them as zero modes, that do not contribute to the zero-point energy, and non-zero modes, that can all be expressed in terms of the diamond lattice formed from the centers of tetrahedra. Within the zero modes, we find, in 3.2, that a number of modes (proportional to $N_s^{1/3}$) have divergent fluctuations. In Sec. 3.3 we discuss the energy band structure and identify special singular lines in the Brillouin zone. In 3.4, we show that the energy of any non-zero mode is invariant under an group of Z_2 gaugelike transformations.

3.1 Zero modes and Non-zero modes

Many of the eigenmodes of the Hamiltonian (2.16), are *zero modes*, i.e. modes that are associated with an (eigen) frequency $\omega_m = 0$. These are the modes $\mathbf{v}_z$ that satisfy

$$(\mathbf{W}\mathbf{v}_z)_\alpha = \sum_{i\in\alpha} \mathbf{v}_z(i) = 0 \qquad \text{for all tetrahedra } \alpha\,. \tag{3.1}$$

Since there are $N_s/2$ tetrahedra, and thus $N_s/2$ constraints, we can expect as many as half of the spin-wave frequencies $\{\omega_m\}$ to be generically zero. In order to prove that indeed half of the eigenmodes of $\mathbf{H}$ are zero modes we first note that the subspace of zero modes is spanned by modes that alternate along *loops*, as in Fig. 3.1, i.e., for a loop $\mathcal{L}$, up to a normalization factor

$$v_{\mathcal{L}}(i) \propto \begin{cases} (-1)^{n_i} & i \text{ site number } n_i \text{ in loop } \mathcal{L} \\ 0 & i \notin \mathcal{L} \end{cases} . \tag{3.2}$$

In order for these loop modes to indeed be zero modes, two consecutive bonds in the loop cannot be from the same tetrahedron, i.e. the sites along each loop are centers of bonds in a diamond lattice loop. In the entire discussion of spin-waves (from now and through chapter 6), we use the term *loop* only for lines in the lattice satisfying this constraint.

The loop zero modes can in turn be written as a linear combination of hexagon modes only, of which there are N_s (see Fig. 3.1a). Hexagons are the shortest loops in this lattice. Since there is a linear dependence between the four hexagons in a big super-tetrahedron (see Fig. 3.1b), then only $N_s/2$ of the hexagon modes are linearly independent [1, 2]. Therefore a basis of zero modes of $\mathbf{H}$ would consist of half of the hexagon modes, and the matrix $(\boldsymbol{\eta}\mathbf{H})^2$ has *at least* $N_s/2$ zero modes. Note that since these modes are zero modes of the matrix $\mathbf{H}$, they are independent of the particular collinear spin arrangement. We refer to these $N_s/2$ modes as the *generic zero modes*, to distinguish them from other zero modes of $(\boldsymbol{\eta}\mathbf{H})^2$ that are not zero modes of $\mathbf{H}$, that we shall discuss in the next section. *All collinear ground states have the same generic zero modes.*

Zero modes mean that the quadratic correction to the classical energy due to small deviations from collinear order vanishes. It is interesting to note, that the zero modes associated with loops that have alternating classical spins η_i, are modes associated with the transformations under which $\mathcal{H}_{\rm cl}$ is invariant. In fact, deviations that rotate spins along these loops by any angle θ take a collinear state to a non-collinear classical ground state, and when $\theta = 180^\circ$, the rotation takes one collinear classical ground state to another. These modes are completely analogous to the so-called *weathervane modes* in the kagomé lattice [3]. We will use the properties of these rotations in Sec. 4.2 to generate a large number of collinear

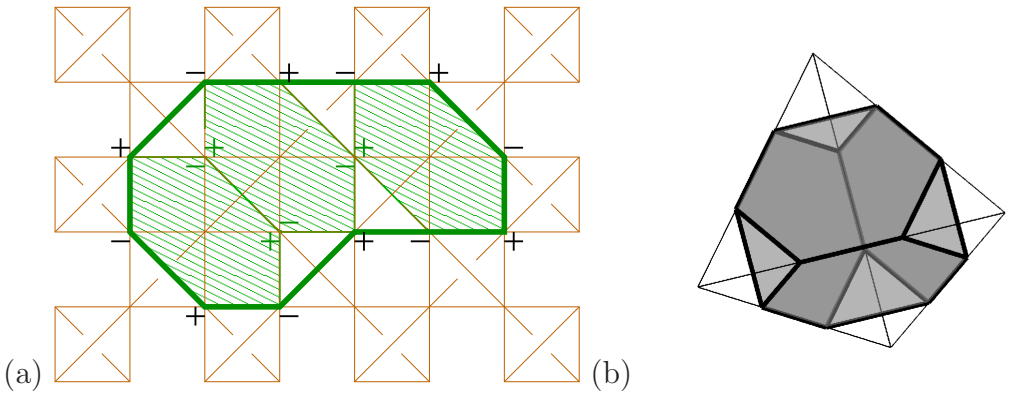

Figure 3.1: Loop zero modes.
(a) Example of a zero mode (in {001} projection) alternating along a loop. Any such loop can be expressed as a linear combination of N_s hexagon modes. Furthermore, there is a linear dependence between the hexagons in each super-tetrahedron, as depicted in (b). The additional constraints reduce the number of independent modes to $N_s/2$.

classical ground state, and in Sec. 4.4 to study the dependence of the zero-point energy on deviations out of collinearity.

Thus, the abundance of spin-wave zero modes is a reflection of the macroscopic continuous classical degeneracy. On the experimental side, the properties of the spinel material $ZnCr_2O_4$, at temperatures just higher than the phase transition into an ordered state, have been shown to be dominated by so-called *local soft modes*, which are spin-wave modes that have zero or infinitesimal frequency [4].

Whereas the zero modes are associated with the large classical degeneracy, they do not contribute to the quantum zero-point energy (2.23). We now consider harmonic modes that have non-zero frequency. For any such mode $\mathbf{v}_{nz}$, the diamond lattice vector $\mathbf{u} = \mathbf{W}\mathbf{v}_{nz}$ is an eigenvector of $(\mathbf{W}\boldsymbol{\eta}\mathbf{W}^\dagger)^2$ with the same eigenvalue

$$(\mathbf{W}\boldsymbol{\eta}\mathbf{W}^\dagger)^2\mathbf{u} = \mathbf{W}(\boldsymbol{\eta}\mathbf{W}^\dagger\mathbf{W})^2\mathbf{v}_{nz} = \lambda^2\mathbf{u} \tag{3.3}$$

In this fashion, we can get rid of $N_s/2$ generic zero modes by projecting to a space

that resides on the diamond lattice sites only, and is orthogonal to all generic zero modes. As already noted, since the generic zero modes are the same for all states, we can consistently disregard them and limit ourselves solely to diamond lattice eigenmodes of Eq. (3.3). Since the matrix $\mathbf{W}\boldsymbol{\eta}\mathbf{W}^\dagger$ is symmetric, it is always diagonalizable and its eigenvectors are orthogonal in the standard sense.

$$\mathbf{u}_m \cdot \mathbf{u}_n \propto \delta_{mn} \,. \tag{3.4}$$

We refer to these remaining $N_s/2$ spin-wave modes, that can be viewed as diamond lattice modes, as the *ordinary modes*. Although the ordinary modes do not generically have zero frequency, we may find that for a given classical ground state, some of them are zero modes. We will find, in the following section, that these are modes that have divergent fluctuations.

3.2 Divergent modes

As is apparent from Eq. (2.24) for the fluctuations G_{ij}, that divergent harmonic fluctuations occur whenever a certain mode $\mathbf{v}_d$ satisfies

$$c_d \equiv (\mathbf{v}_d, \boldsymbol{\eta}\mathbf{v}_d) = 0 \,. \tag{3.5}$$

This can be shown to occur if and only if $\boldsymbol{\eta}\mathbf{H}$ is not diagonalizable, i.e., when the Jordan form of the matrix has a block of order 2.

$$\begin{aligned} \boldsymbol{\eta}\mathbf{H}\mathbf{v}_d &= \mathbf{0} \,, \\ \boldsymbol{\eta}\mathbf{H}\mathbf{w}_d &= \mathbf{v}_d \,. \end{aligned} \tag{3.6}$$

We call the mode $\mathbf{v}_d$, a *divergent zero mode* [As we noted before, a more accurate description would be to refer to the pair of conjugate operators $\boldsymbol{\sigma}^x \sim \mathbf{v}_d$, $\boldsymbol{\sigma}^y \sim \mathbf{w}_d$

as the quantum mechanical divergent mode] From Eq. (3.6), factoring $\mathbf{H} = \frac{1}{2}\mathbf{W}^\dagger\mathbf{W}$ [Eq. (2.16)], we find that *any* divergent zero mode is related to a zero mode of the diamond-lattice equation of motion (3.3) (*diamond lattice zero mode*) $\mathbf{u}_d$

$$\mathbf{u}_d \equiv \mathbf{W}\mathbf{w}_d\,, \qquad \mathbf{v}_d = \boldsymbol{\eta}\mathbf{W}^\dagger\mathbf{u}_d\,. \tag{3.7}$$

Diamond lattice zero modes can be separated into two linear subspaces so that the modes in each subspace are confined to even or odd diamond sublattice. We call such modes *even divergent modes* and *odd divergent modes*, respectively. An even diamond lattice zero mode $\mathbf{u}_d$ corresponds, by (3.7) to a divergent mode

$$v_d(i) = \eta_i u_d(\alpha_{\rm even}(i))\,, \tag{3.8}$$

where $\alpha_{\rm even}(i)$ is the even tetrahedron to which site i belongs. Since any divergent mode $\mathbf{v}_d$ is a zero mode, then it must satisfy the tetrahedron constraint Eq. (3.1). For an even mode, this is automatically guaranteed for the even tetrahedra α, by (3.8)

$$\sum_{i\in\alpha} v_m^{\rm even}(i) = u_m^{\rm even}(\alpha)\sum_{i\in\alpha}\eta_i = 0\,. \tag{3.9}$$

On the other hand, for an *odd* tetrahedron β, we get

$$\sum_{i\in\beta} v_i^{\rm even} = \sum_{i\in\beta} u_m^{\rm even}(\alpha_{\rm even}(i))\eta_i = 0\,. \tag{3.10}$$

Note that there is one linear dependence between the odd and even modes: the Goldstone mode [$v_G(i) = \eta_i$ for all i] can be expressed either as an even mode or as an odd mode [with $u_G(\alpha) = 1$ for all even or odd α, respectively]. Owing to the (almost) independence of the even and odd subspaces of divergent modes, we shall, for the rest of this section, limit the discussion to one sublattice only –the even sublattice– and everything can be carried over trivially to the odd sublattice. Note that each diamond lattice sublattice is an FCC lattice.

3.2.1 Real space support networks

Relatively simple real-space divergent modes can be constructed to satisfy (3.10) with support S_d (S_d is a network composed of a subset of the even diamond sublattice), so that for any odd site β, with even neighbors $\{\alpha_k\}$

$$|\{\alpha_k\} \cap S_d| = \{0, 2\}\,, \tag{3.11}$$

i.e., exactly 0 or 2 even neighbors of β belong to S_d. Eq. (3.10) implies that for a divergent mode $\mathbf{u}_d$ supported on a connected network S_d

$$u_d(\alpha) = \begin{cases} \pm 1 & \alpha \in S_d \\ 0 & \alpha \notin S_d \end{cases}\,. \tag{3.12}$$

If two even diamond lattice sites α_1 and α_2 are connected by a (pyrochlore) bond (ij), and they are both in the support S_d then, by (3.10)

$$u_d(\alpha_1) \cdot u_d(\alpha_2) = \begin{cases} +1 & \text{if } (ij) \text{ is AFM}\,, \\ -1 & \text{if } (ij) \text{ is FM}\,. \end{cases}\,. \tag{3.13}$$

See Fig.3.2 for examples of real space divergent modes.

Upon inspection of Fig. 3.2, it becomes clear that, given a particular support S_d, satisfying (3.11), resolving the values of the Ising variables $\{u_d(\alpha)\}$ is equivalent to finding a ground state configuration of an mock Ising model on S_d, with the AFM (FM) bonds in the $\{\eta_i\}$ spin configuration replaced by FM (AFM) effective Ising bonds. A corollary is that S_d can support a divergent mode only if the mock Ising model is unfrustrated. For example, a square network, as shown in Fig. 3.2(b), supports divergent modes if the product of the bond sign (i.e., $\eta_i\eta_j$ for bond (ij)) around each FCC square is positive, i.e. the flux $\varphi_{\mathcal{L}}$ around corresponding pyrochlore loop is negative.

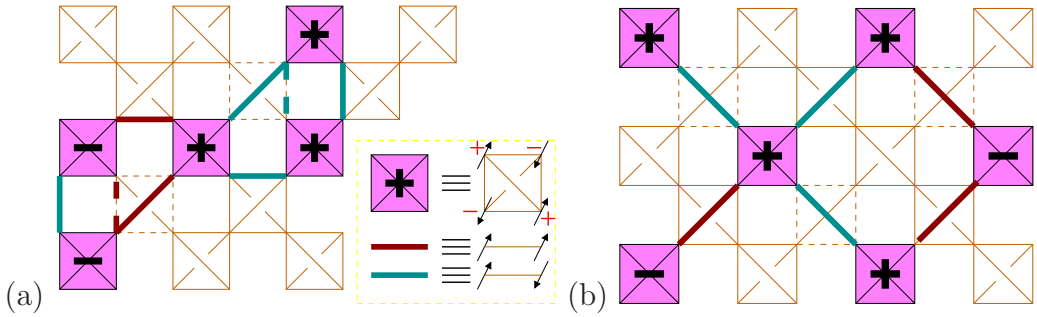

Figure 3.2: Real space divergent modes.
(a) Example of a portion of a {001} slice out of an even divergent mode, in real space (dashed lines connect to adjacent slices). Light (dark) colored bonds represent AFM (FM) bonds, and an even tetrahedron α is marked "$\pm$" for $u_d(\alpha) = \pm 1$. (b) Example of a planar (xy) divergent mode, i.e. a mode that is bounded along the z axis (in this case, to one slice). Divergent modes can be bounded at most, along one of the major axes.

3.2.2 Planar divergent modes

If we examine the rules of constructing a real space divergent modes, we find that their support S_d (on the diamond lattice) can either be unbounded in space, or unbounded in two directions and bounded along *only one* of the major axes, as in Fig. 3.2(b). This can be easily proved: suppose that an even divergent mode is bounded in the x direction. There is an even diamond lattice site α that is in the support of this divergent mode, and its x value takes the maximum possible value x_α [Note that here (x,y,z) are spatial coordinates, while in Sec. 2 they referred to spin directions]. The site α has an odd neighbor at $(x, y, z) = (x_\alpha + 1/4, y_\alpha + 1/4, z_\alpha - 1/4)$ (where the lattice constant of the underlying cubic lattice is taken to be 1), that has two (even) neighbors at $x > x_\alpha$ (and thus cannot be in the S_d), and two (even) neighbors at $x = x_\alpha$. One of these is α, the other – at $(x_\alpha, y_\alpha + 1/2, z_\alpha - 1/2)$ – must, by (3.11) also be in the support of the mode. Continuing this reasoning, we will find that the site at coordinates

$(x_\alpha, y_\alpha + 1, z_\alpha - 1)$ is also in S_d and by induction the support of this mode is unbounded in the $(0, 1, -1)$ direction. Similarly, we can show that the support for this mode is unbounded in the $-y$ axis and the $+z$ directions.

It turns out empirically that one can always construct a basis for divergent modes from planar modes, i.e. modes supported by a quasi-two-dimensional network S_d, satisfying Eq. (3.11). However, the planar divergent modes are generally not mutually orthogonal. The relation between these modes and the Fourier space basis of divergent modes is described in the following section.

3.3 Magnon energy band structure

Our discussion so far has focused on spin waves in real space, and has therefore been applicable to any (even non-periodic) classical collinear ground state. However, in order to perform numerical calculations (in Sec. 4.2), one must consider periodic spin configurations, with a (possibly large) *magnetic unit cell*. We refer to the lattice composed of the centers of the magnetic unit cells as the *magnetic lattice*. We can Fourier transform the Hamiltonian (2.15), using

$$\begin{aligned} \vec{\sigma}_{\mathbf{r}}(l) &= \frac{1}{\sqrt{N_M}} \sum_{\mathbf{q}} \vec{\sigma}^l_{\mathbf{q}} e^{-i\mathbf{q}\cdot(\mathbf{r}+\boldsymbol{\Delta}_l)}\,, \\ \vec{\sigma}_{\mathbf{q}}(l) &= \frac{1}{\sqrt{N_M}} \sum_{\mathbf{r}} \vec{\sigma}^l_{\mathbf{r}} e^{i\mathbf{q}\cdot(\mathbf{r}+\boldsymbol{\Delta}_l)}\,, \end{aligned} \tag{3.14}$$

where $\mathbf{r}$ is a magnetic lattice vector, l is a sublattice index, corresponding to a basis vector $\boldsymbol{\Delta}_l$, N_M is the number of magnetic lattice sites, and $\mathbf{q}$ is a Brillouin zone vector. Note that this deviates from the standard way of Fourier transforming, in that we do not give all of the sites in each unit cell the same phase [i.e. we use $e^{i\mathbf{q}\cdot(\mathbf{r}+\boldsymbol{\Delta}_l)}$ rather than use $e^{i\mathbf{q}\cdot\mathbf{r}}$ for all sublattices l]. The elements of the transformed

Hamiltonian matrix are

$$H_{lm}(\mathbf{q}) = \delta_{lm} + \frac{1}{2}\sum_{\xi_{lm}} e^{i\mathbf{q}\cdot\boldsymbol{\xi}_{lm}}\,, \tag{3.15}$$

where the sum is over all nearest neighbor vectors $\boldsymbol{\xi}_{lm}$ connecting the sublattices l and m. Upon diagonalization, we obtain that the number of bands in the Brillouin zone is equal to the number of sites in the magnetic unit cell, i.e. the number of sublattices. The bands can be classified as follows: half of the energy bands belong to generic zero modes, which have vanishing energy throughout the Brillouin zone. These modes are the zero modes of $\mathcal{H}$ and are identical for all collinear classical ground states. The other half of the spin-wave modes are the ordinary modes, which can be viewed as diamond lattice eigenmodes of Eq. (3.3). Of these bands, the *optical ordinary modes* possess non-zero frequency throughout the Brillouin zone, and the *acoustic ordinary modes* have non-zero energy in most of the Brillouin zone, but vanish along the major axes in reciprocal space (see, for example, the solid lines in Fig. 4.6). Note that this deviates from the common usage of "acoustic band", in which the band goes to zero only at the point $\mathbf{q} = 0$. We find that the number of acoustic zero modes does depend on the particular classical ground state, and the zero modes in these bands are the divergent modes, i.e. modes with divergent fluctuations

$$G_{lm}(\mathbf{q}) \equiv \langle \sigma^x_{\mathbf{q}}(l)\sigma^x_{-\mathbf{q}}(m)\rangle = \langle \sigma^y_{\mathbf{q}}(l)\sigma^y_{-\mathbf{q}}(m)\rangle\,. \tag{3.16}$$

Why are the divergent modes restricted to *divergence lines* in $\mathbf{q}$ space? Since a (non-orthogonal) basis of divergent modes can be made of planar divergent modes, the Fourier space basis is constructed by taking linear combinations of such planar modes, which are localized modes along the (major) axis normal to the plane. We label the $\{100\}$ modes in such a basis by $\{\mathbf{u}^x_m\}$, where x is a (real space) coordinate

along the normal axis, and the index m reflects that there may be several types of plane modes in the x direction [for example, there could be four different types of divergent modes supported by a square-lattice of the form shown in Fig 3.2b]. A divergent mode with wavevector $(q_x, 0, 0)$ can thus be constructed by linear combinations

$$\mathbf{u}_m^{(q_x,0,0)} = \sum_x \mathbf{u}_m^x e^{iq_x x}, , \tag{3.17}$$

and similarly for y and z. These linear combinations can be taken at any $\mathbf{q}$ value along the normal axis, and the number of divergent modes along each axis is equal to the number of values that the index m can take. The conclusion we can draw from this will be important later on (in Sec. 4.3): the rank of the divergent mode space is of order $N_s^{1/3}$.

If we look at the acoustic energy bands to which the divergent modes belong, moving away from the divergence lines, in $\mathbf{q}$ space, we find (see, for example, Fig. 4.6) that the energy increases linearly with $\mathbf{q}_\perp$, the component of $\mathbf{q}$ perpendicular to the divergence line. The dispersion of the acoustic modes can be easily found analytically by solving Eq. (3.3) for small deviations away from a planar divergent mode (e.g. the one depicted in Fig. 3.2b), with $q_\perp$ restricted to be *within* the plane.

The singular spin fluctuations along lines in $\mathbf{q}$ space would produce sharp features in the structure factor $S(\mathbf{q})$, that could be measured in elastic neutron diffraction experiments. Here $\mathbf{q}$ represents a scattering wavevector and not a band wavevector of Bloch-like states). The sharp features would come about because the structure factor is proportional to the spin-spin correlation $\langle \mathbf{S}_\mathbf{q}^\perp \cdot \mathbf{S}_{-\mathbf{q}}^\perp \rangle$, where $\mathbf{S}^\perp$ is the component of the spin transverse to the scattering wave vector $\mathbf{q}$. To

lowest order in S, only σ^x and σ^y contribute to the correlations, and one obtains

$$S(\mathbf{q}) \propto \sum_{\langle lm \rangle} \langle \sigma^l_{\mathbf{q}} \sigma^m_{-\mathbf{q}} \rangle \,. \tag{3.18}$$

Thus, the structure factor should have sharp features, along the major lattice axes, as $\mathbf{q}$ is varied.

Furthermore, since the zero-point energy of the present harmonic theory will be shown to have degenerate ground states (see Sec. 3.4 and Ref. [5]), anharmonic corrections to the harmonic energy determine the ground state selection (See Ch. 6). It turns out that the divergent modes become decisive in calculating the anharmonic energy $\mathcal{H}_{\text{quart}}$. The anharmonic spin-wave interaction would also serve to cut off the singularity of the fluctuations.

In Sec. 4.3, we shall show that the divergent modes also provide a useful basis for constructing and *counting* gaugelike transformations that relate the various degenerate ground states.

3.4 Gaugelike symmetry

Upon examination of the diamond-lattice equation of motion [Eq. (3.3)], it becomes apparent that the harmonic energy E_{harm}, of Eq. (2.23), is invariant under a Z_2 gaugelike transformation that changes the sign of some tetrahedra spin deviations [5]

$$\eta_i \to \tau(\alpha)\tau(\beta)\eta_i \,, \tag{3.19}$$

where $\tau(\alpha), \tau(\beta) \in \pm 1$, and α, β are the two tetrahedra that share site i. While this is an exact gauge symmetry of the projected (diamond lattice) Hamiltonian [related to (3.3)], it is not a physical gauge invariance, since the transformation must be carried out in a way that conserves the tetrahedron rule, i.e. does not take

us out of the classical ground state manifold. Furthermore, these transformations relate physically distinct states. We will henceforth refer by *transformation* to "allowed" gaugelike transformations that conserve the classical tetrahedron rule.

Fig. 3.3 shows an example of a transformation that includes flipping some of the even tetrahedra only (*even transformation*). There are two special transformations that can each be viewed either as an odd or as an even transformation: the identity transformation [$\tau(\alpha) = 1$ for any even α *or* any odd α] the global spin flip [$\tau(\alpha) = -1$ for any even α and $\tau(\alpha) = +1$ for any odd α, or vice-versa].

For any even transformation τ_{even}, we can define its reverse (even) transformation by

$$\overline{\tau}_{\text{even}}(\alpha) = -\tau_{\text{even}}(\alpha)\,, \forall \text{ even } \alpha\,, \tag{3.20}$$

and similarly for odd transformations. Examining Eq. (3.19) we find that there are actually two ways of expressing any transformation as an product of an even transformation and an odd transformation because

$$\overline{\tau}_{\text{even}} \otimes \overline{\tau}_{\text{odd}} \equiv \tau_{\text{even}} \otimes \tau_{\text{odd}}\,, \tag{3.21}$$

Even and odd transformations commute, in the sense that applying an even (odd) transformation does not affect the set of allowed odd (even) transformations [this is trivial to see, as even (odd) transformations only change bonds in odd (even) tetrahedra, which do not alter the rules for constructing odd (even) transformations]. Thus we find that for any reference state, the number of possible gauge transformations $\mathcal{N}_G^{(\text{ref})}$ satisfies

$$\mathcal{N}_G^{(\text{ref})} = \frac{1}{2}\mathcal{N}_{\text{even}}^{(\text{ref})} \times \mathcal{N}_{\text{odd}}^{(\text{ref})}\,, \tag{3.22}$$

where $\mathcal{N}_{\text{even}}^{(\text{ref})}$ and $\mathcal{N}_{\text{odd}}^{(\text{ref})}$ are the number of even and odd transformations for the reference state, respectively, including both the identity transformation and the

overall spin flip.

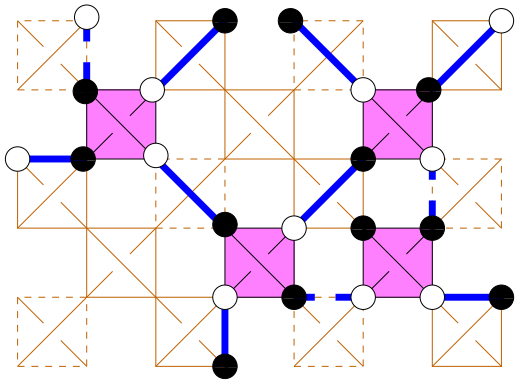

Figure 3.3: Gaugelike transformations.
{001} projection of a portion of an even transformation. The shaded tetrahedra, on the even sublattice of the diamond lattice, are being flipped. Each flipped tetrahedron must be connected by exactly four satisfied (highlighted) bonds to neighboring tetrahedra in the same sublattice. Up (down) spins are signified by solid (open) circles. Dashed lines connect one layer to another in the three-dimensional structure.

If we take a particular classical ground state, and apply a gauge transformation (as depicted in Fig. 3.3) to it, it is easy to see graphically what would happen to the divergent modes (as shown in Fig. 3.2): If a tetrahedron marked by "+" in Fig 3.2 overlaps the support of the gauge transformation, it turns into a "−" and vise versa. More formally, if we start from a given state, in which there is a divergent mode $\mathbf{u}_d$, a transformation $\boldsymbol{\tau}$ (such that $\tau_\alpha = \pm 1$) results in the new state with a divergent mode

$$u(\alpha) \to \tau_\alpha u(\alpha)\,, \tag{3.23}$$

for each α. Otherwise, the number and spatial support of the divergent modes is gauge-invariant. On the other hand, one finds that states that are not related by gauge transformations, and therefore have different (harmonic-order) energies, generally have a different number of divergent modes.

BIBLIOGRAPHY

[1] R. Moessner and J. T. Chalker, Phys. Rev. B **58**, 12049 (1998).

[2] M. E. Zhitomirsky, Phys. Rev. B **67**, 104421 (2003).

[3] P. Chandra, P. Coleman, and I. Ritchey, J. Appl. Phys. **69**, 4974 (1991).

[4] S.-H. Lee *et al.*, Nature **418**, 856 (2002).

[5] C. L. Henley, Phys. Rev. Lett. **96**, 047201 (2006).

Chapter 4

Zero-point energy and effective Hamiltonian

In this chapter, we study the zero-point energy of the harmonic Hamiltonian (2.15). First, in Sec. 4.1, we write the energy as an expansion in real-space paths, and use this expansion to produce an effective Hamiltonian in terms of Ising like fluxes through the diamond lattice loops. Next, in Sec. 4.2, we numerically diagonalize the Hamiltonian to calculate the zero-point energy for various classical ground states. We compare the numerical results to the analytic effective Hamiltonian and find that they agree well, and predict the same ground state family. Finally, in Sec. 4.3 we find an upper bound for the number of harmonic ground states using a correspondence between gaugelike transformations and the divergent modes, which we discussed in Sec. 3.2.

4.1 Effective Hamiltonian

In Ch. 2 we discussed the diagonalization of the harmonic spin-wave Hamiltonian (2.15), which is valid for collinear classical ground states. We wrote the zero-point energy E_{harm} (2.23 as a sum over eigen-frequencies. Later, in Sec. 3.4, we showed that the energy is invariant under a gaugelike transformation (3.19). If we parameterize the E_{harm} in terms of the Ising variables $\{\eta_i\}$, it follows that the energy can only depend on the gauge-invariant combinations of $\{\eta_i\}$, which are products of the Ising variables around loops. These can be viewed as Z_2 flux through the plaquettes of the diamond lattice [1]. In this section, we find an ef-

fective Hamiltonian in terms of these new degrees of freedom, using a real space analytic loop expansion.

The harmonic zero-point energy of Eqs. (2.23), (2.15), and (2.16) can be written as

$$E_{\rm harm} = S\,{\rm Tr}\left(\frac{1}{4}\boldsymbol{\mu}^2\right)^{1/2} - SN_s\,, \tag{4.1}$$

where $\boldsymbol{\mu} = \mathbf{W}\boldsymbol{\eta}\mathbf{W}^\dagger$ is the $N_s/2 \times N_s/2$ matrix, whose indices are diamond lattice sites

$$\mu_{\alpha\beta} = \sum_i W_{\alpha i} W_{\beta i} \eta_i\,. \tag{4.2}$$

For any collinear classical ground state, the diagonal part of $\boldsymbol{\mu}$ vanishes, elements connecting diamond nearest neighbors are equal to ± 1 and all other elements are 0. Therefore, the non-diagonal elements of $\boldsymbol{\mu}^2$ connect between the same diamond sublattice, i.e. between FCC nearest neighbors.

$$(\mu^2)_{\alpha\beta} = \begin{cases} 4 & \alpha = \beta \\ \eta_{\alpha\beta} & \alpha\,,\beta \text{ next nearest neighbors} \\ 0 & \text{otherwise} \end{cases}\,, \tag{4.3}$$

where $\eta_{\alpha\beta} \equiv \eta_i\eta_j$ and (ij) is the (pyrochlore) bond connecting α and β. Thus, we could formally Taylor-expand the square root in Eq. (4.1) about unity. In order to assure convergence of the expansion, as will be discussed later, we generalize this and expand about $A\mathbb{1}$, where A is an arbitrary disposable parameter.

$$\begin{aligned} E_{\rm harm} &= S\,{\rm Tr}\left[A\mathbb{1} + (\frac{\boldsymbol{\mu}^2}{4} - A\mathbb{1})\right]^{1/2} - SN_s \\ &= S\sqrt{A}\sum_{n=0} C_n\,{\rm Tr}(\frac{\boldsymbol{\mu}^2}{A} - 4\mathbb{1})^n - SN_s \\ &= S\sqrt{A}\sum_{n=0} C_n \sum_{k=0}^{n} \frac{(-4)^{n-k}}{A^k} \begin{pmatrix} n \\ k \end{pmatrix} {\rm Tr}\,\boldsymbol{\mu}^{2k} - SN_s\,, \end{aligned} \tag{4.4}$$

with the coefficients

$$C_0 = 1\,, \qquad C_n = (-1)^{n+1}\frac{(2n-3)!!}{8^n n!}\,, \text{for } n > 0\,. \tag{4.5}$$

$\mathrm{Tr}\,\boldsymbol{\mu}^{2k}$ is a sum over all of the diagonal terms of $\boldsymbol{\mu}^{2k}$, i.e. a sum over products of $\boldsymbol{\mu}_{\alpha\beta}$ along all of the closed paths of length $2k$ in the *diamond* lattice. Here a "closed path" is any walk on the diamond lattice that starts and ends at the same site. This expansion involves constant terms that are independent of the sign of $\mu_{\alpha\beta}$ as well as terms that do depend on particular spin configurations. For example, any path of length $2k$, such that each step in one direction is later retraced backwards (a *self-retracing path*), will contribute 1 to $\mathrm{Tr}\,\mu^{2k}$. On the other hand, paths involving *loops* on the lattice could contribute either $+1$ or -1 depending on the spin directions. Thus, we can re-sum Eq (4.4) to obtain an effective Hamiltonian

$$E^{\text{eff}}_{\text{harm}} = E_0 + K_6\Phi_6 + K_8\Phi_8 + \sum_{s(10)} K_{10,s}\Phi_{10,s} + \cdots\,, \tag{4.6}$$

where K_{2l} and $K_{2l,s}$ are constants, which we calculate below, and Φ_{2l} ($\Phi_{2l,s}$) is a sum over all *loops* of length $2l$ (and type s). The index s is to differentiate between different types of loops of length $2l$ that are not related to each other by lattice symmetries. In our case, we do not need the index s for loops of length 6 or 8, since there is just one type of each. On the other hand, there are three different types of loops of length 10, and therefore there are three different $2l = 10$ terms. Since we will explicitly deal with just the first three terms in Eq. (4.6), we shall omit the index s from now on. In fact, in the approximation that we present below, we will assume that all of the loops of length $2l$ can be grouped with the same coefficient K_{2l}.

By our definition of loops, Φ_{2l} can be expressed either in terms of $2l$ diamond lattice sites along the loop $(\alpha_1, \alpha_2, \ldots, \alpha_{2k})$, or in terms of $2l$ *pyrochlore* lattice

sites $(i_1, i_2, \ldots, i_{2l})$:

$$\begin{aligned} \Phi_{2l} &\equiv \sum_{(\alpha_1,\alpha_2,\ldots,\alpha_{2l})} \mu_{\alpha_1\alpha_2}\mu_{\alpha_2\alpha_3}\cdots\mu_{\alpha_{2l}\alpha_1} \\ &= \sum_{(i_1,i_2,\ldots,i_{2l})} \eta_{i_1}\eta_{i_2}\cdots\eta_{i_{2l}}\,. \end{aligned} \tag{4.7}$$

Note that in general, paths that we consider in the calculation (and that are not simple loops) should only be viewed as paths in the diamond lattice.

4.1.1 Bethe lattice harmonic energy

Before we evaluate the coefficients in Eq. (4.6) for the diamond lattice, we shall consider the simpler case of a coordination $z = 4$ Bethe lattice. In order for this problem to be analogous to ours, we assume that the number of sites is $N_B = N_s/2$ and that each bond $(\alpha\beta)$ in the lattice is assigned an Ising variable $\mu_{\alpha\beta} = \pm 1$. In this case, since each bond included in any closed path along the lattice is revisited an even number of times, and since $\mu_{\alpha\beta}^2 = 1$ for any bond in the lattice, then each closed path of length $2k$ contributes 1 to $\mathrm{Tr}\,\boldsymbol{\mu}^{2k}$. Thus all bond configurations in the Bethe lattice would have the same energy.

Calculating the Bethe lattice energy for a given path length $2k$ turns out to be a matter of *enumerating* the closed paths on the Bethe lattice, which can be done *exactly* using simple combinatorics (see Appendix A). The sum (4.4) does not converge, as we consider longer and longer paths, for the trivial choice of $A = 1$, but converges well for $A \gtrsim 1.4$ (see Fig. 4.1). In the thermodynamic limit, we obtain (see Eq. (A.13))

$$E_{\mathrm{harm}}(\mathrm{Bethe}) = E_0 = -0.56395 S N_s \pm 5\times 10^{-5} S N_s\,. \tag{4.8}$$

This value was obtained from Eq. (4.4), cutting it off at $n = 30$ and extrapolating to $n \to \infty$ (see Fig. 4.2).

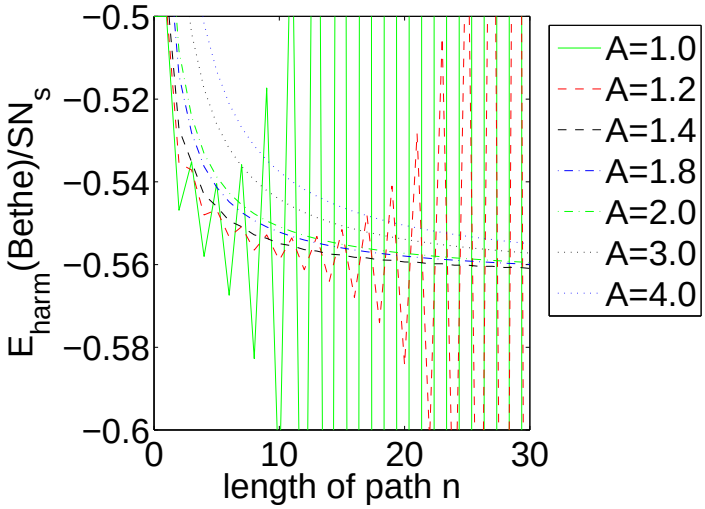

Figure 4.1: Analytically calculated constant E_0, in Bethe lattice approximation. The calculated value is shown here as a function of the maximum path length considered, for various values of A. We find that the sum converges for $A \gtrsim 1.4$.

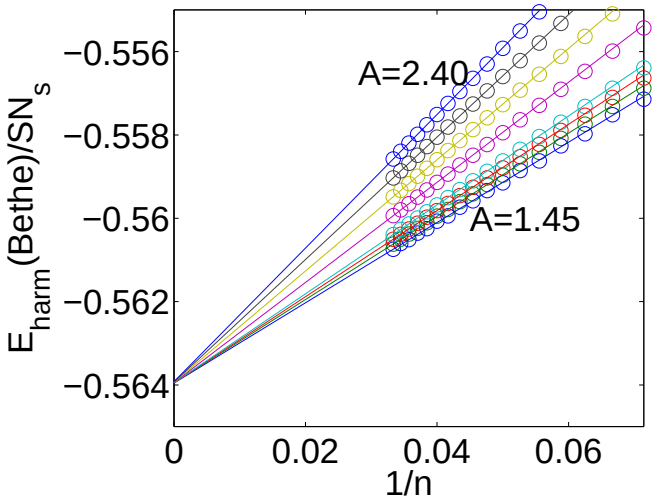

Figure 4.2: Extrapolation of the constant E_0.
Calculated energy in the Bethe lattice approximation for paths of length $n \leq 30$ extrapolated to $n \to \infty$, using the linear dependence of E_0 on $1/n$. The calculated energy is shown as open circles and the extrapolated inverse linear dependence as lines. We see that the extrapolated results are nearly independent of our choice of $A > 1.4$.

It should be noted that we neglected any boundary effects in the Bethe lattice calculation. There is no justification for this in Bethe lattices, since a finite fraction of the lattice points live on the boundary. However, as we shall see in the following, our real interest is in mapping Bethe-lattice paths to diamond-lattice paths. Since the boundaries do not play any significant role in the infinite diamond lattice, we are free to ignore them.

It turns out that since $E_{\rm harm}$(Bethe) is the spin-wave zero-point energy on the Bethe lattice, it can be calculated by solving the spin-wave equation (3.3) on the Bethe lattice. This has actually been previously done in Ref. [2]. The authors in this paper solved an equivalent tight binding model on the Bethe lattice and found a density of states (for general coordination z)

$$\rho(\lambda) = \frac{z}{\pi} \frac{\sqrt{(z-1)-\lambda^2}}{z^2 - 4\lambda^2} \,. \tag{4.9}$$

To find the zero point energy we integrate over $|\lambda|\rho(\lambda)$:

$$\begin{aligned} E_{\rm harm}(\text{Bethe}) &= 2SN_B \int_0^{\sqrt{z-1}} \lambda\rho(\lambda) d\lambda - SN_s \\ &= \frac{zSN_B}{\pi} \left[\sqrt{z-1} - \frac{z-2}{2} \arctan \frac{2\sqrt{z-1}}{z-2} \right] - SN_s \,. \end{aligned} \tag{4.10}$$

In out case, $z = 4$ and $N_s = 2N_B$ and we obtain

$$E_{\rm harm}(\text{Bethe}) = SN_s \left[\frac{2\sqrt{3}}{\pi} - \frac{5}{3} \right] = -0.564009 SN_s \,, \tag{4.11}$$

which agrees well with the result (4.8). This serves as reaffirmation that our numerical technique is valid (for the Bethe lattice), and we shall use it in the following.

4.1.2 Bethe lattice approximation for the constant term

What can we learn from the Bethe lattice calculation about the diamond lattice effective energy? It turns out that actually the coordination-4 Bethe lattice calculation provides a very good approximation for the constant term E_0. There is a one-to-one correspondence between the Bethe lattice paths, and self-retracing diamond lattice paths, which are the paths that contribute to E_0. Conversely, the product of $\mu_{\alpha\beta}$ along a path that goes around a loop depends on the particular classical ground state, and therefore contributes to the term in Eq. (4.6) corresponding to that loop and not to E_0.

There is only one type of path that contributes to the constant term, but was omitted in the Bette lattice approximation: If a loop is repeated twice (or any even number of times), in the same direction, as in Fig. 4.3b, it *does* contribute a constant term since each $\mu_{\alpha\beta}^2 = 1$ for each link along the loop. A simple argument can be given to show that the constant terms involving repeated loops are negligible compared to the Bethe lattice terms. First, we realize that the contribution of paths involving repeated loops is exactly the same as the contribution due to another subset of paths that have already been counted by the Bethe lattice enumeration: self-retracing paths that go around a loop, and then return, in the opposite direction (see Fig. 4.3a). We call these *self-intersecting* self-retracing paths since they include retraced diamond lattice loops. Since they still correspond to Bethe lattice paths, they can be readily enumerated.

In order to get an idea for the number of such self-intersecting paths, consider the smallest loop, a hexagon. The number of paths of length $2k = 12$ starting from a particular point is (by Appendix A), $f_6 = 195352$, while the number of hexagons touching that point is only 12, accounting for 24 intersecting paths of

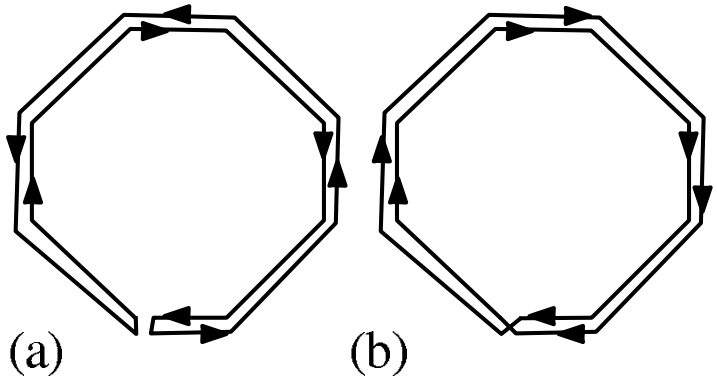

Figure 4.3: Repeated loops that contribute constant terms.
(a) Circled back and forth, and accounted for by the Bethe lattice enumeration (self-intersecting paths), and (b) Repeated in the same direction, not accounted for in our calculation.

length $2k \leq 12$! If we now consider the paths of length 14 starting from the same point, then there are fewer than 100 involving a repeated hexagon, while there are nearly 2 million in total. Essentially, the number of self-intersecting paths, involving loops of length $2l$ is smaller by a factor greater than $(z-1)^l$ than the total number of paths of the same length.

The argument is reinforced a posteriori, by enumeration of paths involving loops, that we do below. The lowest order correction to the constant term E_0 (from Eq. (4.8) due to repeated loops is of the same order as the coefficient for a loop of particular loop of length 12 (circling twice around a hexagon), which we find to be of order 10^{-4}.

4.1.3 One loop terms

We now move on to calculate the coefficients K_{2l} of the non-constant terms that involve simple loops. The prediction of Ref. [3] is that these terms decay with increased length of loops and therefore an effective Hamiltonian of the form (4.6)

can be derived.

Consider a particular loop of length $2l$. We try to enumerate all of the closed paths of length $2k$ that involve this loop and *no other loops*, i.e. all of the terms proportional to $\prod_{i=1}^{2l} \mu_{\alpha_i \alpha_{i+1}}$, where α_i are the sites along the loop ($\alpha_{2l+1} \equiv \alpha_1$).

Since we allow for no additional loops, we assume that the path is a *decorated loop*, i.e. a loop with with self-retracing (Bethe lattice-like) paths emanating from some or all of the sites on it. In order for this description to be unique, we allow the self-retracing path emanating from site α_i along the loop to include site α_{i-1}, but not site α_{i+1}. Thus, the first appearance of the bond $(i, i+1)$ is attributed to the loop, and any subsequent appearance must occur after going back from a site $j > i$, and is attributed to the self-retracing path belonging to j.

Appendix A.2 describes the practical aspects of this calculation. See Fig. A.2 for a diagrammatic description of the paths we enumerate. The approximation neglects, as before, the contribution of repeated loops, which is negligible, by the argument of Sec. 4.1.2. This means that, within our approximation, all loops of length $2l$ have the same coefficient in Eq. (4.6). Calculating the sums in Eq. (4.4) for $n \leq 30$ and extrapolating to $n \to \infty$, we obtain the values $K_6 = 0.0136S$, $K_8 = -0.0033S$.

Looking at the first three terms in the effective Hamiltonian (4.6), it follows that, to leading order in the loop length $2l$, the preferred collinear states should have as many hexagon loops $\mathcal{L}$ with negative flux $\varphi_{\mathcal{L}} = -1$ as possible and as many octagons $\mathcal{L}$ with $\varphi_{\mathcal{L}} = +1$ as possible. It turns out [3] that there is a family of (gauge-equivalent) collinear states that optimize both of these conditions: the so-called π-*flux states* (using the terminology of Ref. [1]), in which

$$\Pi_{\hexagon} \eta_i = -1 \,, \tag{4.12}$$

for *all* hexagons. In the next section we go on to numerically calculate the zero-point energy for a large number of states, in order to prove that the π-flux states are indeed the ground states.

In the next section, we shall compare the effective energy (4.6) to numerical diagonalization.

4.2 Numerical diagonalization

In order to be able to test our predictions numerically, we first constructed a large number of classical ground states, using a path flipping algorithm [4, 5] on a cubic unit cell of 128 sites, with periodic boundary conditions. In each step of this algorithm we randomly select a loop of alternating spins (of any length) to obtain a new classical ground state (see Appendix C.1). This algorithm is ergodic, in the sense that it can reach any collinear classical ground state that is supported by the same unit cell. [1] Considering the large classical degeneracy, we can construct a very large number of collinear classical ground states in this manner. In order to explore diverse regions of the configuration space, we started the algorithm with various different states that we constructed by hand.

We have Fourier transformed the Hamiltonian (2.15), with a magnetic unit cell of 128 sites, diagonalized for each $\mathbf{q}$ value, and calculated the harmonic zero-point energy (2.23) for fluctuations around a wide range of classical ground states. We show the calculated E_{harm} for 50 sample states in Fig. 4.4 [2] Our calculations verified that indeed gauge-equivalent states always have the same energy.

[1] It is my opinion that an algorithm the flips only AFM *hexagons* would not be ergodic (beyond the obvious fact that it would never reach a zero-flux state).

[2] The energies in Table I of Ref. [3] are higher by exactly $+S$ per spin compared to the results presented here, because that calculation omits a constant term arising in the Holstein-Primakoff expansion.

We also show in Fig, 4.4 the effective energy $E^{\text{eff}}_{\text{harm}}$ for the same 50 states, using K_6 and K_8 calculated above. The effective Hamiltonian, even with just 3 terms, proves to do a remarkably good job of approximating the energy. The root-mean-squared (RMS) error for the 50 states shown in Fig. 4.4 is 1×10^{-3}, and it can be attributed to higher order terms ($2l > 8$) in the expansion (4.6).

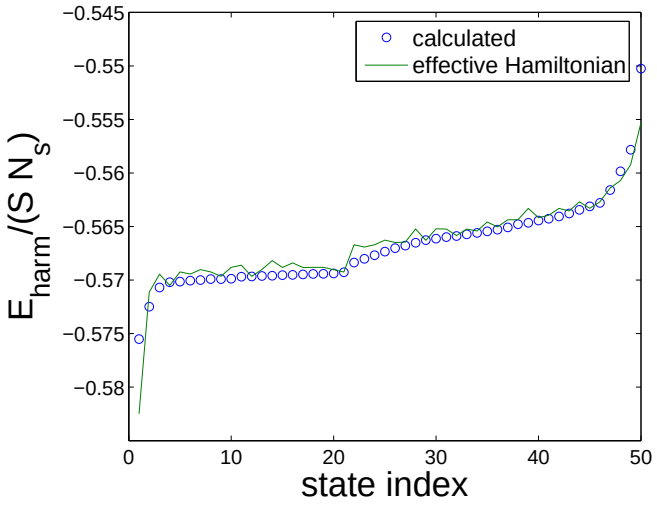

Figure 4.4: Zero-point energy for 50 randomly generated classical ground states. The calculated energy is compared to the Ising effective energy of Eq. (4.6), with $2l \leq 8$. State number 1 in the plot is the π-flux state and state 50 is the zero-flux state, in which all of the terms Φ_{2l} take the maximum possible value. Notice that the effective Hamiltonian is not as good at calculating the energies of these two extreme states, as it does of calculating the energies of other states. This is because neglected higher order terms in these states tend to add up in these states rather than cancel out.

Among the hundreds of collinear states that we constructed, we indeed find that there is a family of exactly degenerate ground states, satisfying Eq. (4.12). In Fig. 4.5 we show some of the ground states. The smallest magnetic unit cell that we obtain for a ground state has 16 spins, although if we consider bond variables rather than spins (as in Fig. 4.5), the unit cell can be reduced to 8 sites (see Appendix B). The highest energy, among collinear states, is obtained for the

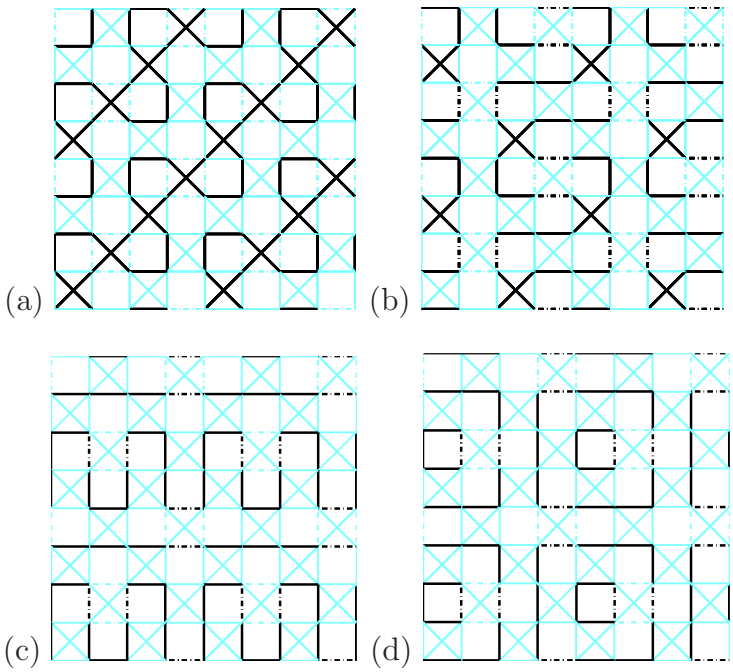

Figure 4.5: Harmonic ground states.
{001} slices of some of the ground states with the smallest magnetic unit cells. For clarity, we only show the bond types, which are (unlike the spin directions), identical for all {001} slices, for these particular states,. FM bonds are presented as dark lines and AFM bonds as light lines. Dashed lines connect this slice to adjacent slices.

zero-flux states, for which the spin directions have a positive product around each hexagon. Note that since the spin product around any loop can be written as a product of hexagon fluxes, all states satisfying Eq. (4.12) have the same loop terms Φ_{2l}, for any l, and are thus gauge-equivalent. In general, if two states have the same hexagon product for every hexagon, they are necessarily gauge-equivalent.

Once we have established that the π-flux states are the ground states, we go on to find such states. To search for π-flux states, we developed a computer algorithm that randomly generates even or odd gauge transformations starting from a particular state, and a unit cell with periodic boundary conditions. We start by flipping a random even tetrahedron. In each subsequent step, we find

an odd tetrahedron that violates the tetrahedron rule (i.e. has non-zero sum), and randomly flip one of its (even) neighbors that can fix that violation. This is repeated until there are no more violated tetrahedra. A similar algorithm is employed to find odd transformations. See Appendix C.2 for the details of the algorithm.

We performed an exhaustive search for ground states, satisfying Eq. (4.12), in the 128 spin cubic magnetic unit cell of linear dimension $L = 2$. We started with a particular π-flux ground state and randomly generated 10^7 even and 10^7 odd gauge transformations and found 142 unique transformations on each sublattice, resulting, by Eq. (3.22), in a total of 10082 distinct states. Only 24 of these are unique with respect to lattice and spin-flipping symmetries. Note that although the number of even gauge transformations and the number of odd gauge transformations turn out to be the same for the harmonic ground states, they need not be the same for other states. Fig.4.5 shows the states with the smallest unit cells. By construction, all of these states are exactly degenerate to harmonic order in spin-wave theory. In Ch. 6, we shall explore the anharmonic selection among the harmonic ground states.

4.3 Ground state entropy

In the preceding section we have found that there is a large family of exactly degenerate ground states. Any two of these states are related by a gauge transformation of the type discussed in Sec. 3.4, and therefore, in order to enumerate these states, we must find how many gauge transformations one can perform on a given ground state, in an arbitrarily large system. In Ref. [3], the number of ground states was speculated to be of order e^L, where L is the linear dimension of the system size

(as opposed to a classically extensive entropy). However, that was only rigorously shown to be a *lower bound*, by explicitly constructing a set of layered ground states in which each layer can independently be flipped. In fact, most of the π-flux states that we present throughout this thesis are not included in that set of states [In Fig. 4.5 *only* (d) is included in that set of states and, later on, in Fig. 6.9 only one of the lines shown is included in this set]. Here, we aim to find an *upper bound* for the number of ground states.

Comparing Figs. 3.3 and 3.2, we see that there is a close relation between even (odd) transformations and even (odd) divergent modes. Any (diamond lattice) divergent mode $\mathbf{u}_G$ that has $u_G(\alpha) = +1$ for any α in its support, describes a valid gauge transformation. This is reminiscent of the relation that we saw in Sec. 3.1, between generic zero modes of $\mathcal{H}_{\rm harm}$ and transformations that keep $\mathcal{H}_{\rm cl}$ invariant. The relation between divergent modes and transformations, as illustrated above, and our knowledge of the divergent modes allows us to demonstrate that the entropy has an upper bound of order $L \ln L$.

Consider a particular reference harmonic ground state. We assume that all of the ground states are related to each other by gauge transformations. Thus, any ground state is related to the reference state by a transformation, that can be almost uniquely expressed as the product of an even and an odd transformation. The number of ground states $\mathcal{N}_0$ is equal to the number of transformations possible for the reference state $\mathcal{N}_G^{(\rm ref)}$ (see Eq. (3.22)).

$$\mathcal{N}_0 = \mathcal{N}_G^{(\rm ref)} \,. \tag{4.13}$$

We have seen in Sec. 3.3 that the number of independent divergent modes is of order L. In the π-flux harmonic ground states, we find that there are $n_{\rm div} = 24L$ independent divergent modes, half of which are even and half odd. Here L is

measured in units of the underlying cubic lattice.

We will focus, for the moment, on the linear subspace of *even* divergent modes, of dimension $n_{\rm even}$. Consider an (not necessarily orthogonal) basis of $n_{\rm even}$ real space planar even divergent modes ($n_{\rm even} = 12L$ for π-flux states), i.e. $\{\mathbf{u}_m\}$ are a set of linearly independent vectors residing on the even diamond sublattice that have amplitude 1 on every diamond-lattice site in their support S_m

$$u_m(\alpha) = \begin{cases} \pm 1 & \alpha \in S_m \\ 0 & \alpha \notin S_m \end{cases} . \tag{4.14}$$

Any even gauge transformation is associated with a divergent mode $\mathbf{u}_G$ also residing on the even sublattice, and satisfying $u_G(\alpha) = +1$, for any $\alpha \in S_G$. Define the projection of $\mathbf{u}_G$ on a basis vector $\mathbf{u}_m$:

$$C_G^m \equiv \frac{\mathbf{u}_G \cdot \mathbf{u}_m}{\mathbf{u}_m \cdot \mathbf{u}_m} . \tag{4.15}$$

We can write the transformation in terms of the basis

$$\begin{aligned} \mathbf{u}_G &= \sum_{m=1}^{n_{\rm even}} \frac{\left(\mathbf{u}_G - \sum_{l<m} \frac{\mathbf{u}_G \cdot \mathbf{u}_l}{\mathbf{u}_l \cdot \mathbf{u}_l} \mathbf{u}_l\right) \cdot \mathbf{u}_m}{\mathbf{u}_m \cdot \mathbf{u}_m} \mathbf{u}_m \\ &= \sum_{m=1}^{n_{\rm even}} \left(C_G^m - \sum_{l<m} C_G^l \frac{\mathbf{u}_m \cdot \mathbf{u}_l}{\mathbf{u}_m \cdot \mathbf{u}_m} \right) . \end{aligned} \tag{4.16}$$

In the case of the pyrochlore π-flux states, each of the planar divergent modes has a support of $|S_m| = 4L^2$ diamond lattice sites and, by Eq. (4.14), we find that $|\mathbf{u}^m|^2 = |S_m|$. Since $\mathbf{u}^G(\alpha)$ is 0 or 1 for each α, the inner product $\mathbf{u}_G \cdot \mathbf{u}_m$ is also an *integer* satisfying

$$|\mathbf{u}_G \cdot \mathbf{u}_m| \leq |\mathbf{u}_m|^2 = |S_m| . \tag{4.17}$$

Therefore, each of the coefficients C_G^m in Eq. (4.16) can take one of, at most, $2|S_m|+1$ values. Since there are $n_{\rm even}$ coefficients C_G^m that determine $\mathbf{u}_G$, the number of

possible vectors $\mathbf{u}_G$ is $\prod_m (2|S_m|+1) \lesssim (2L)^{2n_{\text{even}}}$. This is an upper bound on the number of even transformations and, similarly, of odd transformations, as well. By Eq. (3.22), we find that the number of π-flux states satisfies

$$\mathcal{N}_0 \leq \frac{1}{2}(2L)^{2n_{\text{div}}} . \tag{4.18}$$

The entropy is defined as $\ln \mathcal{N}_0$ and, is at most, of order $L \ln L$. From Ref. [3] we know that $\mathcal{N}_0 > 2^{4L}$, and the entropy is at least of order L.

This same bound on the order of the multiplicity applies to *any* family of gauge-equivalent Ising configurations, since we enumerated the possible gauge transformations on *any* given reference state (not necessarily a π-flux state), which implies that the upper bound to the number of states in *any* gauge-equivalent family is of the same order. However, while the orders of magnitude of the multiplicities of all energy levels are the same, the coefficients in front of $L \ln L$ differ, because the number of independent divergent modes (which is always of order L) is generally not the same for different gauge families.

4.4 Non-collinear spins

We now move on to comment the case of non-collinear classical ground states, aiming to show that the energy of *any* collinear ground state increases upon rotating some of the spins out of collinearity.

In the kagomé lattice it was found that, in the space of all classical ground states, the coplanar states are local minima [6] and that upon an out-of-plane rotations, the zero-point energy increases linearly with the angle of rotation [6, 7].

In the following we show that the linear angle dependence is a property of divergent zero modes. In the kagomé lattice there is an entire band of divergent

modes, and thus they dominate the energy, upon an out-of-plane rotation. In the pyrochlore, on the other hand, the fraction of divergent modes among all modes goes to zero in the thermodynamic limit. Even though the divergent modes' energy is linear in the rotation angle away from *collinearity*, the total zero point energy is found to increase only quadratically.

4.4.1 Collinear states are extrema of E_{harm}

Consider first the case of a coplanar rotation, i.e., without loss of generality, some of the spins are rotated such that the angle θ_i is neither 0 nor π, while ϕ_i remains 0. The elementary way of performing such a rotation is to rotate the spins in an alternating (in η_i) loop, by $+\theta$ and $-\theta$ in an alternating fashion, where θ is a constant.

$$\begin{aligned} \theta_i = 0 \quad &\rightarrow \quad \theta_i = \theta \,, \\ \theta_i = \pi \quad &\rightarrow \quad \theta_i = \pi - \theta \,. \end{aligned} \tag{4.19}$$

Carrying through the derivation of the equation of motion (2.19) (see Appendix B.2), for the coplanar case, we find that the dynamical matrix elements change

$$\eta_i \eta_k H_{ik} H_{kj} \rightarrow \cos(\theta_i - \theta_k) H_{ik} H_{kj} \,. \tag{4.20}$$

This means that in the expansion (4.4), $\boldsymbol{\mu}^2$ changes from Eq. (4.3) to

$$(\mu^2)_{\alpha\beta} = \begin{cases} 4 & \alpha = \beta \\ \cos\theta_{\alpha\beta} & \alpha \,, \beta \text{ next nearest neighbors} \\ 0 & \text{otherwise} \end{cases} \,. \tag{4.21}$$

Here $\theta_{\alpha\beta} \equiv \theta_i - \theta_j$, where (ij) is the (unique) pyrochlore bond a site $i \in \alpha$ and a site $j \in \beta$.

To see how the zero-point energy changes with coplanar deviations away from a collinear state, we take the derivative of the Hamiltonian (2.9) with respect to θ_i

$$\frac{\partial \mathcal{H}_{\rm harm}}{\partial \theta_i} = -\sum_j J_{ij} \sin(\theta_i - \theta_j) \sigma_i^{\tilde{x}} \sigma_j^{\tilde{x}} \,. \tag{4.22}$$

This is clearly zero for any collinear state. Therefore all collinear states ($\theta_i - \theta_j \in \{0, \pi\}$) are local extrema of $E_{\rm harm}(\{\theta_i\})$.

We have shown that the collinear states are local extrema of $E_{\rm harm}$, in the space of coplanar classical ground states. However, are they minima or maxima? In order to find out, we calculate the Hessian $\mathbf{M}$ at a given collinear state

$$M_{ij} \equiv \frac{1}{2} \left. \frac{\partial^2 E_{\rm harm}}{\partial \theta_i \partial \theta_j} \right|_{\rm coll} \,. \tag{4.23}$$

To find $\mathbf{M}$, we take the second derivative of the Hamiltonian, evaluated at a collinear state

$$\begin{aligned} \left. \frac{\partial^2 \mathcal{H}_{\rm harm}}{\partial \theta_i \partial \theta_j} \right|_{\rm coll} &= J_{ij} \cos(\theta_i - \theta_j) \sigma_i^{\tilde{x}} \sigma_j^{\tilde{x}} - \delta_{ij} \sigma_i^{\tilde{x}} \sum_k J_{ik} \cos(\theta_i - \theta_k) \sigma_k^{\tilde{x}} \\ &= J_{ij} \sigma_i^x \sigma_j^x - \sigma_i^x \delta_{ij} \sum_k J_{ik} \sigma_k^x \,, \end{aligned} \tag{4.24}$$

where we took $\cos(\theta_i - \theta_j) \to \eta_i \eta_j$ at the collinear state and used Eq. (2.13) to transform to the σ^x operators.

In order to calculate the Hessian matrix $\mathbf{M}$ we take the expectation value of (4.24). We get terms involving $G_{ij} = \langle \sigma_i^x \sigma_j^x \rangle$ [see Eq. (2.24)]

$$M_{ij} = \frac{1}{2} \left. \frac{\partial^2 \langle \mathcal{H}_{\rm harm} \rangle}{\partial \theta_i \partial \theta_j} \right|_{\rm coll} \approx \begin{cases} \sum_k J_{ik} G_{ik} & i = j \\ \frac{1}{2} J_{ij} G_{ij} & \text{otherwise} \end{cases} \,. \tag{4.25}$$

In order to prove that the collinear states are local minima with respect to $\{\theta_i\}$, we would have to demonstrate that $\mathbf{M}$ is positive definite. Unfortunately, we have not been able to show this analytically,

The inset in Fig 4.6 shows a numerical example $E_{\rm harm}(\{\theta_i\})$ for the state in Fig. 4.5(a), where all of the spins along the AFM line, in the (110) direction, are rotated by an angle away from the axis of the other spins. Clearly, the lowest energy configurations are collinear. For small deviations of θ_i from collinearity, the deviation of the energy from the value is quadratic:

$$E_{\rm harm}(\{\theta_i\}) - E_{\rm harm}(0) = \mathcal{O}(\{(\theta_i - \theta_j)^2\})\,. \tag{4.26}$$

Since the Hessian matrix elements M_{ij} are dominated by the fluctuations of the divergent modes, we focus, in the following section, on these modes. We will show that the divergent modes' frequency becomes nonzero for coplanar states, and therefore the zero point energy increases upon rotation from a collinear to a coplanar state.

4.4.2 Spin-wave modes upon deviation from collinearity

In order to better understand the origin of the quadratic (in θ) energy change in Eq. (4.26), we examine the eigenmodes of the new dynamical matrix (4.20). Looking at the harmonic Hamiltonian (2.9), in the coplanar case ($\phi_i = 0$), we find that it is, as in the collinear case, block diagonal, and the lower-right block $\mathbf{R}^y$ is the same as for a collinear state $\mathbf{R}^y = \mathbf{H}$. Thus, all of the $N_s/2$ generic zero modes of the collinear dynamical matrix (using the jargon of Ch. 3) remain zero modes for *any* coplanar spin arrangement. One finds, however, that these generic zero modes acquire divergent fluctuations in coplanar states, because of the difference in stiffness between in-plane and out-of-plane fluctuations. This is similar to the case of the kagomé lattice, where all of the zero modes of coplanar classical ground states have divergent fluctuations [8].

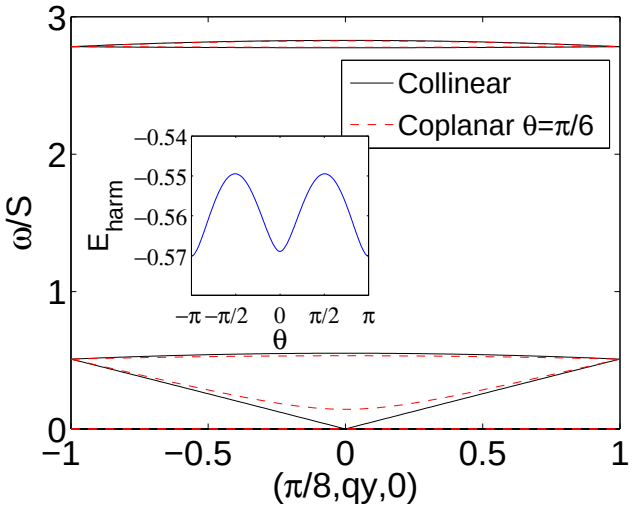

Figure 4.6: Dispersion for coplanar spins.
Dispersion along a line in $\mathbf{q}$ space, for the collinear state shown in Fig. 4.5a (solid lines), as well as the $\theta = \pi/6$ coplanar state (dashed lines), showing that a divergent zero mode at $\mathbf{q} = (\pi/8, 0, 0)$ gains non-zero energy, when the state is taken away from collinearity, while all other modes are virtually unchanged. Inset: Zero-point energy of the same state with the spins along the AFM x-y diagonal rotated by angle $\pm\theta$. The minimum energy is for the collinear states.

On the other hand, the divergent zero modes $\mathbf{w}_d$ of the collinear states, become (non-divergent) nonzero modes when the spins are rotated out of collinearity. If a loop in a collinear state is rotated, as in (4.19), by $\pm\theta$, we find that the divergent modes' frequency increases *linearly* with θ [6, 7]. However, after integration over the Brillouin zone, the rise in total zero-point energy is quadratic in θ. This rise in the divergent modes' zero-point energy is the reason that each collinear classical ground state has *lower* energy than nearby coplanar states.

In the main part Fig. 4.6, we see that the most significant difference in the dispersion between collinear and non-collinear states, is the gap formed in some of the zero modes along the divergence lines. The *change* in the contribution of the optical modes to $\frac{1}{2}\sum\omega$ is negligible compared to this gap, for all cases that we

looked at.[3]

Looking at further rotation of spins out of a *coplanar* arrangement, i.e. rotation of a loop or line by angles $\pm\phi$, one finds numerically that some of the (now divergent) zero modes gain non-zero frequency, proportional to $|\phi|$, as for the kagomé lattice [6, 7], and the energy increase is $\mathcal{O}(\{\phi_i\})$.

While we have shown that collinear states are local minima of the energy landscape, we have not ruled out the possibility that a non-collinear state would be a local (or even global) minimum. Although we do not believe this to be the case, further work would be required to prove so.

[3]We note that $\sum \omega_m^2 \propto \mathrm{Tr}(\mu^2)$ can be shown to be independent of the classical ground state (collinear or not). On the other hand $\sum \omega_m^4$ attains (the same) maximum for all collinear states. This is consistent with the argument of Ref. [9] that collinearity generally maximizes the spectrum's dispersion. That makes it plausible that $\sum \omega_m$ has a minimum.

BIBLIOGRAPHY

[1] O. Tchernyshyov, H. Yao, and R. Moessner, Phys. Rev. B **69**, 212402 (2004).

[2] M. Eckstein, M. Kollar, K. Byczuk, and D. Volhardt, Phys. Rev. B **71**, 235119 (2005).

[3] C. L. Henley, Phys. Rev. Lett. **96**, 047201 (2006).

[4] F. H. Stillinger and M. A. Cotter, J. Chem. Phys. **58**, 2532 (1973).

[5] D. A. Huse and A. D. Rutenberg, Phys. Rev. B **45**, R7536 (1992).

[6] I. Ritchey, P. Chandra, and P. Coleman, Phys. Rev. B **47**, R15342 (1993).

[7] J. von Delft and C. L. Henley, Phys. Rev. B **48**, 965 (1993).

[8] A. Chubukov, Phys. Rev. Lett. **69**, 832 (1992).

[9] C. L. Henley, Phys. Rev. Lett. **62**, 2056 (1989).

Chapter 5

Effective Hamiltonian for related models

The loop expansion of Sec. 4.1 can be easily be adapted to study similar models that support collinear ground states including the pyrochlore Heisenberg model with a large applied magnetic field and the Heisenberg model in closely related lattices, as we shall show in Secs. 5.1 and 5.2, respectively. In this chapter we derive an effective Hamiltonian for several such models, and in each case discuss the nature of the (harmonic) ground states and the zero temperature entropy.

For the purpose of determining the ground state manifold, we find it convenient to recast the effective Hamiltonian $E^{\rm eff}_{\rm harm}$ of Eq. (4.6) as an Ising model in the *complementary lattice*. This is a lattice composed of the centers of the shortest loops, or *plaquettes*, in the original lattice. In the pyrochlore lattice, the complementary lattice sites are the centers of the hexagons, and form another pyrochlore lattice. To each complementary lattice site a, we assign an Ising spin $\tilde{\eta}_a$, equal to the product of the direct lattice sites around the corresponding plaquette, i.e, the flux φ_a through the plaquette:

$$\tilde{\eta}_a \equiv \prod_{i\in a} \eta_i = \varphi_a \,, \tag{5.1}$$

where the product is on all sites in the (direct lattice) plaquette a. Since any loop product can be written as a product of spin products around plaquettes, the terms Φ_{2l} in Eq. (4.6) are now represented by simpler (at least for small l) expressions, in terms of the complementary lattice spins

$$E^{\rm eff}_{\rm harm} = \mathcal{E}_0 + S\mathcal{B}\sum_a \tilde{\eta}_a + S\mathcal{J}\sum_{\langle ab\rangle} \tilde{\eta}_a\tilde{\eta}_b + S\mathcal{J}'\sum_{\langle\langle ab\rangle\rangle} \tilde{\eta}_a\tilde{\eta}_b + S\mathcal{J}_3\sum_{\triangle abc} \tilde{\eta}_a\tilde{\eta}_b\tilde{\eta}_c + \cdots \,, \tag{5.2}$$

where $\langle\cdots\rangle$ and $\langle\langle\cdots\rangle\rangle$ represent nearest neighbors and next-nearest neighbors on

the complementary lattice, respectively, and the $\triangle$ sum is over 3-spin plaquettes. Comparing to Eq. (4.6), we can identify, for the pyrochlore, $\mathcal{E}_0 \equiv E_0$, $\mathcal{B} \equiv K_6/S$, $\mathcal{J} \equiv K_8/2S$, $\mathcal{J}' \equiv K_{10}/S$, $\mathcal{J}_3 = 0$. The 1/2 factor in $\mathcal{J}$ stems from the fact that each loop of length eight in the pyrochlore has two different representations as a product of two hexagons. We are free to choose $\mathcal{J}_3 = 0$, because in pyrochlore complementary lattice the product of three spins of a tetrahedron is equal to the fourth spin in the same tetrahedron. This is due to the dependence, in the direct lattice, between the four hexagons in one super-tetrahedron (see Fig. 3.1b). Thus the $\mathcal{J}_3$ term is already accounted for in the "field" $\mathcal{B}$ term in (5.2). Note that, in the pyrochlore, there are three different types of loops of length 10, and thus, within the approximation that we use to calculate the effective Hamiltonian coefficient (see Sec. 4.1.3 and Appendix A.2), there should be two more terms [not shown in Eq. (5.2)]. with coefficients equal to $\mathcal{J}'$.

Writing the effective Hamiltonian in terms of the complementary lattice spins is manifestly gauge invariant, since the complementary spins $\tilde{\eta}_a$ are not modified by gauge transformations. In the pyrochlore Heisenberg model, we found in Sec. 4 a ferromagnetic nearest neighbor interaction $\mathcal{J}$, with a positive field $\mathcal{B}$, resulting in a uniform complementary lattice ground state in which $\tilde{\eta}_a = -1$ for all a (the π-flux state). This unique complementary lattice state corresponds to the family of direct lattice ground states satisfying Eq. (4.12).

5.1 Non-zero magnetic field

We now consider what happens to the loops expansion when a magnetic field is applied to the system. Since quantum fluctuations favor collinear spins, one generically expects the magnetization to field curve to include plateaus at cer-

tain rational values of the magnetization, corresponding to collinear spin arrangements [1, 2, 3, 4, 5]. Thus, at one certain value of the field $\vec{B}$, such that $\vec{B}/2J$ is an integer, the classical ground states satisfy, for all tetrahedra α

$$\sum_{i\in\alpha} \mathbf{S}_i = MS\,. \tag{5.3}$$

for some non-zero magnetization M. If it is classically allowed (given M and the number of spins in the simplex), then the harmonic spin-waves would favor collinear spin arrangements satisfying

$$\sum_{i\in\alpha} \eta_i = M\,, \qquad \forall \text{ simplexes } \alpha\,. \tag{5.4}$$

These are the new collinear classical ground states in this theory and, like the zero-field case, they are typically highly degenerate. Now the question we ask is which of these are selected by harmonic quantum fluctuations. Repeating the derivation of the loop expansion (4.4), we now find that the diagonal elements of $\mathbf{H}$ change, as now Eq. (2.16) is modified to $\mathbf{H} = \frac{1}{2}\mathbf{W}^\dagger\mathbf{W} - \boldsymbol{\eta}M$. Writing down the equations of motion in terms of the diamond lattice, as before, we find that the zero-point energy can still be written as $\mathrm{Tr}\,(\boldsymbol{\mu}^2)^{1/2}$, as in Eq. (4.1), but that the diagonal elements of $\boldsymbol{\mu}$ are all non-zero and equal to $-M$. In order to remove these diagonal elements, we can define

$$\boldsymbol{\mu}_0 \equiv \boldsymbol{\mu} + M\mathbb{1}\,, \tag{5.5}$$

where $\boldsymbol{\mu}_0$ is equal to the $M = 0$ value of $\boldsymbol{\mu}$ as defined in Eq. (4.2), and, as before, it only connects nearest neighbor tetrahedra. The loop expansion is now

$$\begin{aligned} E_{\text{harm}} &= S\,\mathrm{Tr}\left(A\mathbb{1} + \left(\frac{(\boldsymbol{\mu}_0 - M\mathbb{1})^2}{4} - A\mathbb{1}\right)\right)^{1/2} - SN_s + |M|N_z S \\ &= S\sqrt{A}\sum_{n=0} C_n\,\mathrm{Tr}\left(\frac{(\boldsymbol{\mu}_0^2 - 2M\boldsymbol{\mu}_0) + (M^2 - 4A)\mathbb{1}}{A}\right)^n - SN_s + |M|N_z S \\ &= S\sqrt{A}\sum_{n=0}^{\infty}\frac{C_n}{A^n}\sum_{k=0}^{n}\sum_{j=0}^{n-k}\begin{pmatrix} n \\ k\,j \end{pmatrix}(M^2 - 4A)^{n-k-j}(-2M)^j\,\mathrm{Tr}\,\boldsymbol{\mu}_0^{2k+j} \\ &\quad -SN_s + |M|N_z S\,. \end{aligned} \tag{5.6}$$

Here N_z is the number of zero modes of $\mathbf{W}^\dagger\mathbf{W}$, i.e. $N_s/2$ for the pyrochlore lattice. Now the calculation goes as in Sec. 4.1, noting that the trace is non-zero only for even j. When one re-sums the terms in Eq. (5.6) to construct an effective Hamiltonian of the form (4.6), one finds that, unlike the $M = 0$ case, where always $\mathrm{sgn}(K_{2l}) = (-1)^{l+1}$, the signs of the expansion terms are no longer easy to predict.

Applying this calculation to the only non-trivial collinear case on the pyrochlore lattice, i.e., $M = 2$, and rearranging the terms in the form (5.2), we find (see Tab. 5.1) that $\mathcal{B} < 0$, and that the coefficient of the interaction terms, $\mathcal{J}$, is two orders of magnitude smaller than the effective field $\mathcal{B}$. Therefore the complementary lattice ground state is a uniform $\tilde{\eta}_a = 1$ state, corresponding to the family of states with positive hexagon products (zero-flux states).

As in the zero magnetization case, studied in chapters 2–4, the harmonic energy is invariant under any gauge transformation that flips the spins in a set of tetrahedra, while conserving the constraint (5.4). However, it is clearly much harder, in this case, to construct a transformation in this way, because a single tetrahedron flip violates the constraint not just on the neighboring tetrahedra, but on the flipped tetrahedron itself as well. Therefore one would expect the ground state

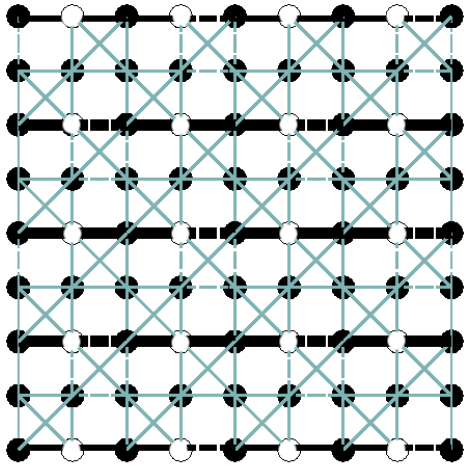

Figure 5.1: Pyrochlore $M = 2$ ground state.
{001} projection of a pyrochlore lattice $M = 2$ zero-flux ground state. Each tetrahedron has three up spins (solid circles) and one down spin (empty circle). This is the ground state with the smallest possible (four-site) magnetic unit cell. The dark lines show x-z planes (coming out of the page), that can each by flipped independently to obtain a valid zero-flux $M = 2$ state. Since there are $\mathcal{O}(L)$ such planes, the ground state entropy is at least of order L.

degeneracy for this model to be smaller than for the $M = 0$ case.

It is easy to show that still, the ground state entropy is *at least* of order L, by observing that in the simplest ground state, with a 4 site unit cell, one can construct gauge transformations by independently flipping some of $\mathcal{O}(L)$ parallel planes, each composed e.g. of parallel AFM lines in the x-z plane (see Fig. 5.1). The keys to these transformations being valid are: (i) The spin-product around any hexagon (and therefore any loop) in the lattice is not affected by it. (ii) Since AFM lines are flipped, the spin sum on each tetrahedron remains the same.

5.2 Other lattices

The calculation of the loop expansion is actually quite general and can be applied on any lattice composed of corner-sharing simplexes, as long as the classical ground state is collinear, and the (zero field) Hamiltonian has the form (2.16). We have implicitly assumed that the *simplex lattice*, formed by centers of simplexes, is bipartite, although we could easily modify the calculation to take care of a more general case. Given these assumptions, the only lattice information relevant to our calculations is the coordination z of the simplex lattice and the lengths of the various loops in the same lattice. In most cases, the coordination of the simplex lattice is equal to the number of sites in a single simplex, e.g. $z = 4$ for the pyrochlore, or 3 for the kagomé. However the expansion works equally well for cases where not every lattice site is shared by two simplexes, as in the *capped kagomé* model below, in which case z is smaller than the number of sites in a simplex.

In general, we find numerically, that in going from $z = 4$ to $z = 3$, the convergence rate of the Bethe lattice calculation becomes slower and the value of of the parameter A at which convergence is obtained is smaller. The accuracy of our Bethe lattice approximation is expected to be better for larger values of z, since there are relatively fewer uncounted paths.

5.2.1 Checkerboard lattice

The checkerboard lattice is also often called the planar pyrochlore, and is a two-dimensional projection of the pyrochlore lattice [6, 7]. It is composed of "tetrahedra" (crossed squares) whose centers form a square lattice (see, e.g. the {001}

projections of the pyrochlore in Figs. 3.1a,3.2,3.3,4.5). Aside from the dimensionality, a major difference between the checkerboard and the pyrochlore lattice is that in the checkerboard, not all of the "tetrahedron" bonds are of the same length, and thus one would generally expect coupling $J' \neq J$ along the square diagonals. Nevertheless, to pursue the frustrated analog of the pyrochlore, we shall consider here the case $J' = J$.

As in the diamond lattice, the coordination of the (square) simplex lattice is $z = 4$, and therefore the calculation of approximate loop expansion coefficients, is identical to the pyrochlore calculation of Sec. 4.1. However, we should note that since the shortest loops are now of length 4, the error in our Bethe lattice approximation is greater than in the pyrochlore case, since the "repeated loops" that we ignore carry more significant weight. Nevertheless, the ignored terms are still expected to be two orders of magnitude smaller than the Bethe lattice terms.

In the checkerboard case, the complementary lattice is a square lattice composed of the centers of the empty square plaquettes. Now the effective field in Eq. (5.2) is the coefficient due to loops of length four $\mathcal{B} = K_4/S < 0$, which prefers $\tilde{\eta}_a > 0$, or in other words, zero-flux order. While the nearest neighbor complementary lattice coupling is antiferromagnetic $\mathcal{J} = K_6/S > 0$ and competes with $\mathcal{B}$, it is not strong enough (see Tab. 5.1) to frustrate the uniform zero-flux order.

The ground state entropy of the checkerboard lattice, has been shown in Ref. [8] to be of order L, by construction of all of the possible even and odd gauge transformations on a particular reference zero-flux state. A simple explanation for the degeneracy is that, given a line of spins, say in the x direction, there are, at most, two choices in the construction of an adjacent parallel line. This is because there is one constraint on each tetrahedron (two down-spins) and one on each plaquette

(an even number of down-spins). Thus, starting from an arbitrary choice of one horizontal line (2^L choices), there are $\leq 2^L$ ways of constructing the rest of the lattice. The resultant entropy is $\mathcal{O}(L)$.

Applying a magnetic field that induces the $M = 2$ plateau, we find (Tab. 5.1), that the complementary lattice effective Hamiltonian has $\mathcal{B} > 0$, $\mathcal{J} < 0$, favoring the π-flux uniform state. The ground state entropy in this case is also of order L. To show this, we note that there is only one down-spin in each tetrahedron when $M = 2$, and that the spin product around each plaquette is -1. This means that there must be exactly one down-spin around each plaquette.

We could use an argument similar to the one used in the $M = 0$ model, to find the entropy in this model. A more elegant argument uses a one-to-one correspondence between the ground states and *complete* tiling the checkerboard lattice with squares of size $2a \times 2a$, where a is the size of each plaquette (and "tetrahedron"). Here each square is centered on a down-spin and covers the two plaquettes and two tetrahedra to which it belongs (see Fig. 5.2. The entropy of such tilings is clearly of order L.

5.2.2 "Capped kagomé"

The kagomé lattice Heisenberg model has been one of the most studied highly frustrated models. The lattice is two dimensional, and is composed of corner sharing triangles, such that the centers of the triangles form a honeycomb simplex lattice. This model too is closely related to the pyrochlore, as a (111) projection of the pyrochlore lattice contains kagomé planes sandwiched between triangular planes, such that the triangular lattice sites "cap" the kagomé triangles to form tetrahedra.

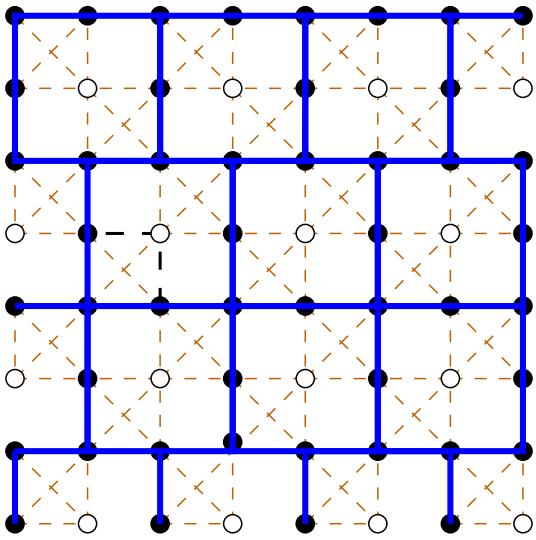

Figure 5.2: Mapping checkerboard $M = 2$ ground states to tilings.
The checkerboard $M = 2$ ground states (π-flux states) can be mapped to tilings of the lattice with squares. Each square covers two "tetrahedra" and is centered on a down-spin (open circle). The entropy of such tilings in trivially of order L.

We cannot apply our collinear loop expansion to the kagomé Heisenberg model, with no applied field, because there are no collinear states that can satisfy the zero triangle-sum rule. One way to consider a "collinear kagomé" is to look at a *capped kagomé* lattice which consists of a kagomé, flanked by two triangular lattices, so that each triangle turns into a tetrahedron, with equal bonds. This model was studied by Tchernyshyov et. al. [9], who referred to it as a "[111] slice of pyrochlore". Those authors found that the ground state is one in which one out of every four hexagons has a positive spin product (the 2×2 *state* shown in Fig. 5.3a). Surprisingly, the Hamiltonian for this model can be written in matrix form with $\mathbf{H} = \frac{1}{2}\mathbf{W}^\dagger\mathbf{W}$ [Eq. (2.16)], and therefore we expect our loop expansion to work. Furthermore, as long as there is no applied field, $\mathcal{B} = K_6/S$ is positive, so applying our intuition based on the previously discussed models, we would naively think that the ground state should be a π-flux state.

However, this is the one model that we have studied, where the complementary lattice effective Hamiltonian has interaction terms strong enough to resist the $\mathcal{B}$ field term. Here, the complementary lattice nearest neighbor term corresponds to loops of length 10 and therefore $\mathcal{J} > 0$ (there are no loops of length 8 in the kagomé), and $\mathcal{J}' = K_{12}/S < 0$.

In the π-flux state, all complementary lattice spins are -1, and thus while the $\mathcal{B}$ term in Eq. (5.2) is optimized, all of the nearest neighbor bonds ($3N_s^c$, where N_s^c is the number of complementary lattice sites) are violated, as well as all of the 3-site terms ($2N_s^c$). On the other hand, the 2×2 state has only $N_s^c/4$ negative spins, but half of the complementary lattice bonds and 3/4 of the three-spin terms are satisfied. Applying the coefficients we obtained (from Tab. 5.1, $\mathcal{J}/\mathcal{B} \approx 0.14$), and including also the next order (K_{12}) term $\mathcal{J}_3/\mathcal{B} \approx -0.05$) to the expansion, we find the energy per complementary-lattice site

$$\frac{E_{\rm harm}^{\pi-{\rm flux}} - E_{\rm harm}^{2\times 2}}{SN_s^c} \approx -0.5\mathcal{B} + 3\mathcal{J} - 3\mathcal{J}_3 \approx 0.0026 > 0\,, \tag{5.7}$$

and we find that the 2×2 state is favored over the π-flux state [9]. We provide this calculation as an illustration of the difficulty in using the effective Hamiltonian in a model with an unusually frustrated complementary lattice. In order to actually determine the ground state in this case, one must include further terms in the effective Hamiltonian. In fact, based only on the terms included in Eq. (5.7), we would conclude, mistakenly, that the complementary lattice ground state is the $\sqrt{3} \times \sqrt{3}$ *state* (not to be confused with the well-known coplanar kagomé ground state with the same ordering vector), where 1/3 of the (in plane) spins are up, so that each triangular plaquette has two down spins and one up spin (see Fig. 5.3b). However, based on numerical diagonalization, we find that both the 2×2 state and the π-flux state have, in fact, lower energy than the $\sqrt{3} \times \sqrt{3}$ state, in agreement

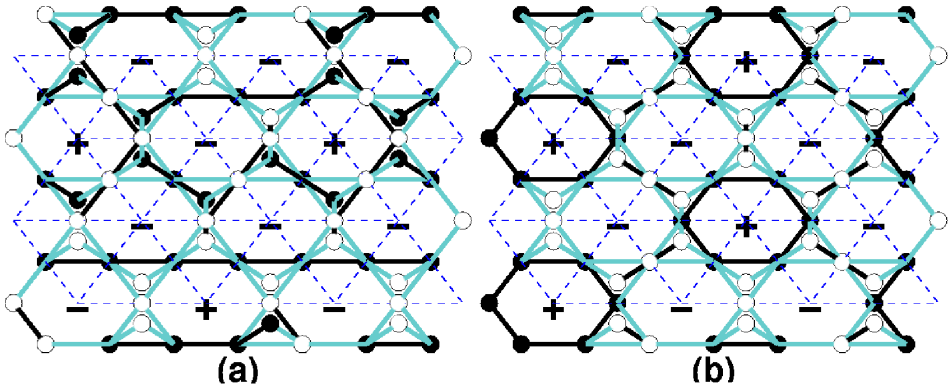

Figure 5.3: "Capped kagomé" states.
(a) The 2×2 ground state of the "capped kagomé" lattice. (b) The $\sqrt{3} \times \sqrt{3}$ state in the same lattice. Up (down) spins are marked by solid (open) circles, and FM (AFM) lattice bonds are shown as dark (light) lines. The dashed lines represent the complementary lattice bonds, whose sites are marked + and −.

with Ref. [9].

Due to the large number of degrees of freedom in this model, arising from the "free" spins capping each triangle, there is an extensive number of 2×2 ground states, as has been calculated in Ref. [9].

5.2.3 Kagomé with applied field

Another way of obtaining a "collinear kagomé" model, is to apply a field strong enough to induce collinear states with $M = 1$ on the (standard) kagomé lattice [4, 10]. Applying our expansion, we find $\mathcal{B} < 0$ and $\mathcal{J} < 0$ (see Tab. 5.1), consistent with a uniform zero-flux ground state, as we have indeed confirmed by numerically calculating the zero-point energy.

In the $M = 1$ kagomé model, zero-flux states are obtained by spin arrangements in which there are exactly two down-spins around each hexagon. To find the ground state entropy, we map these to a dimer covering of the (triangular) complementary

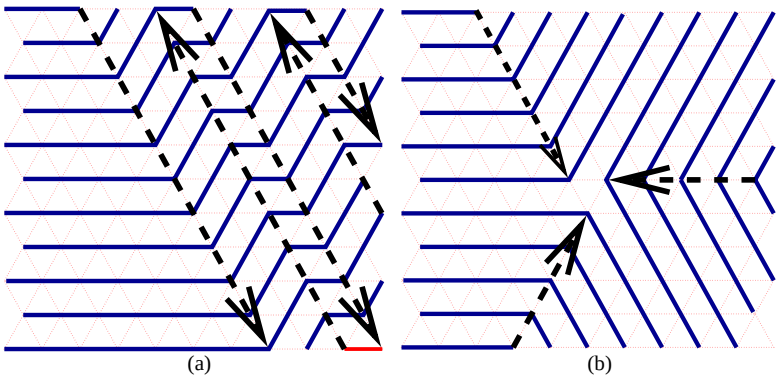

Figure 5.4: Counting $M = 1$ kagomé ground states by mapping.
The $M = 1$ kagomé model ground states can be mapped one-to-one to continuous lines on triangular lattice, such that a line can turn, at each site by $\pm 60°$ or $0°$. The "kinks" in each lines must lie along directed defect lines (dashed lines). There are two possible cases: (a) parallel defects alternating in directions. (b) three lines meeting at a point defect (and no other kinks).

lattice, in which there are exactly 2 dimers touching each complementary lattice site, and there is exactly 1 dimer in each plaquette. These can be viewed as continuous lines on the triangular lattice, that can turn at each node by $\pm 60°$ or $0°$. Since there is no way of closing such lines into loops, one finds that they generally run in parallel, possibly turning by $60°$ to form a "directed line defect". Three such line defects can meet and terminate at a single plquette, as long as they form $120°$ angles and are all directed into this "point defect". Thus, each ground state either has exactly one point defect and three line defects coming into it (and no others), as in Fig. 5.4b, or parallel line defects (alternating in direction), as in Fig. 5.4a, allowing for entropy of order L.

Table 5.1: Effective Hamiltonian (5.2) coefficients for the models we consider. The coefficients were obtained by the expansion (5.6), with $n \geq 30$ and extrapolated to $n \to \infty$. The complementary lattice ground state is given in the right column, and it corresponds, in all cases, to a family of states in the direct lattice.

Lattice	Complementary lattice	M	$\mathcal{B}$	$\mathcal{J}$	Ground state
pyrochlore	pyrochlore	0	$+0.0136$	-0.0016	π-flux
pyrochlore	pyrochlore	2	-0.0091	-0.00007	0-flux
checkerboard	square	0	-0.0649	$+0.0136$	0-flux
checkerboard	square	2	$+0.0342$	-0.0091	π-flux
capped kagomé	triangular	0	$+0.0376$	$+0.0052$	2×2
kagomé	triangular	1	-0.0173	-0.0037	0-flux

BIBLIOGRAPHY

[1] H. Ueda *et al.*, Phys. Rev. Lett. **94**, 047202 (2005).

[2] K. Penc, N. Shannon, and H. Shiba, Phys. Rev. Lett. **93**, 197203 (2004).

[3] D. L. Bergman, R. Shindou, G. A. Fiete, and L. Balents, cond-mat/0510202 (unpublished).

[4] M. E. Zhitomirsky, A. Honecker, and O. A. Petrenko, Phys. Rev. Lett. **85**, 3269 (2000).

[5] S. R. Hassan and R. Moessner, cond-mat/0512594 (unpublished).

[6] E. H. Lieb and P. Schupp, Phys. Rev. Lett. **83**, 5362 (1999).

[7] B. Canals, Phys. Rev. B **65**, 184408 (2002).

[8] O. Tchernyshyov, O. A. Starykh, R. Moessner, and A. G. Abanov, Phys. Rev. B **68**, 144422 (2003).

[9] O. Tchernyshyov, H. Yao, and R. Moessner, Phys. Rev. B **69**, 212402 (2004).

[10] M. E. Zhitomirsky, Phys. Rev. Lett. **88**, 057204 (2002).

Chapter 6

Anharmonic spin-waves

In Ch. 4 we found that the harmonic spin-wave theory has a large family of degenerate collinear ground states. These states are related by a gaugelike transformation and are known as the π-flux states, because the product $\varphi_{\mathcal{L}} = \prod \eta_i$ around each hexagon in the lattice is -1. We now attempt to resolve this degeneracy by taking the next order (in $1/S$) in the spin-wave expansion.

This chapter is organized as follows: in Sec. 6.1 we derive the quartic-order term in the Holstein-Primakoff large-S expansion, assuming a collinear classical ground state. We then derive a self-consistent mean-field Hamiltonian for the anharmonic theory.

Then, in Sec. 6.2 we use a simple example – the (π, π) state on the two-dimensional checkerboard lattice– in order to gain some analytic intuition on the behavior of the bond variables that govern the mean-field quartic energy, and the scaling laws involved. We find that these diverge as $\ln S$, resulting in anharmonic energy of order $(\ln S)^2$. We argue that among all harmonic checkerboard ground states, the quartic energy is minimized in the (π, π) state and prove this to be true within a set of checkerboard lattice harmonic ground states.

In Sec. 6.3 we present the main results of this chapter – numerical results for the pyrochlore lattice. We find that, as in the checkerboard, the quartic energy scales as $(\ln S)^2$. We calculate the anharmonic energy for a large set of harmonic ground states and show that the anharmonic theory breaks the degeneracy between them. We numerically fit effective Hamiltonians for both the gauge-invariant and gauge-dependent terms in the quartic energy, and find a set of seemingly degenerate

ground-states.

6.1 Self-consistent theory

In Ch. 2, we wrote down the harmonic-order Hamiltonian, for collinear states, in matrix form

$$\mathcal{H}_{\rm harm} = \vec{\boldsymbol{\sigma}}^{\dagger} \begin{pmatrix} \mathbf{H} & \mathbf{0} \\ \mathbf{0} & \mathbf{H} \end{pmatrix} \vec{\boldsymbol{\sigma}} - SN_S \,, \tag{6.1}$$

where the matrix elements of $\mathbf{H}$ satisfy $H_{ii} = 1$ and $H_{ij} = J_{ij}/2$ [$J_{ij} = 1$ for nearest neighbors (i, j) and zero otherwise], N_s is the number of lattice sites, and $\vec{\boldsymbol{\sigma}}$ is a vector of length $2N_s$: $\vec{\boldsymbol{\sigma}}^{\dagger} = ((\boldsymbol{\sigma}^x)^{\dagger}, (\boldsymbol{\sigma}^y)^{\dagger})$.

Here we carry the Holstein-Primakoff expansion to the next order, in $1/S$ to obtain the quartic-order Hamiltonian $\mathcal{H}_{\rm quart}$. We then decouple it to derive a mean-field Hamiltonian similar in form to (6.1). To solve it we propose a self-consistent variational Hamiltonian.

6.1.1 Mean field Hamiltonian

If we continue the Holstein-Primakoff expansion of Ch. 2 to the next order is $1/S$, for a collinear classical configuration, we obtain the anharmonic term in (1.4)

$$\begin{aligned} \mathcal{H}_{\rm quart} &= \frac{1}{8S^2} \sum_{ij} J_{ij} \left[2\eta_i\eta_j((\sigma_i^x)^2 + (\sigma_i^y)^2)((\sigma_j^x)^2 + (\sigma_j^y)^2) \right. \\ &- \sigma_i^x((\sigma_j^x)^3 + \sigma_j^y\sigma_j^x\sigma_j^y) - \sigma_j^x((\sigma_i^x)^3 + \sigma_i^y\sigma_i^x\sigma_i^y) \\ &- \left. \sigma_i^y((\sigma_j^y)^3 + \sigma_j^x\sigma_j^y\sigma_j^x) - \sigma_j^y((\sigma_i^y)^3 + \sigma_i^x\sigma_i^y\sigma_i^x) \right] . \end{aligned} \tag{6.2}$$

In order to calculate the anharmonic corrections to the energy, for an arbitrary given state, parameterized by $\{\eta_i\}$, we develop a mean field approach. We can obtain a Hartree-Fock-like mean field Hamiltonian by decoupling the quartic term

of the Hamiltonian (6.2) (see Appendix D). We write the mean-field form of $\mathcal{H}_{\rm quart} + \mathcal{H}_{\rm harm}$ in matrix form, in analogy with the Harmonic Hamiltonian (6.1)

$$\mathcal{H}_{\rm MF} = \vec{\boldsymbol{\sigma}}^{\dagger} \begin{pmatrix} \mathbf{H}_{\rm MF} & \mathbf{0} \\ \mathbf{0} & \mathbf{H}_{\rm MF} \end{pmatrix} \vec{\boldsymbol{\sigma}} - SN_s \,, \tag{6.3}$$

where the matrix elements can be written in terms of the correlations $G_{ij} = \langle \sigma_i^x \sigma_j^x \rangle = \langle \sigma_i^y \sigma_j^y \rangle$

$$(H_{\rm MF})_{ii} = 1 + \frac{1}{2S^2} \sum_j J_{ij} \left(\eta_i \eta_j G_{jj} - G_{ij} \right) , \tag{6.4}$$

$$(H_{\rm MF})_{ij} = \frac{1}{2} J_{ij} \left[1 - \frac{1}{2S^2} (G_{ii} + G_{jj} - 2\eta_i \eta_j G_{ij}) \right] \tag{6.5}$$

We have thus taken the interacting spin-wave Hamiltonian and decoupled it to obtain a non-interacting theory. Unfortunately, even this problem is not easy to solve, since the Hamiltonian matrix elements are written in terms of the correlations $\{G_{ij}\}$, which are unknown. We cannot use the correlations obtained from the bare Harmonic theory (6.1) for both practical reasons (G_{ij} diverges) and substantial ones: the theory would not be self-consistent – we would not recover the same correlations as those we put into it. Our solution will therefore be based on correlation functions that we obtain, self-consistently, from a variational Hamiltonian.

6.1.2 Variational Hamiltonian

To self-consistently solve the Hamiltonian (6.3), we would like to construct a Gaussian variational wavefunction $\Psi_{\rm var}$ which is the ground state of a variational harmonic Hamiltonian $\mathcal{H}_{\rm var}$. We know the exact mean-field Hamiltonian – the solution to an unconstrained variational problem – has only nearest-neighbor terms, so there is no loss of generality when we restrict out variational search to that

form. (This can be contrasted to the kagomé lattice where, due to cubic terms in the spin-wave expansion, the appropriate variational Hamiltonian had second- or third-nearest-neighbor (Heisenberg) terms [1, 2, 3, 4])

The simplest nontrivial form for the variational Hamiltonian $\mathcal{H}_{\rm var}$ is thus the same as (6.3), but with the diagonal block matrix $\mathbf{H}_{\rm MF}$ replaced by

$$\mathbf{H}_{\rm var} \equiv \mathbf{H} + \delta\boldsymbol{\eta}\mathbf{H}\boldsymbol{\eta} + \varepsilon\mathbb{1}\,. \tag{6.6}$$

where δ and ε are variational parameters. Here, the δ term distinguishes between AFM and FM bonds [i.e. $(H_{\rm var})_{ij} = 1+\delta$ for neighbors with $\eta_i = \eta_j$ and $(H_{\rm var})_{ij} = 1-\delta$ for neighbors with $\eta_i = -\eta_j$]. This is the simplest possible form of a variational Hamiltonian that is consistent with the local spin symmetries.

Spin rotation symmetry requires that the global rotation, associated with the eigenvector $\mathbf{v}_G$, with elements

$$v_G(i) = \frac{\eta_i}{\sqrt{N_s}}\,, \qquad \forall i\,, \tag{6.7}$$

would have zero energy, i.e., $\boldsymbol{\eta}\mathbf{H}_{\rm var}\mathbf{v}_G = 0$. Writing this term by term, we find

$$0 = \eta_i \sum_j (H_{\rm var})_{ij} v_G(j) = 4\delta + \varepsilon \tag{6.8}$$

Thus, if we require invariance to global spin rotation [and assume (6.6)] we end up with only one variational parameter ε. It will become clear in the following, that the correct signs for the parameters are $\varepsilon > 0$, $\delta < 0$.

We diagonalize this Hamiltonian to find a variational wavefunction $\Psi_{\rm var}(\varepsilon)$ and the correlations $\{G_{ij}\}$, and minimize with respect ε (for a given S) the decoupled mean-field energy, from (6.3)

$$E_{\rm MF} = \langle\mathcal{H}_{\rm MF}\rangle = -\sum_{\langle ij\rangle} \eta_i\eta_j \left(\Gamma_{ij} + \Gamma_{ji} - \frac{1}{S^2}\Gamma_{ij}\Gamma_{ji}\right) - SN_s\,. \tag{6.9}$$

Here $\langle ij \rangle$ denotes a sum over nearest neighbors. We defined, for conciseness, the bond variable Γ_{ij}

$$\Gamma_{ij} \equiv G_{ii} - \eta_i \eta_j G_{ij} \,. \tag{6.10}$$

Γ_{ij} is not symmetric and is defined only for (i, j) nearest neighbors (nonzero J_{ij}).

The result of the minimization is that for any value of S there is one unique value of the variational parameter $\varepsilon = \varepsilon^*(S)$ for which the variational wavefunction $\Psi_{\rm var}(\varepsilon^*)$ minimizes $E_{\rm MF}$. We will find, in the following, that $\varepsilon^*(S) \propto \ln S/S$.

6.1.3 Scaling

Within the harmonic theory of Ch. 2, the fluctuations of the spin deviation operators scale as $\langle \sigma_i \sigma_j \rangle = \mathcal{O}(S)$ and therefore, we would expect, from the spin-wave expansion (1.4)

$$E_{\rm harm} = \mathcal{O}(S) \,, \qquad \langle \mathcal{H}_{\rm quart} \rangle = \mathcal{O}(1) \,. \tag{6.11}$$

However, since the fluctuations diverge, $\mathcal{H}_{\rm quart}$ has an infinite expectation. Studies of the kagomé lattice [2, 3, 4] have taught us that, when anharmonic terms are treated self consistently, spin fluctuations of *divergent modes* are renormalized. In the kagomé case $\langle \sigma_i \sigma_j \rangle = \mathcal{O}(S^{4/3})$ and the scaling relations are

$$E_{\rm harm} = \mathcal{O}(S) \,, \qquad \langle \mathcal{H}_{\rm quart} \rangle = \mathcal{O}(S^{2/3}) \,. \tag{6.12}$$

Note that the harmonic energy is not rescaled because the frequency of divergent zero modes is only $\mathcal{O}(S^{2/3})$, which is negligible compared to non-zero modes' $\mathcal{O}(S)$ frequency.

Naïvely, one might expect this scaling argument to carry through to the pyrochlore lattice as well [5]. However, it is important to observe that the dominant

contribution to the anharmonic term in $E_{\rm MF}$ comes from (the vicinity of) the divergent modes, discussed previously in Sec. 3.2. There is a big difference between the divergent modes of the kagomé and the pyrochlore: in the kagomé, due to the anisotropy between in-plane and out-of-plane spin fluctuations, *all* zero modes are divergent modes. In other words, the kagomé divergent modes span the entire Brillouin zone. In the pyrochlore, on the other hand, the divergent modes reside only along lines in the Brillouin zone. In the following, we shall find that this leads to *logarithmic* renormalization of the divergent fluctuations $\Gamma_{ij} = \mathcal{O}(S \ln S)$, resulting in scaling

$$E_{\rm quart} \equiv E_{\rm MF} - E_{\rm harm} = \mathcal{O}((\ln S)^2)\,. \tag{6.13}$$

The singularity of the divergent modes' fluctuations, away from $\mathbf{q} = \mathbf{0}$, is cut off by the variational parameter ε. At $\mathbf{q} = \mathbf{0}$, the divergence of $\langle \sigma_i \sigma_j \rangle$ would be preserved, due to the physical Goldstone mode $\mathbf{v}_G$, but the Goldstone mode's contribution to Γ_{ij} vanishes such that the Goldstone mode does not contribute to the energy at any order in $1/S$. Because it is technically difficult to deal with the divergence of $G_{ij}(\mathbf{q} = \mathbf{0})$ we shall, for now, retain both variational parameters. Thus we will have a handle on the fluctuations until we eventually take the limit $\delta \to -\varepsilon/4$. [We find that $G_{ij}(\mathbf{q} = \mathbf{0}) \sim 1/\sqrt{\varepsilon + 4\delta}$, so that $\varepsilon + 4\delta$ must be chosen to be positive.]

6.1.4 Self-consistency

In order for our theory to be self-consistent, each of the diagonal elements (6.4) should be be independent of i, and the off-diagonal elements (6.5) should depend solely on $\eta_i \eta_j$. Furthermore, we want $(H_{\rm MF})_{ij}/(H_{\rm var})_{ij}$ to be equal for all i, j (for

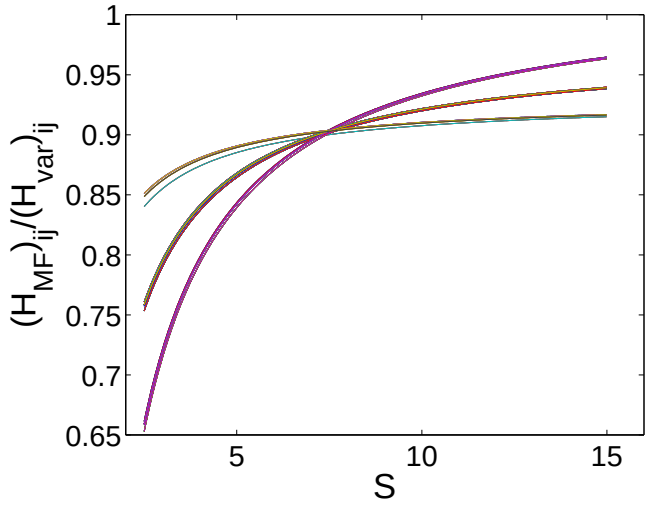

Figure 6.1: Self-consistency of the matrix elements.
We show the ratio of all nonzero elements of $\mathbf{H}_{\rm MF}$ and $\mathbf{H}_{\rm var}(\varepsilon)$ for the state shown in Fig. 4.5(d). Here ε is set to 0.1. Each line represents a particular (ij) matrix element. Up to symmetries of the configuration, there are 11 unique matrix elements elements, some of which are virtually indistinguishable in the plot. All of the lines converge at $S^*(\varepsilon = 0.1) = 7.5$ (up to a deviation which is much smaller than ε)

which $H_{ij} \neq 0$). We indeed find (empirically) that, for a certain value $S = S^*(\varepsilon)$ this is true, i.e.

$$\text{variance}\left[\frac{(H_{\rm MF}(S^*(\varepsilon))_{ij}}{(H_{\rm var}(\varepsilon))_{ij}}\right] \ll \varepsilon\,. \tag{6.14}$$

In Fig. 6.1 we show an example of this for a particular state and a particular value of ε.

The self consistency clearly implies that the relation $S^*(\varepsilon)$ is the inverse of the relation $\varepsilon^*(S)$: If, up to a constant $\mathcal{H}_{\rm MF}(S^*(\varepsilon)) = \mathcal{H}_{\rm var}(\varepsilon)$, then the variational wavefunction $\Psi(\varepsilon)$ minimizes the mean field energy $E_{\rm MF}(S^*(\varepsilon))$. Thus, the self-consistency provides us with an alternative way of finding the value of $\varepsilon^*(S)$.

The mechanism of the self-consistency can be explained as follows: we find

numerically that (for any ε) the ground state wavefunction $\Psi(\varepsilon)$ of $\mathcal{H}_{\rm var}$ satisfies

$$\Gamma_{ij} = \Gamma^{(0)}(\varepsilon) + \Gamma^{(2)}(\varepsilon)\eta_i\eta_j + \Delta\Gamma_{ij}(\varepsilon)\,, \tag{6.15}$$

where $\Gamma^{(0)}$ and $\Gamma^{(2)}$ are independent of i, j (and of order $S\ln\varepsilon$) whereas $\Delta\Gamma_{ij}$ does depend on i and j but is much smaller than $\Gamma^{(2)}$ ($|\Delta\Gamma_{ij}|$ is an order of magnitude smaller that $\Gamma^{(2)}$ for all numerically accessible value of ε). Using the relation (6.15) and Eqs. (6.4) and (6.5), we can write the matrix elements of the mean-field Hamiltonian

$$\begin{aligned}
(H_{\rm MF})_{ij} &= \frac{J_{ij}}{2}\left[1 - \frac{1}{2S^2}(\Gamma_{ij}+\Gamma_{ji})\right] \\
&= \frac{J_{ij}}{2}\left[1 - \frac{1}{S^2}\Gamma^{(0)} - \frac{1}{S^2}\Gamma^{(2)}\eta_i\eta_j - \frac{1}{2S^2}(\Delta\Gamma_{ij}+\Delta\Gamma_{ji})\right] \\
(H_{\rm MF})_{ii} &= 1 + \frac{1}{2S^2}\sum_j J_{ij}\eta_i\eta_j\Gamma_{ji} \\
&= 1 - \frac{1}{S^2}\Gamma^{(0)} + \frac{3}{S^2}\Gamma^{(2)} + \frac{1}{2S^2}\sum_j J_{ij}\eta_i\eta_j\Delta\Gamma_{ji}\,.
\end{aligned} \tag{6.16}$$

In the last line of this equation, we used the $z = 6$ coordination of the pyrochlore lattice, and the classical tetrahedron constraint. We now define

$$J^* \equiv 1 - \frac{1}{S^2}\Gamma^{(0)}\,, \qquad J^*_{ij} \equiv J^* J_{ij}\,, \tag{6.17}$$

and obtain

$$\begin{aligned}
(H_{\rm MF})_{ij} &= \frac{J^*_{ij}}{2}\left(1 + \frac{\Gamma^{(2)}}{\Gamma^{(0)} - S^2}\eta_i\eta_j\right) - \frac{\Delta\Gamma_{ij}+\Delta\Gamma_{ji}}{2S^2} \\
(H_{\rm MF})_{ii} &= J^*\left(1 - 3\frac{\Gamma^{(2)}}{\Gamma^{(0)} - S^2}\right) + \frac{1}{2S^2}\sum_j J_{ij}\eta_i\eta_j\Delta\Gamma_{ji}\,.
\end{aligned} \tag{6.18}$$

For a particular spin length $S = S^*$, such that

$$\frac{\Gamma^{(2)}}{\Gamma^{(0)} - (S^*)^2} = \delta\,, \tag{6.19}$$

(recall that $\delta < 0$ and $\varepsilon = -4\delta$), we find (neglecting terms that are $\ll \delta$)

$$\begin{aligned}(H_{\rm MF})_{ii} &\approx J^*(1+\varepsilon+\delta) = J^*(H_{\rm var})_{ii}\,,\\ (H_{\rm MF})_{ij} &\approx J^*(1+\delta\eta_i\eta_j) = J^*(H_{\rm var})_{ij}\,. \end{aligned} \tag{6.20}$$

Why is our choice of the variational Hamiltonian (6.6) a natural one? The reason is that the correlations that come out of the bare Hamiltonian have the form (6.15) (albeit with divergent $\Gamma^{(0)}$, $\Gamma^{(2)}$) [For motivation of this form, see Appendix E]. For example, if we try a different one-parameter variational Hamiltonian, where we add $\pm\delta$ to the matrix elements $\mathbf{H}_{ij}$ in a pattern other than the one in Eq. (6.6), Γ_{ij} is regularized, but the dominant contribution is still of the form (6.15), and the self-consistency is lost. The only one-parameter nearest-neighbor variational Hamiltonian which is self-consistent is (6.6).

A more elaborate (multi-variabled) self-consistent scheme could improve the quality of the calculation, by exploring a larger set of variational wavefunctions. Nevertheless, as we shall see numerically in of Sec. 6.3, there are clear, degeneracy-breaking effects even within this simple one parameter theory.

6.2 Checkerboard lattice

As a warm-up to the pyrochlore lattice problem, we will first consider the same model on the closely related, two-dimensional checkerboard lattice. The checkerboard lattice (see Fig. 6.2) can be viewed as $\{001\}$ projection of the pyrochlore lattice, and is often called the *planar pyrochlore*. The lattice structure is a square lattice with primitive vectors $\mathbf{a}_1 = (1,1)$, $\mathbf{a}_2 = (1,-1)$ and two sublattices corresponding to basis vectors $\mathbf{u}_1 = (-1/2, 0)$,$\mathbf{u}_2 = (1/2, 0)$. We refer to the crossed squares as "tetrahedra" in analogy with the pyrochlore lattice, and we refer to any

two sites within a tetrahedron as "nearest neighbors" regardless of the actual bond length.

Since the checkerboard lattice, as the pyrochlore, is composed of corner sharing tetrahedra, the derivation of Ch. 2 and Ch. 3 remains valid. Note that we assume that all of the couplings within a tetrahedron are equal, even though in the checkerboard lattice, the various bonds are not related by lattice symmetries. Since the shortest loop in the checkerboard lattice is a square, the effective harmonic Hamiltonian for this lattice has the same form as the pyrochlore harmonic effective Hamiltonian (4.6), with the addition of a dominant term $K_4\Phi_4$, with $K_4 < 0$ [6, 7]. Thus, the harmonic ground states of the checkerboard lattice consist of all the zero-flux states, i.e., states with positive flux in all square plaquettes. Similar to the pyrochlore case, this is a family of states that are exactly degenerate to harmonic order, and in this case residual entropy is $\mathcal{O}(L)$, where L is the linear dimension of the system [7].

6.2.1 The checkerboard (π,π) state

One of the checkerboard harmonic ground states is simple enough for the diagonalization of the variational Hamiltonian (6.6) to be done analytically: the (π, π) state depicted in Fig. 6.2. In this state, the diagonal bonds in each tetrahedron are unsatisfied (FM), such that the symmetry of the lattice is conserved, and the magnetic unit cell has two sites.

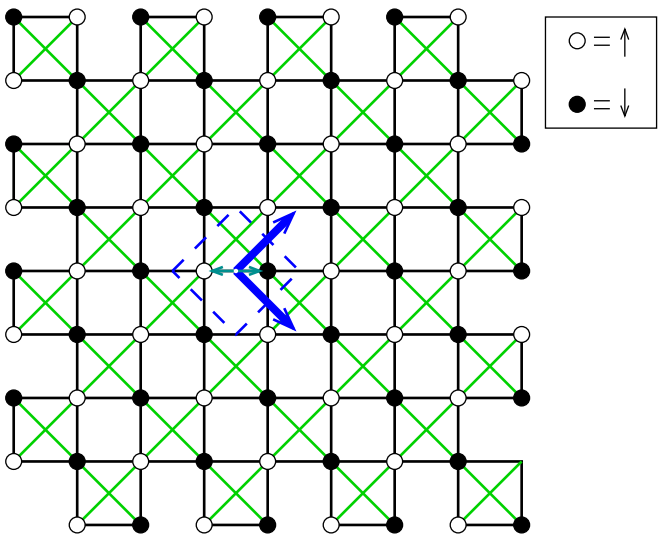

Figure 6.2: The checkerboard lattice (π, π) state.
The primitive vectors are the diagonal arrows, and the primitive unit cell is shown by the dashed square. The small arrows represents the two basis vectors. Here we show the (π, π) state: open (closed) circles denote up (down) spins. Dark (light) colored lines denote AFM (FM) bonds.

Harmonic Hamiltonian

The Fourier transformed harmonic Hamiltonian for the (π, π) state is Eq. (3.15), with

$$\mathbf{H}(\mathbf{q}) = \begin{pmatrix} 2\cos^2 Q_+ & 2\cos Q_+ \cos Q_- \\ 2\cos Q_+ \cos Q_- & 2\cos^2 Q_- \end{pmatrix}, \tag{6.21}$$

where

$$Q_\pm \equiv (q_x \pm q_y)/2\,. \tag{6.22}$$

In Ch. 2 we learned that the spin-wave modes can be found by diagonalizing the matrix $\boldsymbol{\eta}\mathbf{H}(\mathbf{q})$. $\boldsymbol{\eta}$ is a diagonal matrix with elements $\{\eta_i\}$ along the diagonal (in our case $\eta_1 = 1$, $\eta_2 = 2$). Diagonalization of $\boldsymbol{\eta}\mathbf{H}(\mathbf{q})$ produces eigenmodes $\mathbf{V}_\mathbf{q}$ and

$\mathbf{U_q}$ for any wavevector $\mathbf{q}$, with eigenvalues $\lambda_\mathbf{V}$ and $\lambda_\mathbf{U}$, respectively

$$\begin{aligned} \mathbf{V}_\mathbf{q}^T &= \sqrt{\tfrac{2}{\alpha_\mathbf{q}}}(\cos Q_+, -\cos Q_-)\,, \qquad \lambda_V = \beta_\mathbf{q}\,, \\ \mathbf{U}_\mathbf{q}^T &= \sqrt{\tfrac{2}{\alpha_\mathbf{q}}}(\cos Q_-, -\cos Q_+)\,, \qquad \lambda_U = 0\,, \end{aligned} \tag{6.23}$$

satisfying the orthogonality condition $\mathbf{V}_\mathbf{q}^\dagger \boldsymbol{\eta} \mathbf{U}_\mathbf{q} = 0$. Here we defined

$$\begin{aligned} \alpha_\mathbf{q} &= 2(\cos^2 Q_+ + \cos^2 Q_-)\,, \\ \beta_\mathbf{q} &= 2(\cos^2 Q_+ - \cos^2 Q_-)\,. \end{aligned} \tag{6.24}$$

Thus, the ordinary spin-wave band has dispersion $\omega_\mathbf{q} = 2S|\beta_\mathbf{q}|$, and the zero point energy can be easily calculated

$$E_\text{harm} = \frac{1}{2}\sum_\mathbf{q} \omega_\mathbf{q} - N_s S = N_s S\left(\frac{4}{\pi^2} - 1\right)\,. \tag{6.25}$$

The fluctuations of the spin deviation operators ($G_{lm}(\mathbf{q}) = \langle \sigma^x_\mathbf{q}(l)\sigma^x_{-\mathbf{q}}(m)\rangle$, where l and m are sublattice indices) can be calculated from the spin-wave modes by Eq. (2.24)

$$\mathbf{G}(\mathbf{q}) = \frac{S}{2\beta_\mathbf{q}} \begin{pmatrix} \alpha_\mathbf{q} & -\gamma_\mathbf{q} \\ -\gamma_\mathbf{q} & \alpha_\mathbf{q} \end{pmatrix}\,, \tag{6.26}$$

where $\gamma_\mathbf{q} \equiv 4\cos Q_+ \cos Q_-$, so that $\alpha_\mathbf{q} = \sqrt{\beta_\mathbf{q}^2 + \gamma_\mathbf{q}^2}$. Eq. (6.26) shows that the fluctuations diverge wherever $\beta_\mathbf{q}$ vanishes, i.e., along the lines in the Brillouin zone $|Q_+| = |Q_-|$, which turn out to be $q_x = 0$ or $q_y = 0$.

Anharmonic energy

The variational Hamiltonian for the (π, π) checkerboard state is of the form (3.15) with the matrix (6.6) given by

$$\mathbf{H}_\text{var}(\mathbf{q}) = \alpha_\mathbf{q} \boldsymbol{\eta} \mathbf{V}_\mathbf{q} \mathbf{V}_\mathbf{q}^T \boldsymbol{\eta} + \delta\alpha_\mathbf{q} \mathbf{V}_\mathbf{q} \mathbf{V}_\mathbf{q}^T + \varepsilon \mathbb{1}\,, \tag{6.27}$$

Diagonalizing $\boldsymbol{\eta}\mathbf{H}_{\rm var}(\mathbf{q})$, and keeping only the first order terms in δ, ε results in $\omega_{\mathbf{q}}$ of order $\sqrt{\varepsilon}$, $\sqrt{\delta}$ along the divergence lines defined by $\beta_{\mathbf{q}}=0$, and a linear (in ε,δ) correction to $\omega_{\mathbf{q}}$ away from these lines.

The fluctuations of the variational Hamiltonian are now:

$$\mathbf{G}(\mathbf{q})=\frac{S}{2D_{\mathbf{q}}(\varepsilon,\delta)}\begin{pmatrix}\alpha_{\mathbf{q}}(1+\delta)+2\varepsilon & -\gamma_{\mathbf{q}}(1-\delta)\\ -\gamma_{\mathbf{q}}(1-\delta) & \alpha_{\mathbf{q}}(1+\delta)+2\varepsilon\end{pmatrix}. \tag{6.28}$$

Here we defined, for conciseness

$$D_{\mathbf{q}}(\varepsilon,\delta)\equiv\sqrt{\beta_{\mathbf{q}}^2(1-\delta)^2+4(\alpha_{\mathbf{q}}+\varepsilon)(\alpha_{\mathbf{q}}\delta+\varepsilon)}\,. \tag{6.29}$$

The fluctuations diverge (for nonzero ε) only if $\beta_{\mathbf{q}}=0$ *and* $\alpha_{\mathbf{q}}\delta+\varepsilon=0$. If we take $\delta\to-\varepsilon/4$, to conserve the symmetries of the original Hamiltonian, we find one divergent mode: the $\mathbf{q}=\mathbf{0}$ Goldstone mode.

In order to calculate the mean field energy (6.9), we are interested in combinations of the diagonal (on-site) and off-diagonal (nearest neighbor) fluctuations of the form Γ_{ij}. We can write this as a sum over Fourier modes

$$\Gamma_{ij}=\frac{1}{N_M}\sum_{\mathbf{q}}\Gamma_{ij}(\mathbf{q})\,, \tag{6.30}$$

with $\Gamma_{ij}(\mathbf{q})$ defined as

$$\Gamma_{ij}(\mathbf{q})\equiv G_{l_il_i}(\mathbf{q})-\eta_i\eta_jG_{l_il_j}(\mathbf{q})\cos\boldsymbol{\xi}_{ij}\cdot\mathbf{q}\,. \tag{6.31}$$

Here l_i, l_j are the sublattice indices of i and j, respectively, $\boldsymbol{\xi}_{ij}$ is the vector connecting the two sites. N_M is the number of points in the Brillouin zone, i.e. the number of sites in the magnetic lattice.

In this case we obtain, for two neighboring sites on the same sublattice

$$\Gamma_{\uparrow\uparrow}(\mathbf{q}) = \frac{S}{D_{\mathbf{q}}(\varepsilon,\delta)}[\alpha_{\mathbf{q}}(1+\delta)+2\varepsilon]\sin^2Q_+\,, \tag{6.32}$$

$$\Gamma_{\downarrow\downarrow}(\mathbf{q}) = \frac{S}{D_{\mathbf{q}}(\varepsilon,\delta)}[\alpha_{\mathbf{q}}(1+\delta)+2\varepsilon]\sin^2Q_-\,. \tag{6.33}$$

Here we used $\Gamma_{\uparrow\uparrow}(\mathbf{q})$ [shown in Fig. 6.3(a)] for $\Gamma_{ij}(\mathbf{q})$, where both i and j are on the up-spin sublattice (and similarly for $\Gamma_{\downarrow\downarrow}$. For neighboring sites on different sublattices, we obtain [see Fig. 6.3(b)]

$$\Gamma^{x/y}_{\uparrow\downarrow}(\mathbf{q}) = \frac{S}{2D_{\mathbf{q}}(\varepsilon,\delta)}[\alpha_{\mathbf{q}}(1+\delta) + 2\varepsilon - \gamma_{\mathbf{q}}(1-\delta)\cos q_{x/y}]\,, \tag{6.34}$$

where $\Gamma^{x}_{\uparrow\downarrow}$ ($\Gamma^{y}_{\uparrow\downarrow}$) is the bond variable for a bond oriented along the x (y) axis, connecting an up-spin and a down-spin. Note that Eqs. (6.32),(6.33), and (6.34) do not diverge at any value of $\mathbf{q}$ for $\varepsilon + 4\delta = 0$. Thus, we have regularized the fluctuations, and retained only one variational parameter. Since all sites are related by symmetry in this state, $\Gamma_{ij} = \Gamma_{ji}$. Furthermore $\Gamma_{\uparrow\uparrow}(\mathbf{q})$ and $\Gamma_{\downarrow\downarrow}(\mathbf{q})$ are related by a rotation of the Brillouin zone, and the real space correlations will be the same upon integration over the Brillouin zone.

As we can see in Fig. 6.3, the divergent lines for $\Gamma_{\uparrow\uparrow}(\mathbf{q})$ and $\Gamma_{\downarrow\downarrow}(\mathbf{q})$ are both major axes, whereas $\Gamma^{x}_{\uparrow\downarrow}(\mathbf{q})$ and $\Gamma^{y}_{\uparrow\downarrow}(\mathbf{q})$ only diverge along the y and x axes, respectively. Along the divergent lines, where $\beta_{\mathbf{q}} = 0$ and $\alpha_{\mathbf{q}} = |\gamma_{\mathbf{q}}| = 4\cos^2 Q_+$, the values of the bond variables are, asymptotically $\Gamma_{ij}(\mathbf{q}) = S|\sin 2Q_+|/2\sqrt{\epsilon}$. Away from the divergence line,

$$\Gamma_{ij}(\mathbf{q}) \approx \frac{S|\sin 2Q_+|}{2\sqrt{\varepsilon + 4q_\perp^2}}\,, \tag{6.35}$$

where $q_\perp \ll 1$ is transverse to the divergence line. Upon integration of (6.32), (6.33), and (6.34) over the Brillouin zone, the result is a logarithmic singularity in the fluctuations that go into the anharmonic term of (6.9)

$$\Gamma_{\uparrow\uparrow} = \Gamma_{\downarrow\downarrow} = -\frac{4S}{\pi^2}\ln\varepsilon + \mathcal{O}(\varepsilon) = 2\Gamma_{\uparrow\downarrow} + \mathcal{O}(\varepsilon)\,. \tag{6.36}$$

Next, we plug this into Eq. (6.9) for E_{MF}. The terms linear in $\Gamma_{ij}+\Gamma_{ij}$ cancel out at leading order in $1/S$, as there are twice as many AFM bonds as there are FM bonds

and Γ_{ij} is twice as big for FM bonds as it is for AFM bonds. This must be true for *any* checkerboard or pyrochlore state since, from Eq. (6.6) $\langle \mathcal{H}_{\rm var} \rangle = E_{\rm harm} + \mathcal{O}(\varepsilon)$.

The quartic term in the mean field energy $E_{\rm MF}$ is quadratic in $\ln \varepsilon$, resulting in $E_{\rm MF}$

$$\begin{aligned} E_{\rm MF} &= E_{\rm harm} + S \times \mathcal{O}(\varepsilon) - \sum_{\langle ij \rangle} \eta_i \eta_j (\ln \varepsilon)^2 + \mathcal{O}(\varepsilon \ln \varepsilon) \\ &= E_{\rm harm} + S \times \mathcal{O}(\varepsilon) + \frac{4(\ln \varepsilon)^2}{\pi^4} + \mathcal{O}(\varepsilon \ln \varepsilon)\,. \end{aligned} \tag{6.37}$$

Minimizing (6.37) with respect to ε, for a given $S \gg 1$, we obtain $\varepsilon^*(S) \propto \ln S/S$ and therefore the quartic energy $E_{\rm quart} \equiv E_{MF} - E_{\rm harm}$ is quadratic in $\ln S$. We remark that due to the logarithmic singularity, in a numerical calculation one would expect it to be hard to distinguish between terms of order $\mathcal{O}((\ln \varepsilon)^2)$, $\mathcal{O}(\ln \varepsilon)$, and $\mathcal{O}(1)$ for numerically accessible values of ε. Nevertheless, since we are doing a large-S expansion, we are mostly interested in the asymptotic behavior.

6.2.2 Anharmonic ground state selection

Divergent correlations

In order to understand the leading order term in the anharmonic energy, we restrict our discussion to the correlations due to divergent modes. We would like to derive an expression for the divergent part of Γ_{ij}, for any zero-flux state. In order to do so, we need to be more explicit about the divergent modes for these states.

As we saw in Sec. 3.2, a basis of real-space divergent modes $\{\mathbf{v}_d\}$ can be constructed from diamond lattice modes $\{\mathbf{u}_d\}$, each with support on a subset of either the even or odd tetrahedra. For example, for an even mode

$$v_d(i) = \frac{1}{2} \eta_i u_d(\alpha_{\rm even}(i))\,, \tag{6.38}$$

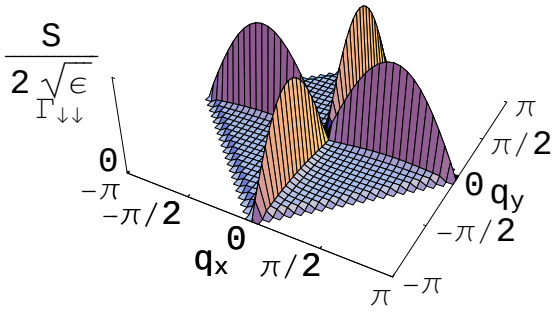

(a)

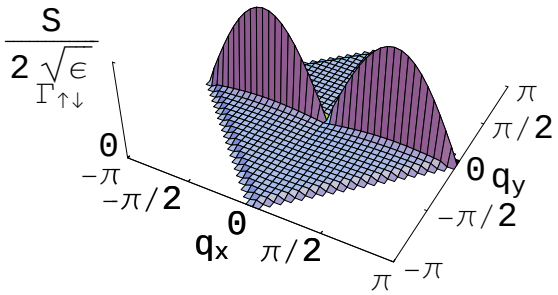

(b)

Figure 6.3: Bond variables in the Brillouin zone of the (π, π) checkerboard state. (a) Γ_{ij} for two neighboring sites on the same sublattice. (b) Γ_{ij} for two neighboring sites with $\eta_i \eta_j = -1$. In the case shown, the (ij) bond is along the x axis. The analytic forms of the functions are given in Eq. (6.32) and Eq. (6.34), respectively.

where $\alpha_{\text{even}}(i)$ is the (unique) even tetrahedron to which site i belongs and u_d is a diamond-lattice mode. For a support network S_d

$$u_d(\alpha) = \begin{cases} \pm 1 & \alpha \in S_d \\ 0 & \text{otherwise} \end{cases} . \tag{6.39}$$

We further showed that the *sign* of $u_d(\alpha)$ (for $\alpha \in S_d$) is determined by a "mock" Ising model: next nearest neighbor (even) diamond sites $\alpha, \beta \in S_d$ have $u_d(\alpha) = u_d(\beta)$ if the bond connecting them is AFM, and $u_d(\alpha) = -u_d(\beta)$ if the bond connecting them is FM [see Eq. (3.13)].

In the checkerboard lattice (π,π) state, we can construct such a basis of real-space divergent modes, such that each mode has support on a horizontal ($\hat{\mathbf{x}}$-oriented) or vertical ($\hat{\mathbf{y}}$-oriented) ladder, living on the square lattice [as in Fig. 6.4]. We label each $\hat{\mathbf{x}}$-oriented mode by its y coordinate $\mathbf{u}_y^{\hat{\mathbf{x}}}$ and similarly, the $\hat{\mathbf{y}}$-oriented modes are labeled by their x coordinate.[1] Since all of the horizontal and vertical bonds in the (π,π) state are AFM, the mock Ising model for this particular state is satisfied by $u_y^{\hat{\mathbf{x}}}(\alpha) = 1$, $u_x^{\hat{\mathbf{y}}}(\alpha) = 1$, for all sites on each ladder.

Considering other zero-flux states, we find that any ladder supports a divergent mode (the support networks S_d are gauge-invariant), but the signs of $\mathbf{u}_y^{\hat{\mathbf{x}}}$, $\mathbf{u}_x^{\hat{\mathbf{y}}}$ are different from the (π,π) case. Looking at the $\hat{\mathbf{x}}$ and $\hat{\mathbf{y}}$ ladders, it is easy to see that, for all checkerboard zero-flux states, one can consistently choose a single value $u_\alpha = \pm 1$ for each tetrahedron so that $u_{y(\alpha)}^{\hat{\mathbf{x}}}(\alpha) = u_{x(\alpha)}^{\hat{\mathbf{y}}}(\alpha) = u_\alpha$.

The "mock Hamiltonian constraint (3.13) on $\{u_\alpha\}$ holds for tetrahedra connected by vertical ($\hat{\mathbf{y}}$) or horizontal ($\hat{\mathbf{x}}$) bonds. This implies that, if i and j are

[1] To be exact, we note that for the basis to be linearly independent, one would have to remove *one* of the ladders from it, since, as mentioned in Sec. 3.2, there in one case of linear dependence between the odd and even modes. This concern has no effect on the discussion, in the thermodynamic limit

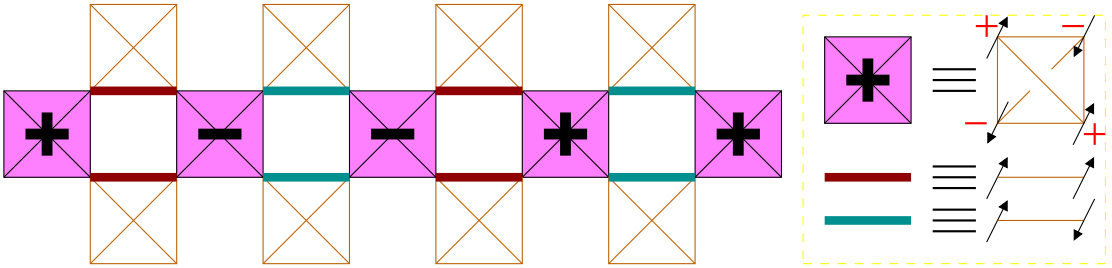

Figure 6.4: Real space "ladder" divergent mode in the Checkerboard lattice. The analog of a planar mode in the checkerboard lattice: a "ladder mode". The large "+" and "-" represent the effective Ising variables $\{u_m(\alpha)\}$, and the thick lines represent the nearest neighbor bonds within the support S_m.

nearest neighbors

$$u_{\alpha_{\rm even}(i)} \times u_{\alpha_{\rm even}(j)} = \begin{cases} -\eta_i\eta_j & (ij)\ \hat{\mathbf{x}} \text{ or } \hat{\mathbf{y}} \text{ bond}; \alpha_{\rm even}(i) \neq \alpha_{\rm even}(j)\,, \\ +\eta_i\eta_j & (ij) \text{ diagonal bond}; \alpha_{\rm even}(i) \neq \alpha_{\rm even}(j)\,, \\ 1 & \alpha_{\rm even}(i) = \alpha_{\rm even}(j)\,. \end{cases} \tag{6.40}$$

Unfortunately, the real-space ladder modes are not mutually orthogonal. Any $\hat{\mathbf{x}}$ ladder has nonzero product with each and every $\hat{\mathbf{y}}$ ladder. To construct an orthonormal basis, we take Fourier combinations of the even and odd $\hat{\mathbf{x}}$ ladders, and of the even and odd $\hat{\mathbf{y}}$ ladders, separately

$$\begin{aligned} u^{\rm even}_{q_x}(\alpha) &= \begin{cases} \frac{2}{\sqrt{N_s}} e^{iq_x x(\alpha)} u_\alpha & \alpha \text{ even}\,, \\ 0 & \text{otherwise} \end{cases}\,, \\ u^{\rm even}_{q_y}(\alpha) &= \begin{cases} \frac{2}{\sqrt{N_s}} e^{iq_y y(\alpha)} u_\alpha & \alpha \text{ even}\,, \\ 0 & \text{otherwise} \end{cases}\,, \end{aligned} \tag{6.41}$$

and similarly for odd modes. The band indices q_x and q_y takes $L/2$ values $2\pi n/L$, with $n = 0, 1, \cdots, L/2-1$, for both odd and even modes. Here L is the length of the system.

The bond variable Γ_{ij} can be written as a sum over these basis divergent modes,

using Eq. (2.24) and Eq. (6.10)

$$\Gamma_{ij} \approx \sum_m \Gamma_{ij}^{(m)} = SC(\varepsilon) \sum_m{}' \left(|v_m(i)|^2 - \eta_i \eta_j v_m^*(i) v_m(j) \right) , \tag{6.42}$$

where the sum $\sum'$ is just over the divergent mode basis and the prefactor $C(\varepsilon) \equiv (2|\mathbf{v}_m^\dagger \boldsymbol{\eta} \mathbf{v}_m|)^{-1}$ would be infinite for $\varepsilon \to 0$. Given that all of the divergent modes are related by lattice symmetries, we assume that $C(\varepsilon)$ is approximately equal, to leading order in $1/\varepsilon$, for all of the divergent modes in our basis. We note that based on Sec. 6.2.1, we know to expect $C(\varepsilon) \propto \ln \varepsilon$, upon integration over the *almost divergent modes*.

Writing Eq. (6.42) in terms of the even and odd Fourier modes, using $v_m(i) = \eta_i u_m(\alpha_i)/2$ [from Eq. (6.38)] we get

$$\begin{aligned} \Gamma_{ij} \;\approx\; & \frac{SC(\varepsilon)}{4} \Bigg\{ \sum_{\mathbf{q}} [|u_{\mathbf{q}}^{\text{odd}}(\alpha_{\text{odd}}(i))|^2 - [u_{\mathbf{q}}^{\text{odd}}(\alpha_{\text{odd}}(i))]^* u_{\mathbf{q}}^{\text{odd}}(\alpha_{\text{odd}}(j))] \\ & + \sum_{\mathbf{q}} [|u_{\mathbf{q}}^{\text{even}}(\alpha_{\text{even}}(i))|^2 - [u_{\mathbf{q}}^{\text{even}}(\alpha_{\text{even}}(i))]^* u_{\mathbf{q}}^{\text{even}}(\alpha_{\text{even}}(j))] \Bigg\} , \end{aligned} \tag{6.43}$$

where $\sum_{\mathbf{q}}$ is shorthand for sum over q_x and q_y.

Plugging the Fourier modes (6.41) into Eq. (6.43) we find

$$\begin{aligned} \Gamma_{ij} \;\approx\; & \frac{SC(\varepsilon)}{N_s} \Bigg\{ \sum_{q_x} \left[1 - u_{\alpha_{\text{odd}}(i)} u_{\alpha_{\text{odd}}(j)} e^{iq_x [x(\alpha_{\text{odd}}(j)) - x(\alpha_{\text{odd}}(i))]} \right] \\ & \quad + \left[1 - u_{\alpha_{\text{even}}(i)} u_{\alpha_{\text{even}}(j)} e^{iq_x [x(\alpha_{\text{even}}(j)) - x(\alpha_{\text{even}}(i))]} \right] \\ & + \sum_{q_y} \left[1 - u_{\alpha_{\text{odd}}(i)} u_{\alpha_{\text{odd}}(j)} e^{iq_y [y(\alpha_{\text{odd}}(j)) - y(\alpha_{\text{odd}}(i))]} \right. \\ & \quad \left. + \left[1 - u_{\alpha_{\text{even}}(i)} u_{\alpha_{\text{even}}(j)} + e^{iq_y [y(\alpha_{\text{even}}(j)) - y(\alpha_{\text{even}}(i))]} \right) \right] \Bigg\} . \end{aligned} \tag{6.44}$$

If i and j are nearest neighbors in, say, an odd tetrahedron, only even modes give nonzero contributions to Γ_{ij}. Summing up the terms and using the mock Ising model constraint (6.40), we get different contributions for diagonal bonds than for

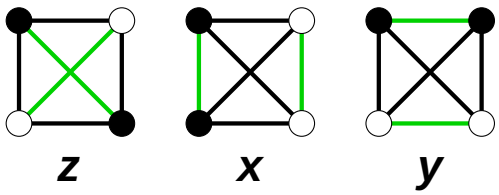

Figure 6.5: The three possible polarization axes for a single tetrahedron.

horizontal or vertical bonds

$$\Gamma_{ij} = \begin{cases} \frac{SC(\varepsilon)L}{N_s} & (ij) \text{ diagonal bond}\,, \\ \frac{SC(\varepsilon)L}{2N_s}(2+\eta_i\eta_j) & (ij)\ \hat{\mathbf{x}} \text{ or } \hat{\mathbf{y}} \text{ bond}\,, \\ 0 & \text{otherwise}\,, \end{cases} \tag{6.45}$$

Note that due to the anisotropy of the checkerboard lattice (i.e., the asymmetry between diagonal and $\hat{\mathbf{x}}$ or $\hat{\mathbf{y}}$ bonds), here Γ_{ij} does not have the expected form (6.15).

Single tetrahedron

To find the leading order quartic energy for a generic state, we consider the three possible bond configurations for a single tetrahedron, which can be viewed as three *polarization axes*:[8, 9] z (where all tetrahedra are oriented as in the (π,π) state), x and y (see Fig. 6.5).[2]

Summing up the contributions, we obtain, for a single z polarized tetrahedron:

$$E^{\boxtimes}_{\text{quart}} = \frac{1}{S^2}\sum_{\langle ij\rangle\in\boxtimes}\eta_i\eta_j\Gamma^2_{ij} \approx C(\varepsilon)^2L^2/N_s^2\,. \tag{6.46}$$

On the other hand, for x or y polarization we find

$$E^{\boxtimes}_{\text{quart}} \approx 2C(\varepsilon)^2L^2/N_s^2\,. \tag{6.47}$$

[2]In Ref. [6] the polarization axis of checkerboard tetrahedra was denoted by a color Potts variable.

Note that in all cases $\sum \eta_i \eta_j \Gamma_{ij}^{(m)} \approx 0$ to leading order, since the divergent modes do not contribute to the harmonic part of E_{MF} in (6.9).

Thus we found that the divergent contribution to the quartic energy is twice as large for x or y polarization as it is for z polarization. We expect an effective Hamiltonian of the simplified form

$$E_{\mathrm{quart}}^{\mathrm{eff}} = N_s[A(S) - B(S)\rho_z]\,, \tag{6.48}$$

with $B(S) \approx A(S)/2$. Therefore the (π, π) state, in which all tetrahedra are z polarized, would be favored over all other zero-flux states, and thus is the *unique* ground state for the checkerboard lattice.

Numerics for full lattice

To prove our theory on the anharmonic selection among harmonic checkerboard ground states, we constructed various such states in the following way: we started from the (π, π) state on a 8×8 system ("checkerboard"), with periodic boundary conditions. To generate a new state, we applied a gaugelike transformation by changing the sign of $\eta_i \eta_j$ of all bonds crossing one or more horizontal lines going through centers of four tetrahedra (see Fig. 6.6). We do this for any subset of the eight possible horizontal lines, generating a total of 2^8 states, 32 of which are unique by lattice symmetry. Note that the construction of states, as well as our calculation, is based on bond-order (see Appendix B), and thus we need not worry about flipping an odd number of lines of this structure. See Ref. [7] for a detailed discussion of gaugelike transformations; for our purpose, it suffices to realize that each state that we generate is a valid classical ground states with zero flux through each plaquette.

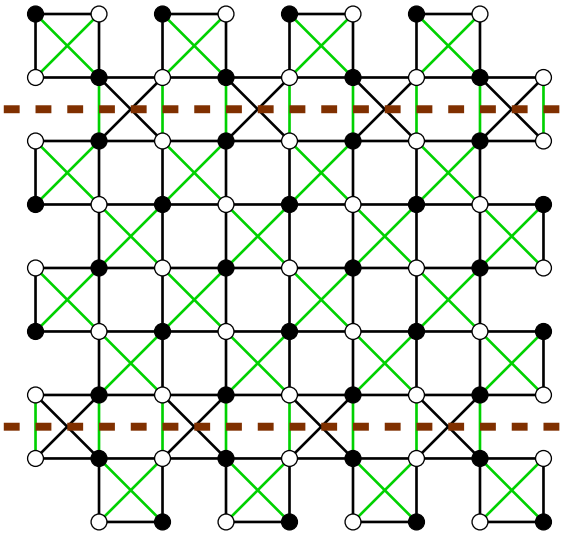

Figure 6.6: A checkerboard lattice harmonic ground state.
This state was constructed by flipping the bonds that cross each of the two dashed horizontal lines.

Whenever we flip a row of bonds, we change the polarization of four tetrahedra from the z direction to the x direction. Based on the arguments of the previous section, we expect that the leading order term in the quartic energy would be proportional to the number of flipped rows.

For each of these states, we calculate the quartic energy for a given value of $\varepsilon = 0.001$, integrating over 41×41 points in the Brillouin zone, equivalent to a system size of 328×328, which is more than required to obtain good accuracy (see Sec. 6.3 for more details about the numerical considerations).

The results are presented in Fig. 6.7, as a function of the fraction of z-polarized tetrahedra ρ_z. As expected we find: (i) the quartic energy is, for the most part, linear in ρ_z. (ii) the energy span is of order $4(\ln \varepsilon)^2/\pi^4$. (iii) the ground state is the uniformly z polarized (π, π) state. (iv) the quartic energy of the (π, π) state is approximately half of the energy of the uniformly x polarized state.

Given the clear differences in $E_{\rm quart}(\varepsilon, S)$ between the various harmonic ground states, we expect that the same ordering would be conserved in the saddle point value $E_{\rm quart}(S)$ upon minimization with respect to ε. Thus we can predict that the large-S checkerboard lattice model would possess long range Neél order at zero temperature. The ground state is the same one found in large-N calculations for the large-S limit. [10, 11] The effective quartic Hamiltonian has the form (6.48) with the coefficients $B(S) \propto (\ln S)^2$ and $A(S) \approx 2B(S)$ to leading order in S. We note that this effective Hamiltonian can be written in a more conventional form, in terms of Ising products

$$E^{\rm eff}_{\rm quart} = N_s A(S) - B(S) \sum_{\langle ij \rangle}{}^{\times} \eta_i \eta_j \,, \tag{6.49}$$

where $\sum^{\times}$ is a sum is over diagonal bonds only.

The result is not very surprising: although we set the Heisenberg couplings to be the same for all bonds in the checkerboard lattice, there is no physical symmetry between the diagonal bonds and the non-diagonal bonds and therefore we should have expected to generate anharmonic terms consistent with the actual lattice symmetry. Thus, unfortunately, this does not provide a guide to lattices where all bonds in a tetrahedron are related by symmetry.

6.3 Effective Hamiltonian for the pyrochlore

We now turn our attention back to the pyrochlore lattice, where, due to the large sizes of the magnetic unit cells of ground state candidates, it would be impossible to do analytic calculations. Our aim here is to calculate the quartic energy for a given arbitrary periodic state, and gather the energies we have calculated to construct an effective Hamiltonian.

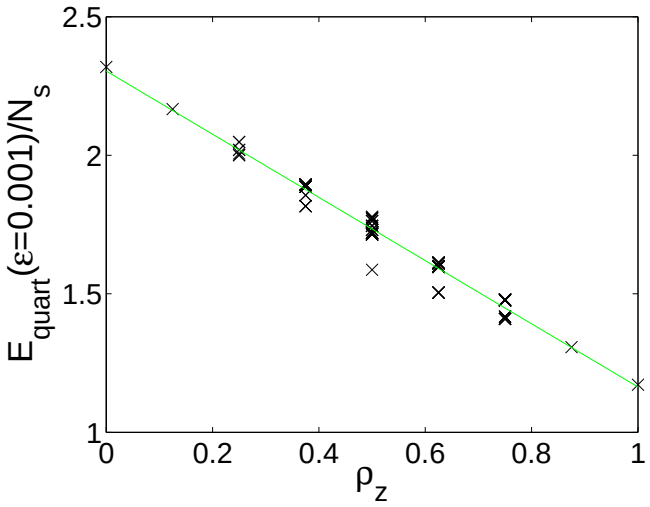

Figure 6.7: Quartic energy for checkerboard lattice harmonic ground states. The energy E_{quart} is shown for $\varepsilon = 0.001$, as a function of the fraction of z polarized tetrahedra, for various checkerboard lattice harmonic ground states.

The numerical calculation is done as follows: for a given collinear classical ground state and a given value of ε we diagonalize the Fourier transform of the variational Hamiltonian (6.6), keeping $\varepsilon + 4\delta$ infinitesimal. We find the bond variable $\Gamma_{ij}(\mathbf{q})$ for each wavevector on a grid of Brillouin zone points, and sum over these points to obtain Γ_{ij} in real space.

In performing the calculation, we find a distinct resemblance to our findings on the checkerboard lattice: There are divergent modes along the x, y, and z axes in the Brillouin zone [7], and these modes dominate the mean field quartic energy (and have no contribution to the harmonic order energy). The variational Hamiltonian's divergence is cut off, along the divergent lines by a term of the order $S/\sqrt{\epsilon}$. The width of the divergence peaks is of order $\sqrt{\varepsilon}$, which means that the grid of wavevectors that we use must become denser in order to capture the effect of the divergent modes, as ε becomes smaller. Thus, we need to sum of the order

of $1/\varepsilon^{3/2}$ points, to obtain good accuracy. This limits the values of S that we can do the calculation for, and we have found no useful numerical tricks to get around it. Nevertheless, we can get results over about two orders of magnitude of S, which can be extrapolated to the $S \to \infty$ limit.

Upon numerical integration, we find, that as in the two-dimensional checkerboard lattice, the divergence of the fluctuations is logarithmic

$$\Gamma_{ij} \propto \ln \varepsilon + \mathcal{O}(\varepsilon)\,. \tag{6.50}$$

This numerical finding is somewhat surprising. We would naïvely expect that the bond variable $\Gamma_{ij}(\mathbf{q})$ would drop, away from the divergent lines, with a functional form (6.35), as in the checkerboard. In that case, two-dimensional integration over $\mathbf{q}_\perp$ would result in a non-singular Γ_{ij}.

It turns out that this expectation is incorrect because the dispersion in the direction perpendicular to the divergence line is strongly anisotropic. For each value of $\mathbf{q}$ along the divergence line, there are two particular independent eigendirections of $\mathbf{q}_\perp$. For example, for a $\mathbf{q} = q_z\hat{\mathbf{z}}$ divergence, corresponding to a linear combination of real-space divergent modes similar to the one shown in Fig. 3.2(b), the eigendirections of $\mathbf{q}_\perp$ are $(1,1,0)$ and $(1,-1,0)$. If we call unit vectors along these eigendirections $\hat{\mathbf{e}}_\mathbf{1}$ and $\hat{\mathbf{e}}_\mathbf{2}$, then we find that $\Gamma_{ij} \propto 1/\sqrt{\varepsilon + (q_\perp \cdot \hat{\mathbf{e}}_\mathbf{1})^2} + 1/\sqrt{\varepsilon + (q_\perp \cdot \hat{\mathbf{e}}_\mathbf{2})^2}$. Integration over $\mathbf{q}_\perp$ results in the logarithmic dependence on ε of (6.50), as in the checkerboard case.

Once we have calculated E_{MF} for many values of ε (for a given collinear state), we can minimize it, for a given S, and find $E_{\mathrm{quart}}(S)$. Our plan of action is to perform this numerical calculation of E_{quart} for a large number of collinear classical ground states and construct an effective Hamiltonian.

6.3.1 Gauge invariant terms

We start by calculating $E_{\rm quart}$ on a large number of classical ground states (not all π-flux states), with unit cells ranging from 4 to 32 sites. We minimize the $E_{\rm MF}$ with respect to ε at each value of S and obtain the energy shown in the inset of Fig. 6.8. We show the energies of 16 states, belonging to five gauge families. Two of these families have uniform $+1$ and -1 products around all hexagons, the zero-flux and π-flux, respectively. We refer to the other three gauge families as the 000π, $0\pi0\pi$, and $00\pi\pi$ plane states, as the hexagon fluxes are arranged in planes such that within each plane the flux is uniform. Due to the exact invariance of the ($\varepsilon = 0$) harmonic energy under the gaugelike transformation, the total energies of states related by such transformations are, as expected, indistinguishable in the inset, since the harmonic term dominates.

In the main part of Fig. 6.8 we show the anharmonic energy $E_{\rm quart}$ for the same states. As in the checkerboard lattice, the dominant part of the quartic energy is quadratic in $\ln S$, and of the order $(\ln S)^2$. However, unlike the checkerboard lattice (compare to Fig. 6.7), we find that the energy *differences* between harmonically degenerate states are one to two orders of magnitude smaller.

We first consider the dominant gauge invariant contribution to the quartic energy. Since the invariants of the gaugelike transformation are products around loops, we search for an effective Hamiltonian in terms of the fluxes Φ_l, similar to the harmonic effective Hamiltonian (4.6).

$$E^{\rm eff}_{\rm quart} = A_0 + A_6(S)\Phi_6 + A_8(S)\Phi_8 + A_{10}(S)\Phi_{10} + \cdots , \tag{6.51}$$

where we find, numerically

$$\begin{aligned} A_0(S) &\approx 0.300 + 0.0130(\ln S)^2\,, \\ A_6(S) &\approx -0.116 - 0.0030(\ln S)^2\,, \\ A_8(S) &\approx -0.022 + 0.0055(\ln S)^2\,, \\ A_{10}(S) &\approx 0.008 - 0.0021(\ln S)^2\,. \end{aligned} \tag{6.52}$$

Note that for large S, the signs of the coefficients A_6, A_8, and A_{10} are opposite to K_6, K_8, and K_{10} in the harmonic Hamiltonian. The differences in signs among the $A_l(S)$ coefficients can explain why some of the lines in Fig. 6.8 appear to be convex and other concave: each family of states is dominated by different flux loop lengths l.

The gauge invariant terms can be heuristically explained in terms of the divergent modes: the quartic energy is large for states that have a large number of divergent modes. As was discussed in Sec. 3.2, the divergent modes are spanned by a set of real-space divergent modes, each with support on a subset of fcc sites S_m. In order for a divergent mode to exist on a given S_m, it turns out that any loop of length $n/2$ (equivalent to diamond lattice or pyrochlore loops of length n), the flux φ_a through the loop, defined in (1.5), must be $(-1)^{n/2}$. This ensures that the mock Ising model within S_m is unfrustrated. Thus, the gauge invariant energy is largest when the product around hexagons is negative and the product around loops of length eight in positive.

In fact, not only the divergent modes, but all ordinary modes of the bare Hamiltonian are gauge invariant (see Appendix E.3). In is only when one considers the details of our (variational) regularization scheme that the degeneracy is broken.

The above discussion of the gauge invariant quartic energy (6.51) is somewhat

moot, inasmuch as it is negligible compared to the harmonic energy (4.6), and it does not break the gauge symmetry. Nevertheless, one can clearly see in Fig. 6.8 that the anharmonic energy within each gauge family is not exactly the same, meaning that there is a gauge-dependent term in the variational anharmonic energy.

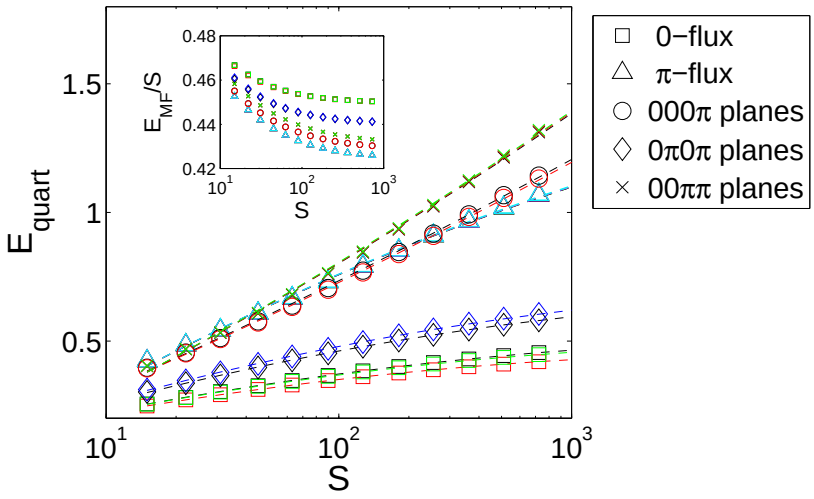

Figure 6.8: Quartic energy $E_{\rm quart}$ for 16 classical collinear ground states. $E_{\rm quart}(S)$ was obtained in the variational calculation. The lines show a numerical quadratic fit in $\ln S$. Each gauge family (represented by 2-6 different states each) is denoted by a different symbol, of which triangles denote the harmonic ground states – the π-flux states. We show six π-flux states, and their energies are virtually indistinguishable to the naked eye. The total energy $E_{\rm MF}$ is shown in the inset.

6.3.2 Gauge dependent terms

Upon close inspection of Fig. 6.8, we see that some of the gauge families have a larger dispersion in their quartic energies than others. Unfortunately, the quartic energy differences among the ground states of the harmonic Hamiltonian –the π-flux states–are much smaller than the gauge-invariant contribution. We attribute

this to the fact that, unlike the checkerboard lattice harmonic ground states or even some pyrochlore gauge families, the set of supports of the divergent modes of the π-flux states possess all of the lattice symmetries. Thus, there is no reason for *any* tetrahedron to prefer a particular polarization axis. We would expect any gauge dependent terms in an effective Hamiltonian to not be as local as those in, say, Eq. (6.48).

In Fig. 6.9, we zoom in on the gauge dependent anharmonic energy, by showing the difference $\Delta E_{\rm quart} \equiv E_{\rm quart} - \overline{E}_{\rm quart}$, where $E_{\rm quart}$ is calculated for 12 π-flux states, and $\overline{E}_{\rm quart}$ is the mean quartic energy of the states shown in the plot.

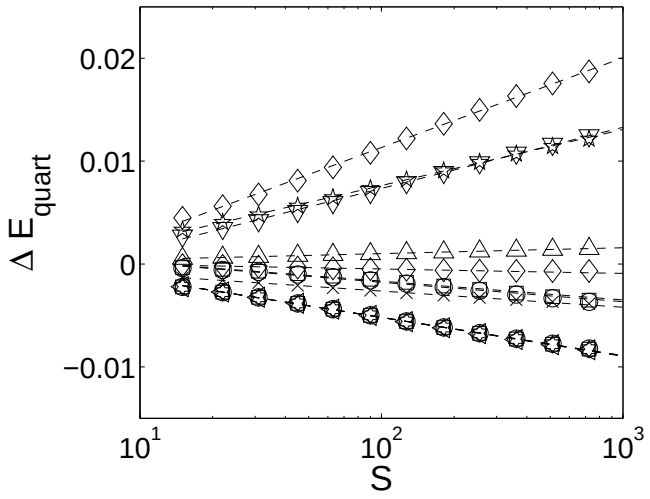

Figure 6.9: Energy difference between $E_{\rm quart}$ of 12 harmonic ground states and the average of their energies $\overline{E}_{\rm quart}$.
By taking differences between energies, we eliminate the (dominant) gauge-invariant term in the anharmonic energy. Each dashed line shows a linear fit in $\ln S$, for one of the states.. Note that there are several overlapping symbols along the bottom line, representing the degenerate states described later in the text (those with the maximum possible value of $\mathcal{P}_6 = N_s/3$).

In order to systematically search for a ground state configuration, we have constructed a large number of harmonic ground states using an algorithm for randomly

generating gaugelike transformations [7]. Within unit cells that we used, of up to 192 sites, we believe that the algorithm performs an *exhaustive* search for harmonic ground states. We observe that each of these energies can be extremely well fitted by a quadratic in $\ln S$. This is consistent with the view that the decoupled quartic energy in Eq. (6.9) is a sum over products $\Gamma_{ij}\Gamma_{ji}$, with Γ_{ij} linear in $\ln S$.

In Fig. 6.10 we show $E_{\rm quart}$ for 50 of the harmonic order ground states at $S = 100$. There are two sources of error in this calculation: The first is the minimization error, represented by the error bars, which is due to the difference in energy between consecutive value of ε that we calculated, i.e. due to the "grid" in ε-space. The second source of error is the grid used in integrating over the Brillouin zone, which is equivalent to a finite (albeit large) system size. This error becomes more significant for large values of S (i.e., smaller values of ε), where the singularity of the divergence lines becomes narrower. The results shown are for 15^3 points in the Brillouin zone, for two different magnetic unit cells: a cubic 128 site unit cell, and a 96 site tetragonal unit cell.

Also shown in the figure is a numerical fit to an effective Hamiltonian of the form

$$\Delta E^{\rm eff}_{\rm quart} = C_6(S)\mathcal{P}_6 + C_8(S)\mathcal{P}_8 + C_{10}(S)\mathcal{P}_{10}\,, \tag{6.53}$$

where $\mathcal{P}_l$ is equal to the number of loops of length l composed solely of satisfied AFM bonds and, for $S = 100$ we obtain

$$\begin{aligned} C_6/N_s &= -0.0621\,, \\ C_8/N_s &= -0.0223\,, \\ C_{10}/N_s &= -0.0046\,. \end{aligned} \tag{6.54}$$

We ignore any constant terms here, as they belong in the gauge-invariant Hamil-

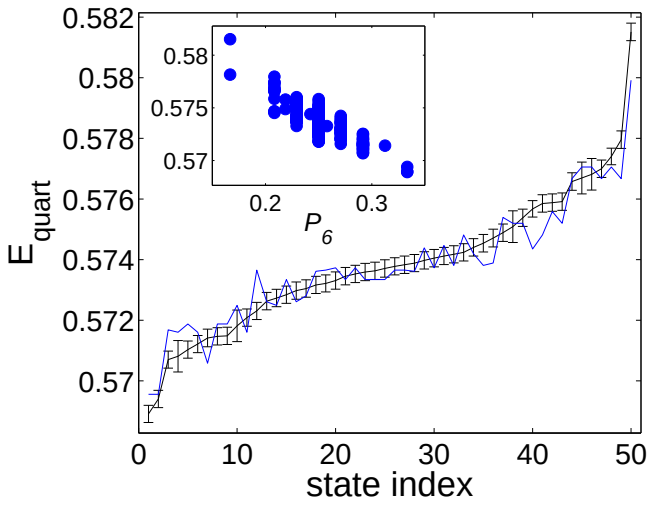

Figure 6.10: $E_{\rm quart}$ for 12 π-flux states at $S = 100$.
Also shown is a numerical fit given by Eq. (6.53). The inset shows the energy as a function of $\mathcal{P}_6$.

tonian (6.51).

While we cannot numerically repeat this calculation over a large range of values of S, in order to find the functional dependence $C_l(S)$ with good accuracy, we can obtain a rough fit by considering the small group of states depicted in Fig. 6.9. For these 12 states we obtain

$$\begin{aligned} C_6(S)/N_s &\approx 0.05 - 0.03 \ln S \,, \\ C_8(S)/N_s &\approx 0.04 - 0.02 \ln S \,, \\ C_{10}(S)/N_s &\approx 0.01 - 0.005 \ln S \,. \end{aligned} \tag{6.55}$$

We remark that we could write the first term of the effective Hamiltonian (6.53) in terms of simple Ising products, using the sum rule (valid for all π-flux states)

$$16\mathcal{P}_6 + S_{3,2} + S_{2,2} = 4 \,, \tag{6.56}$$

where $S_{2,2}$ is a sum over Ising products $\eta_i \eta_j$ for all next-nearest-neighbors (i, j),

such that the distance between i and j is twice the distance between nearest neighbors in the lattice. $S_{3,2}$ is a sum over next-next-nearest neighbors at the same distance.

Although it is hard to say, with no analytical understanding, which parameterization of the effective Hamiltonian is more "fundamental", the form of Eq. (6.53) is appealing, since it depends solely on loop variables. As we have seen in the harmonic theory of Ch. 4, and shall see later in the large-N theory of Ch. 7, it is natural that any non-trivial energy differences among states should be represented in loop variables, since the *local* environments that all spins see are the same.

Although it is a rough fit, with significant error, it is clear (see the inset in Fig. 6.10) that for a large number of states, the leading order contribution to the energy is captured in Eq. (6.53). In particular, the highest energy states are those with $\mathcal{P}_6 = N_s/6$, which can be shown to be the smallest value that $\mathcal{P}_6$ can take (for π-flux states), and the lowest energy states have $\mathcal{P}_6 = N_s/3$ which is the highest possible value of $\mathcal{P}_6$ (see Appendix F for proof of the bounds on $\mathcal{P}_6$).

The value $\mathcal{P}_6 = N_s/3$ is shared by a set of states that are, within the numerical accuracy that we can obtain, degenerate for all values of S. The smallest of these states has a unit cell of 48 spins, and they can be constructed by layering two-dimensional slabs (see Fig. 6.11), where each slab can independently be in any of four orientations. The number of these stacked states is $9 \times 2^{3L/2}$ where L is the linear dimension measured in units of the underlying cubic lattice. In fact, these states share the same values of $\mathcal{P}_l$ for all loop lengths that we calculated ($l \leq 16$). If we believe that the effective Hamiltonian of form (6.53) is valid, it is thus not surprising we cannot distinguish between the energies of these states.

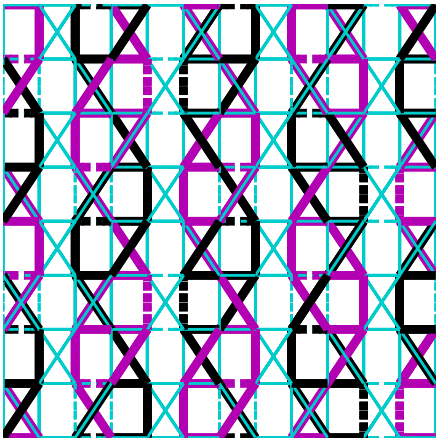

Figure 6.11: {001} projection of the one of the degenerate anharmonic ground state we obtained.
The thick bonds are FM, of which the dark bonds connect two ↑ spins and the light thick bonds connect two ↓ spins. Dashed lines represent bonds that connect between different {001} slices. The magnetic unit cell of this state has 96 spins, and is repeated every two {001} slices. Therefore, in this projection, there may *appear* to be more than two thick bonds per tetrahedron. Other degenerate states possessing $\mathcal{P}_6 = N_s/3$ can be constructed by independently performing a 180° rotation about the x axis and/or translating in the {011} direction the *bond order* of each of the {100} slabs (four configurations for each slab).

6.4 Discussion

We have calculated the anharmonic corrections to the spin-wave energy in the pyrochlore, and found that they break the degeneracy between the various harmonic ground states. We managed to numerically construct an effective Hamiltonian, but we do not have an analytic understanding of its origin, nor does it completely break the degeneracy.

In retrospect, we should not be surprised that the effective Hamiltonian is written in terms of loop variables. After all, in any collinear configuration, the local environment that each spin sees is the same for all sites. If the centers of the simplexes were put on a Bethe lattice rather than a diamond lattice, all collinear configurations would be related by lattice symmetries and would therefore have the same energy (as we find explicitly in Ch. 4 and later in Ch. 7, and in analogy to Ref. [12]). Thus any degeneracy-breaking terms *must* arise from lattice loops, and it is plausible that the effective Hamiltonian could be written explicitly in terms of loops.

Our numerics result in an $\mathcal{O}(L)$ entropy of degenerate ground states. It is worth noting that the anharmonic selection effects in the pyrochlore turn out to be much weaker than in other closely related lattices: the two-dimensional checkerboard and kagomé lattices.

In the checkerboard lattice, which we discussed in Sec. 6.2, many of the details are the same as in the pyrochlore: it is composed of corner sharing tetrahedra, the spin-wave Hamiltonian is the same, and the harmonic ground states are collinear states with uniform fluxes. Nevertheless, because of the anisotropy inherent to the two-dimensional checkerboard, the anharmonic energy breaks the harmonic degeneracy at the lowest order terms, of order $(\ln S)^2$.

In the kagomé lattice, the anharmonic selection is even stronger: first, there are cubic (in spin $\sigma^{x/y}$) anharmonic spin-waves terms. In addition, because of the anisotropy between in-plane and out-of-plane fluctuations about the coplanar states, *all* harmonic zero modes possess divergent fluctuations and therefore the anharmonic energy scales as a power law in S [2, 3, 4].

What are we to make of the anharmonic degeneracy? It could be an exact degeneracy that is related to some hidden symmetry that we have yet to discover or it could be a near degeneracy that would be resolved by adding more and more terms to the effective Hamiltonian. A third option is that the degeneracy is a by-product of our variational approach. Perhaps a more sophisticated self-consistent theory could clearly distinguish between the set of "degenerate" states.

BIBLIOGRAPHY

[1] A. B. Harris, C. Kallin, and A. J. Berlinsky, Phys. Rev. B **45**, 2899 (1992).

[2] A. Chubukov, Phys. Rev. Lett. **69**, 832 (1992).

[3] C. L. Henley and E. P. Chan, J. Magn. Magn. Mater. **140**, 1693 (1995).

[4] E. P. Chan, Ph.D. thesis, Cornell University, 1994.

[5] M. Kvale (unpublished).

[6] O. Tchernyshyov, O. A. Starykh, R. Moessner, and A. G. Abanov, Phys. Rev. B **68**, 144422 (2003).

[7] U. Hizi and C. L. Henley, Phys. Rev. B **73**, 054403 (2006).

[8] S. V. Isakov, K. Gregor, R. Moessner, and S. L. Sondhi, Phys. Rev. Lett. **93**, 167204 (2004).

[9] C. L. Henley, Phys. Rev. B **71**, 014424 (2005).

[10] J.-S. Bernier, C.-H. Chung, Y. B. Kim, and S. Sachdev, Phys. Rev. B **69**, 214427 (2004).

[11] U. Hizi, P. Sharma, and C. L. Henley, Phys. Rev. Lett. **95**, 167203 (2005).

[12] B. Douçot and P. Simon, J. Phys. A: Math. Gen. **31**, 5855 (1998).

Chapter 7

Large-N mean-field theory

In this chapter, we study the large-N Sp(N) mean field theory [1, 2], in the semi-classical limit. This approach has been very successful in other lattices, e.g., the kagomé antiferromagnet.[3] Until now, this approach was generally used only on ordering patterns of high symmetry and small magnetic cells, or by enumerating all saddle-points in a small finite system [3, 4].

Here we develop an effective Hamiltonian approach to this question. Most of the work here has been previously published in Ref. [5]. We first write the mean-field energy, in the limit of $N \to \infty$, in terms of valence bond variables, and then expand it in powers of $1/\kappa$, keeping only the harmonic order $\mathcal{O}(\kappa)$ terms.

The effective Hamiltonian is constructed as an analytical real-space expansion of *loops* made of valence bonds. This allows us to systematically search for a collinear pyrochlore ground state, using Monte Carlo annealing, on quite large system sizes. However, we also find that the pyrochlore ground state does *not* agree with even the lowest-order term in the spin-wave expansion, and therefore cannot give the right answer for the physical ($N = 1$) ground state, in the large-S limit, demonstrating a limitation of the large-N approach for this case.

7.1 Large-N formalism

We begin by discussing the mean-field Hamiltonian derived from the Sp(N) generalization of H. For the (SU(2)) $N = 1$ case we transform to Schwinger boson operators

$$S_i^z = \frac{1}{2}(b_{i\uparrow}^\dagger b_{i\uparrow} - b_{i\downarrow}^\dagger b_{i\downarrow})\,, \quad S_i^+ = b_{i\uparrow}^\dagger b_{i\downarrow}\,, \quad S_i^- = b_{i\downarrow}^\dagger b_{i\uparrow}\,, \tag{7.1}$$

with the spin size fixed at each site by the constraint

$$b_{i\uparrow}^{\dagger} b_{i\uparrow} + b_{i\downarrow}^{\dagger} b_{i\downarrow} = 2S\,. \tag{7.2}$$

The boson operators obey the standard boson commutation relations. It is convenient to rewrite the interaction in terms of valence bonds created by the operator

$$A_{ij}^{\dagger} \equiv b_{i\uparrow}^{\dagger} b_{j\downarrow}^{\dagger} - b_{i\downarrow}^{\dagger} b_{j\uparrow}^{\dagger}\,. \tag{7.3}$$

Thus, the Hamiltonian (1.1) can be written

$$\mathcal{H} = \sum_{ij} \left(-\frac{1}{2} A_{ij}^{\dagger} A_{ij} + \frac{1}{4} S^2 \right)\,. \tag{7.4}$$

An arbitrary singlet state can be written in terms of some arrangement of these bonds with at most $2S$ bonds emanating from any lattice site.

The large-N Hamiltonian is obtained by generalizing the bond operators A_{ij} in the Hamiltonian (7.4) to N flavors

$$A_{ij} = \sum_{m} \left(b_{i\uparrow,m}^{\dagger} b_{j\downarrow,m}^{\dagger} - b_{i\downarrow,m}^{\dagger} b_{j\uparrow,m}^{\dagger} \right)\,, \tag{7.5}$$

where the *flavor* index $m = 1, 2..., N$. Thus we put a large number of bonds on a link. Since the Hamiltonian acting on a state changes at most two bonds per link, the relative change in the number of bonds goes like $1/NS$. In the limit of $N \to \infty$ limit which we consider, the effect of fluctuations is reduced, and we obtain a mean-field theory.

Upon Hubbard-Stratonovich decoupling of (7.4), we obtain the mean-field Hamiltonian

$$H_{\rm MF} = \frac{1}{2} \sum_{\langle ij \rangle} \left[N |Q_{ij}|^2 + \left(A_{ij}^{\dagger} Q_{ij} + H.c. \right) \right] + \sum_{i} \lambda_i \left(b_{i\sigma,m}^{\dagger} b_{i\sigma,m} - N\kappa \right) \tag{7.6}$$

Here the bond variables Q_{ij} satisfy

$$Q_{ij} = \frac{1}{N} \langle A_{ij} \rangle\,. \tag{7.7}$$

The Lagrange multipliers λ_i have been introduced to enforce the constraint on boson number $N\kappa$ at every site i, defining the *generalized spin length*

$$\kappa = 2S\,. \tag{7.8}$$

The Hamiltonian (7.6) can be written in matrix form

$$\begin{aligned} H_{\rm MF} &= \frac{1}{2}\sum_{\langle ij\rangle} N|Q_{ij}|^2 - N\kappa\sum_i \lambda_i & \text{(7.9a)}\\ &+ \sum_m (\mathbf{b}^\dagger_{\uparrow,m}, \mathbf{b}_{\downarrow,m}) \begin{pmatrix} \mathbf{\Lambda} & \mathbf{Q} \\ \mathbf{Q}^\dagger & \mathbf{\Lambda} \end{pmatrix} \begin{pmatrix} \mathbf{b}_{\uparrow,m} \\ \mathbf{b}^\dagger_{\downarrow,m} \end{pmatrix} - N\sum_i \lambda_i\,, & \text{(7.9b)} \end{aligned}$$

where $\mathbf{Q}$ is the (antihermitian) $N_s \times N_s$ matrix whose elements are $J_{ij}Q_{ij}$, $\mathbf{b}_{\sigma,m}$ is the vector whose N_s elements are $\{b_{i\sigma,m}\}$, and $\mathbf{\Lambda}$ is the diagonal matrix with elements $\delta_{ij}\lambda_i$. We are interested in large enough values of κ to condense a flavor mode of the itinerant bosons, $\langle b_{i\sigma,m}\rangle = \sqrt{N}\delta_{1,m}x_{i\sigma}$. This is equivalent to an assumption of long-range order, breaking the Sp(N) symmetry. The mean-field ground state energy (per flavor) is obtained by diagonalizing (7.9b) by a canonical Bogoliubov transformation:

$$\begin{aligned} \frac{E_{\rm MF}}{N} &= \frac{1}{2}\sum_{\langle ij\rangle} \left[|Q_{ij}|^2 + (x_{i\uparrow}x_{j\downarrow} - x_{i\downarrow}x_{j\uparrow})\,Q^*_{ij} + c.c.\right] \\ &+ \sum_i \lambda_i \left(x^*_{i\uparrow}x_{i\uparrow} + x^*_{i\downarrow}x_{i\downarrow} - \kappa\right) & \text{(7.10a)}\\ &+ {\rm Tr}\left(\sqrt{\mathbf{\Lambda}^2 - \mathbf{Q}^\dagger\mathbf{Q}} - \mathbf{\Lambda}\right), & \text{(7.10b)} \end{aligned}$$

Here (7.10b) is the zero-point energy contribution of the bosons. The exact mean-field ground state is obtained by a constrained minimization of the above expression. It can be systematically approached as an expansion in powers of $1/\kappa$. The leading contribution to the energy (of order κ^2) is Eq. (7.10a), whose minimization simply relates the valence bonds to the condensate configuration in the classical

ground states of the Heisenberg Hamiltonian H with spin size $\kappa/2$. We will denote this configuration of bond variables with a superscript c: $\{Q^c_{ij}\}$, satisfying $Q^c_{ij} = x_{i\uparrow}x_{j\downarrow} + x_{i\downarrow}x_{j\uparrow}$. The quantum correction (of order κ) is provided by terms in (7.10b) for these bond configurations.

In the most general case, where the spin at site i is characterized by classical spherical angle (θ_i, ϕ_i), the condensed boson component can be written

$$x_{i\uparrow} = \sqrt{\kappa} e^{i(\Phi_i + \phi_i/2)} \cos\theta_i/2\,, \qquad x_{i\downarrow} = \sqrt{\kappa} e^{i(\Phi_i - \phi_i/2)} \sin\theta_i/2\,, \tag{7.11}$$

where Φ_i is an *arbitrary* U(1) gauge field. Therefore, at the saddle-point

$$\begin{aligned} Q^c_{ij} &= -x_{i\uparrow}x_{j\downarrow} + x_{i\downarrow}x_{j\uparrow} \\ &= \kappa e^{i(\Phi_i + \Phi_j)} \left(\cos\frac{\phi_i - \phi_j}{2} \sin\frac{\theta_i - \theta_j}{2} - i \sin\frac{\phi_i - \phi_j}{2} \sin\frac{\theta_i + \theta_j}{2} \right) . \end{aligned} \tag{7.12}$$

Also, at the saddle point, $\lambda_i = \lambda^c = 4\kappa$ for all pyrochlore lattice classical ground states. Note that for these Q^c_{ij} the classical contribution to the energy (7.9a) is, for all classical ground state configurations, $E_{\rm cl} = -N_s\kappa^2/4$, in agreement with Eq. (2.6) [using Eq. (7.8)].

On general grounds we expect, as for the spin-waves in Sec. 4.4, that quantum corrections would select *collinear* ground states from the classical ground state manifold [6, 7]. We therefore restrict our attention to such states, in which each spin can be denoted by an Ising variable $\eta_i \in \{\pm 1\}$. Once we find an effective Hamiltonian in terms of loop variables, we shall see, in Sec. 7.4, that the *same* effective Hamiltonian also applies for non-collinear spins, with a generalization of the variables. This will allow us to compare the energies of *any* set of classical ground states, collinear or non-collinear. Collinearity implies that, up to an arbitrary gauge choice of $\{\Phi_i\}$

$$Q^c_{ij} = \kappa(\eta_i - \eta_j)/2\,, \tag{7.13}$$

and thus the bond variables are $\pm\kappa$ for every satisfied, AFM bond, and zero otherwise.

7.2 Loop expansion and effective Hamiltonian

Next, we recast the first quantum correction to the mean field energy, Eq. (7.10b), for a given classical ground state, into an effective Hamiltonian form where only some of the degrees of freedom remain [8]. Eq. (7.10b) can formally be Taylor-expanded

$$\frac{E_q}{N} = -\sum_{m=1}^{\infty} \frac{(2m+1)!!}{2^m \lambda^{2m-1} m!} \operatorname{Tr}\left[\left(\mathbf{Q}^\dagger \mathbf{Q}\right)^m\right] \tag{7.14}$$

7.2.1 Expansion for collinear classical states

In the case of collinear classical ground states, from Eq. (7.13), $|Q_{ij}/\kappa| = 1$ for AFM bonds, and zero otherwise, $\operatorname{Tr}\left[(\mathbf{Q}^\dagger\mathbf{Q}/\kappa^2)^m\right]$ is equal to the number of closed paths of length $2m$, composed of AFM bonds. All terms in Eq. (7.14) depend solely on the structure of the network formed by AFM bonds. Since the Ising variables η_i alternate along paths in this network, each nonzero element of $\mathbf{Q}^\dagger\mathbf{Q}$ is κ^2. Note that, whereas the phase of Q_{ij} (and $(\mathbf{Q}^\dagger\mathbf{Q})_{ij}$) depends on the gauge choice in (7.11), all terms appearing in Eq. (7.14) are gauge-invariant.

In any collinear classical ground state, each tetrahedron (with two up spins and two down spins) has four AFM bonds forming a closed loop (see Figs. 7.1a-d). This means that locally, in the AFM network, each site has coordination 4 and belongs to two loops of length 4. Thus many closed paths only contribute state-independent terms to Eq. (7.14). For example, $\operatorname{Tr}\mathbf{Q}^\dagger\mathbf{Q} = 4N_s\kappa^2$, for any classical ground state since the only paths of length 2 involve going to and fro on the same bond, and each site has four neighbors which have the opposite spin (see Fig. 7.1a).

Similarly $\mathrm{Tr}(\mathbf{Q}^\dagger\mathbf{Q})^2 = (16+12+4)N_s\kappa^4$, where the three terms correspond to the paths shown in Figs. 7.1b, 7.1c, 7.1d, respectively. All paths that do not involve loops, (e.g. those in Figs. 7.1a, 7.1b, 7.1c) can be viewed, similarly to the spin-wave case of Sec. 4.1, as paths on a Bethe lattice of coordination 4, and would contribute a constant term to the energy for all collinear classical ground states. The same is true for paths involving any combination of trivial loops and Bethe lattice paths, as in Fig. 7.1d. Here, a "trivial" loop is the loop of length 4 that exists within any tetrahedron.

An important remark is that in this chapter, the meaning of the term "loop" is different than in the spin-wave theory of Chs. 2-6. In the spin-wave discussion, we limited the term to mean "diamond lattice loop". Here, on the other hand, all pyrochlore closed paths are considered "loops".

The lattice that includes trivial loops, and no other loops, can be mapped one-to-one to a *decorated Bethe lattice* (sometimes called a *Husimi cactus*), composed of corner-sharing squares whose centers lie on the sites of a $z = 4$ Bethe lattice (see Fig. 7.2) . The lowest order terms in expansion (7.14) that contribute a state-dependant term in the effective Hamiltonian are for $2m = 6$, since the shortest non-trivial loops are hexagons.

This leads us to parameterize the effective Hamiltonian in terms of the various non-trivial AFM loops.

$$\frac{E_q^{\mathrm{eff}}}{N(\kappa/2)} = \mathcal{K}_0 + \mathcal{K}_6\tilde{\mathcal{P}}_6 + \mathcal{K}_8\tilde{\mathcal{P}}_8 + \mathcal{K}_{10}\tilde{\mathcal{P}}_{10} + \cdots , \tag{7.15}$$

where $\{\mathcal{K}_{2l}\}$ are numerical coefficients, and $\tilde{\mathcal{P}}_{2l}$ is the number of non-trivial AFM loops of length $2l$, per site. Note that $\tilde{\mathcal{P}}_{2l}$ is not equal to $\mathcal{P}_{2l}$ in Ch. 6. This is because the term "loop" used here is more general than in the spin-wave theory, as mentioned before.

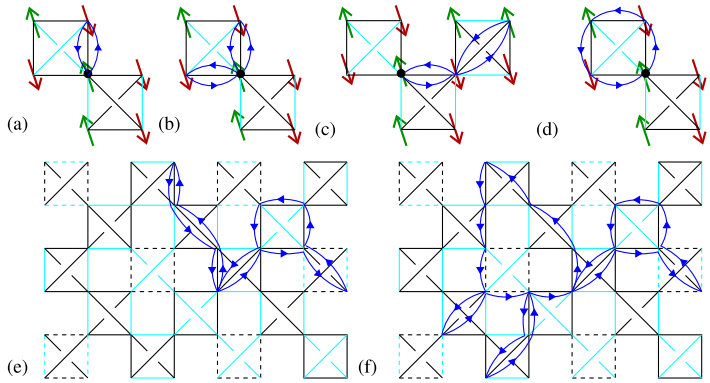

Figure 7.1: Real-space paths counted in calculation.
(a)-(d) Schematic diagram of terms contributing to the constant term in the effective energy, due to $\mathrm{Tr}\,\mathbf{Q}^2$ (a), and $\mathrm{Tr}\,\mathbf{Q}^4$ (b,c,d). These are $\{001\}$ projections, where the crossed squares are projected tetrahedra, and AFM bonds are shown in dark. All paths that do not contain loops, e.g. (a,b,c), can be viewed as paths on a coordination 4 Bethe lattice. (e)-(f): Examples of the two types of paths that we need to count, in order to calculate the effective Hamiltonian coefficients, as shown on a $\{001\}$ slice of the pyrochlore lattice. The dashed lines represent bonds that connect to adjacent slices. (e) A decorated Bethe lattice path of length 14 contributing to $F(14)$ and (f) A path of length 22 containing a loop of length 8, contributing to $G(8, 14)$.

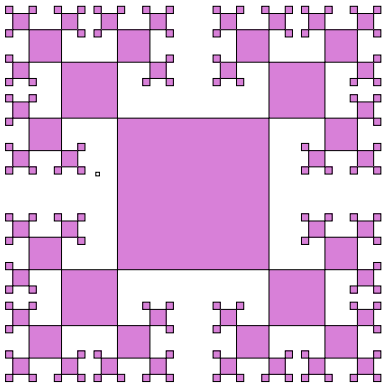

Figure 7.2: Decorated Bethe lattice (Husimi cactus).
The figure shows the topology of 5 "generations" of the lattice. Note that all of the squares are equivalent.

To evaluate the coefficients $\{\mathcal{K}_{2l}\}$, we need to calculate two types of terms: (i) The number $F(2m)$ of closed paths of total length $2m$ on the decorated Bethe lattice (Fig. 7.1e). (ii) The number $G(2l, 2m)$ of closed paths of length $2(m + l)$, involving a particular loop of length $2l$ with decorated Bethe lattice paths emanating from each site along the loop (Fig. 7.1f). [We use these notations in the interest of consistency with Ref. [5], even though $F(2m)$ and $G(2l, 2m)$ are analogous to f_m and f^l_{m+l} of Sec. 4.1.1, respectively.] Calculating these terms is a matter of tedious but tractable combinatorics similar in spirit to the calculations in the spin-wave loop expansion of Sec. 4.1.1 and App. A.

We find, numerically, that the functions $F(2m)$, $G(2l, 2m)$ decay exponentially with m, allowing us to sum them in order to evaluate the coefficients to any accuracy in Eq. (7.15), using

$$\mathcal{K}_0 = \sum_{m=0}^{\infty} F(2m)\,, \qquad \mathcal{K}_{2l} = \sum_{m=0}^{\infty} G(2l, 2m)\,. \tag{7.16}$$

We show the first five coefficients in Tab. 7.1. Thus we have obtained an effective Hamiltonian that is parameterized solely by the number of AFM loops of various sizes. Note that the coefficients decay rapidly $\mathcal{K}_{2l+2}/\mathcal{K}_{2l} \approx 1/10$, which leads us to expect short loops to be the dominant terms in the expansion. This allows us, in principle, to calculate the energy, to any accuracy, for any member of an *infinite* ensemble of classical ground states. This represents a significant improvement over previous calculations that were always limited to small system sizes [3, 4].

7.2.2 Comparison to spin-wave loop expansion

We should note here that despite the similarities between the calculation here and the derivation of the spin-wave effective Hamiltonian in Sec. 4.1, there are some

Table 7.1: Coefficient values for Eq. (7.15).
The values were obtained analytically, and by an independent numerical fit to the energies in Fig. 7.3.

coefficient	analytical	numerically fitted
$\mathcal{K}_0$	-0.59684	-0.59687
$\mathcal{K}_6$	-3.482×10^{-3}	-3.522×10^{-3}
$\mathcal{K}_8$	-3.44×10^{-4}	-3.76×10^{-4}
$\mathcal{K}_{10}$	-3.59×10^{-5}	-4.5×10^{-5}
$\mathcal{K}_{12}$	-3.8×10^{-6}	-5.5×10^{-6}

subtle differences: (i) The coordination-4 lattice Bethe lattice considered in the spin-wave calculation was a mapping from the diamond lattice formed by centers of pyrochlore tetrahedra. Here, the sites on the decorated Bethe lattice (Husimi cactus) correspond to pyrochlore lattice sites and the bonds on the decorated Bethe lattice correspond to AFM pyrochlore bonds. (ii) In the spin-wave calculation, there are no trivial loops, as the starting point is the diamond lattice. Conversely, here the trivial loops *do* contribute to the zero-point energy, and therefore we decorate the Bethe lattice with such loops. (iii) In the spin-wave calculation of Sec. 4.1, each bond contributes $\mu_{\alpha\beta} = \pm 1$ to the product around loops. These products differ between various classical configurations. On the other hand, in the large-N calculation all bonds have identical contributions to the products, but the *number* of loops of various lengths is different for different spin classical ground states. This is because the *connectivity* of the lattice depends on the arrangement of AFM bonds, which depends on the configuration.

7.3 Numerical results

To verify the validity of the effective Hamiltonian (7.15), we calculated the energy for a large number of collinear classical ground states, as well as some harmonic spin-wave ground states, obtained by the same random flipping algorithm used to find states in Sec. 4.2, described in Appendix. C.1. We find that the energies are remarkably well described by E_q^{eff}, even when we cut the expansion (7.15) off at $2l = 8$, as shown in Fig. 7.3. We used the coefficient values of Tab. 7.1, but had to adjust the constant term $\mathcal{K}_0$ *separately* for each choice of cutoff, in order to get a good fit [1]. In practice, this means that the effective Hamiltonian (7.15) is extremely useful for *comparing* energies of various states, even with a small cutoff, but requires many terms in order to accurately determine the energy. An independent 5-parameter numerical fit, to Eq. (7.15), up to $2l = 12$, gives the values shown in the right-hand column of Tab. 7.1.

Now that we have an approximate formula for E_q, for any collinear classical ground state, we can systematically search these states, with large magnetic unit cells, to find a ground state. We conducted Monte Carlo simulations using a Metropolis loop flipping algorithm and the effective energy of Eq. (7.15), for various orthorhombic unit cells of sizes ranging from 128 to 3456 sites, with periodic boundary conditions. The Monte Carlo algorithm, described in Appendix C.3, was adapted from the aforementioned loop-flipping algorithm.

We find a minimum energy of $E_q/(N\kappa/2) = -0.60077N_s$ for a family of *nearly* degenerate states. They are composed of layers, that can each be in one of four

[1] We could get a cutoff-independent constant term $\tilde{K}_0$ if we replaced $\tilde{\mathcal{P}}_{2l}$ by $\tilde{\tilde{P}}_{2l} = \tilde{\mathcal{P}}_{2l} - \langle\tilde{\mathcal{P}}_{2l}\rangle$, where $\langle\tilde{\mathcal{P}}_{2l}\rangle$ is the ensemble average of $\tilde{\mathcal{P}}_{2l}$, and took $\tilde{K}_0 = \mathcal{K}_0 + \sum \mathcal{K}_{2l}\langle\tilde{\mathcal{P}}_{2l}\rangle$.

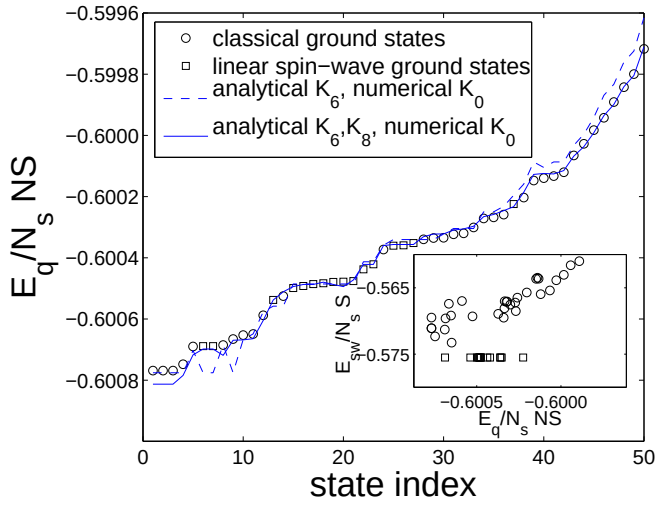

Figure 7.3: Energies E_q of 50 sample classical ground states.
16 of these are harmonic spin-wave ground states (squares), and the rest are shown with circles. We also show the effective energy $E_q^{\rm eff}$, with $2l \leq 6$ (dashed line) and $2l \leq 8$ (solid line). The constant term $\mathcal{K}_0$ was numerically fitted (see main text). The inset shows the linear spin-wave energy for the same states. Although the spin-wave energy tends to be lower for states with lower E_q, the large-N ground state need not be a spin-wave ground state.

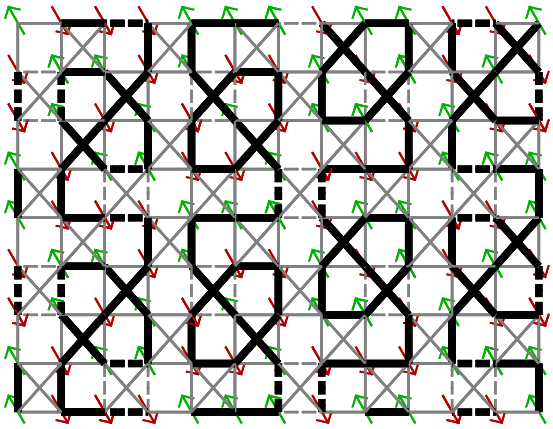

Figure 7.4: The ground state of our large-N theory.
Here we show the state in a $\{001\}$ projection. Light (dark) bonds represent AFM (FM) bonds (unlike in Fig. 7.1). The shown pattern is repeated along x and y directions, as well as in adjacent z slices. This state has a 48 site magnetic unit cell.

arrangements, resulting in $\sim e^{cL}$ states, where L is the system size, and c is a constant. Each of these states has $\tilde{\mathcal{P}}_6 = N_s/3$, which is the maximum possible value of $\tilde{\mathcal{P}}_6$ (see Appendix F; this value is *not* unique to these states), and $\tilde{\mathcal{P}}_8 = 23N_s/6$. Upon closer investigation, however, we find that a *unique ground state* (depicted in Fig. 7.4) is selected. The energy difference to nearby states is of order $10^{-7}N_s$, corresponding to the $2l = 16$ term.

7.4 Non-collinear spins

Although we derived the effective Hamiltonian for collinear states, it turns out that, in fact, the classical tetrahedron zero sum rule implies that Eq. (7.15), with the coefficients in Tab. 7.1, is valid for *any non-collinear* classical ground state, as

well, with the generalized loop variables expressed as sums over non-trivial loops

$$\tilde{\mathcal{P}}_{2l} = \frac{1}{\kappa^{2l}} \sum_{(i_1 \ldots i_{2l})} \mathrm{Re}(Q^{\dagger}_{i_1 i_2} Q_{i_2 i_3} \cdots Q^{\dagger}_{i_{2l-1} i_{2l}} Q_{i_{2l} i_1}) \,. \tag{7.17}$$

Unlike the collinear case, where the elements of $\mathbf{Q}^{\dagger}\mathbf{Q}$ could only take the values 0 or κ^2, and thus each loop would contribute 0 or 1 to the sum (7.17), in the general case, the matrix elements of $\mathbf{Q}^{\dagger}\mathbf{Q}$ are complex.

This is quite a surprising result. Whereas we found the effective Hamiltonian coefficient in the collinear case by simply *counting* closed paths, the general, non-collinear case would be expected to be much harder to address because, many more paths contribute to the energy, and each of the paths carries a different weight. Nevertheless, the tetrahedron sum rules turns out to imply that the sum $\mathrm{Tr}\left[(\mathbf{Q}^{\dagger}\mathbf{Q})^m\right]$, due to paths on a decorated Bethe lattice, gives the same results for all classical ground states. Thus, all of the decorated Bethe lattice calculations that went into the the values of $\{K_{2l}\}$, in Sec. 7.2, are perfectly valid for the non-collinear case as well.

In the general non-collinear case, the loop variables can be written, using (7.17) and (7.12)

$$\tilde{\mathcal{P}}_{2l} = \left(-\frac{1}{2}\right)^{l} \sum_{(i_1 \ldots i_{2l})} \left\{ \prod_{n=1}^{2l} (1 - \hat{\mathbf{n}}_{i_n} \cdot \hat{\mathbf{n}}_{i_{n+1}})^{1/2} \cos\left[\varphi_{i_1 i_2} - \varphi_{i_2 i_3} + \cdots - \varphi_{i_{2l} i_1}\right] \right\} . \tag{7.18}$$

Here $\hat{\mathbf{n}}_i$ is he classical direction of spin i and φ_{ij} is the complex argument of Q_{ij} [see Eq. (7.12)].

While our systematic search for a ground state, in Sec. 7.3, was done only among collinear states, we also calculated the energy for several $\mathbf{q} = \mathbf{0}$ non-collinear classical ground states (i.e. states with a 4-site magnetic unit cell). We find numerically that the energy E_q for such states is always larger than for *any* of the collinear states.

The reason for this can easily be seen by considering Eq. (7.18) for hexagons in a $\mathbf{q} = \mathbf{0}$ state. For any such hexagon $\varphi_{i_1 i_2} = \varphi_{i_4 i_5}$, $\varphi_{i_2 i_3} = \varphi_{i_5 i_6}$, and $\varphi_{i_3 i_4} = \varphi_{i_6 i_1}$. Thus the phases of the various bonds cancel out, resulting in $\tilde{\mathcal{P}}_6 \leq 0$ [9]. In the first order of the effective Hamiltonian (7.15), $\mathbf{q} = \mathbf{0}$ non-collinear states are worse than any collinear state.

This, of course, does not strictly rule out the possibility that a non-collinear state with a larger magnetic unit cell would have lower energy than the collinear states. Unlike the spin-wave case, though, here the effective Hamiltonian (7.15) provides a simple formula to calculate E_q for any candidate non-collinear state, and compare to the collinear ground state.

7.5 Validity of results

As we have seen in Chap. 4, the degeneracy of ground states of the spin-wave quantum Hamiltonian, at the lowest order in $1/S$, is associated with a gaugelike symmetry. This symmetry characterizes the degenerate sub-manifold of collinear spin ground states by the condition (4.12). Since the spin-wave theory is exact in the limit of infinite S, the physical ground state must satisfy Eq. (4.12). The state depicted in Fig. 7.4, however, *does not*. Looking at the inset in Fig. 7.3, we find that states with negative hexagon products tend to have lower large-N energy than other states, since they tend to have more AFM loops, but this is not a strict rule. Thus it would seem that the $N \to \infty$, large-κ ground state cannot be the physical ($N = 1$) large-S ground state.

Nevertheless, if we restrict the large-N calculation to harmonic spin-wave ground states only, we find that the ordering of energies for various states is similar to anharmonic spin-wave results of Ch. 6, and does predict the same ground state. As

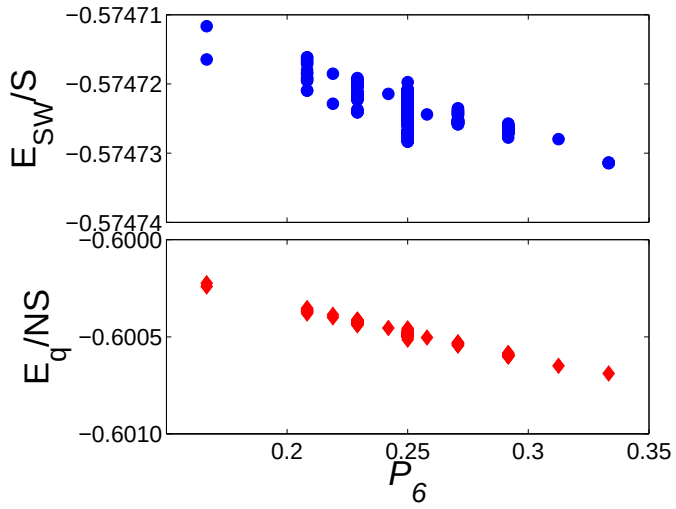

Figure 7.5: Comparison of large-N energies E_q and quartic spin-wave energies. Per-site E_q calculated for various harmonic spin-wave ground states (bottom), compared to the per-site spin-wave energy obtained from an anharmonic calculation for $S = 1500$ (top). In both cases the lowest energy is for a state that maximizes the number of AFM hexagons.

shown in Fig. 7.5, in both cases, the lowest energy among harmonic spin-wave ground state belongs to a state with the most AFM hexagons [2]

The similarities between the large-N theory and the anharmonic spin-wave theory are most vividly seen by comparing the functional forms of the effective Hamiltonians (7.15) and (6.53). Both Hamiltonians favor an abundance of AFM loops of all lengths. The main difference, other than coefficient values, is that the spin-wave loop terms $\mathcal{P}_{2l}$ and the large-N loop terms $\tilde{\mathcal{P}}_{2l}$ are defined on different lattices: the diamond-lattice and the pyrochlore, respectively. Nevertheless, the

[2] At first glance, it may seem strange that the energy E_q/N that we calculate in the mean-field theory, is *lower* than the spin-wave energy, which is, in the limit of large S, exact. Usually, mean-field theories are equivalent to variational Hamiltonians, which *always* produce an upper bound to the exact energy. However, the large-N mean-field theory is *not* variational and therefore it can have lower energy than the exact energy[10].

leading order contribution is from hexagons, for which $\mathcal{P}_6 = \tilde{\mathcal{P}}_6$. This is because all of the (non-trivial) loops of length 6 in the pyrochlore lattice are diamond lattice hexagons.

7.6 Alternative large-N theory

In the previous sections, we developed a large-N mean field theory, which, for collinear spins, has non-zero coupling only along AFM bonds. It would seem that a natural way to generalize the large-N Hamiltonian (7.6) would be to use not only the AFM bond operators A_{ij}, but also FM bond operators [11, 12]. One might think a theory that includes all of the lattice bonds would capture the physics better than one that takes advantage of only a subset of the bonds. We shall see, in the following, that this is not so.

7.6.1 Large-N theory with both AFM and FM bonds

To put the FM bonds back into the theory, we define

$$B_{ij} \equiv b^\dagger_{i\uparrow} b_{j\uparrow} + b^\dagger_{i\downarrow} b_{j\downarrow} \,. \tag{7.19}$$

The Heisenberg Hamiltonian (1.1) can be rewritten

$$\mathcal{H} = \frac{1}{4} \sum_{ij} \left(: B^\dagger_{ij} B_{ij} : - A^\dagger_{ij} A_{ij} \right) \,, \tag{7.20}$$

where $: \cdots :$ denotes normal ordering. Note that obtaining Eq. (7.20), unlike Eq. (7.4), does not require invoking the constraint (7.2). Straightforwardly generalizing B_{ij} to N flavors, as we did for A_{ij} in (7.5), and defining

$$R_{ij} = \frac{1}{N} \langle B_{ij} \rangle \,, \tag{7.21}$$

the mean-field Hamiltonian (7.9) now becomes [13]

$$H_{\rm MF} = \frac{1}{4}\sum_{\langle ij\rangle} N(|Q_{ij}|^2 + |R_{ij}|^2) - \frac{1}{2}N\kappa\sum_i \lambda_i \tag{7.22a}$$

$$+\frac{1}{2}\sum_m (\mathbf{b}^\dagger_{\uparrow,m}, \mathbf{b}_{\downarrow,m}) \begin{pmatrix} \mathbf{\Lambda}+\mathbf{R} & \mathbf{Q} \\ \mathbf{Q}^\dagger & \mathbf{\Lambda}+\mathbf{R}^\dagger \end{pmatrix} \begin{pmatrix} \mathbf{b}_{\uparrow,m} \\ \mathbf{b}^\dagger_{\downarrow,m} \end{pmatrix} - \frac{1}{2}N\sum_i \lambda\,, \tag{7.22b}$$

where $\mathbf{R}$ is the matrix of Hubbard-Stratonovich fields that result from the terms in the Hamiltonian involving B_{ij}. Note that (7.22) possesses neither Sp(N) nor SU(N) invariance.

Repeating the same reasoning as in Sec. 7.1, we assume that one of the flavors of the bosons condenses, as in Eq. (7.11), and find classical configurations Q^c_{ij}, R^c_{ij}, λ^c. The AFM bond variables Q^c_{ij} of (7.12) remain as before. The FM bond variables are easily found to be

$$\begin{aligned} R^c_{ij} &= x^*_{i\uparrow}x_{j\uparrow} + x^*_{i\downarrow}x_{j\downarrow} \\ &= \kappa e^{i(\Phi_j-\Phi_i)}\left(\cos\frac{\phi_i-\phi_j}{2}\cos\frac{\theta_i-\theta_j}{2} - i\sin\frac{\phi_i-\phi_j}{2}\cos\frac{\theta_i+\theta_j}{2}\right) \end{aligned} \tag{7.23}$$

In this case, we find that for all classical ground states $\lambda^c = 2\kappa$.

Limiting ourselves to collinear classical ordering, as in Sec. 7.1, we find that, in the same $\Phi_i = 0$ gauge that we used before

$$R^c_{ij} = \kappa(1+\eta_i\eta_j)/2\,. \tag{7.24}$$

Thus $R^c_{ij} = 1$ for FM bonds and zero otherwise. We can diagonalize block diagonalize the matrix in (7.22b), using the unitary transformation matrix

$$\mathbf{U} = \frac{1}{\sqrt{2}}\begin{pmatrix} \boldsymbol{\eta} & \mathbb{1} \\ \mathbb{1} & -\boldsymbol{\eta} \end{pmatrix} \tag{7.25}$$

And the mean-field Hamiltonian (7.22) becomes

$$H_{\rm MF} = E_{\rm cl} + \sum_m \left[\boldsymbol{\Psi}_m^\dagger \begin{pmatrix} \mathbf{H} & \mathbf{0} \\ \mathbf{0} & \mathbf{H} \end{pmatrix} \boldsymbol{\Psi}_m - \operatorname{Tr} \tilde{\mathbf{H}} \right] \tag{7.26}$$

where

$$\boldsymbol{\Psi}_m = \sqrt{\frac{\kappa}{2}} \mathbf{U} \begin{pmatrix} \mathbf{b}_{\uparrow,m} \\ \mathbf{b}_{\downarrow,m}^\dagger \end{pmatrix} , \tag{7.27}$$

and

$$\mathbf{H} = \frac{1}{2\kappa} \left(\lambda \mathbb{1} + \mathbf{R} + \boldsymbol{\eta} \mathbf{Q} \right) = \frac{1}{2} \mathbf{W}^\dagger \mathbf{W} , \tag{7.28}$$

just like in the harmonic spin-wave Hamiltonian of Eq. (2.16)! Here we used the identities $\boldsymbol{\eta}\mathbf{Q}\boldsymbol{\eta} = -\mathbf{Q}$ and $\boldsymbol{\eta}(\lambda\mathbb{1} + \mathbf{R})\boldsymbol{\eta} = \lambda\mathbb{1} + \mathbf{R}$.

Clearly the zero point energy of this quantum Hamiltonian is equal to N times the harmonic spin-wave zero-point energy, even though we arrived to it from a Schwinger boson theory rather than Holstein-Primakoff bosons. Thus this theory is of no use in breaking the spin-wave degeneracy. However, the "standard" theory of Sec. 7.1 results in a lower energy (see, for example, Fig. 7.5), and thus is a better choice for a large-N saddle point.

7.6.2 Conclusions

The insight that we get from this "experiment", part of which was independently observed by Ref. [9], is that the standard large-N Hamiltonian (7.9) can in fact be obtained from the harmonic spin-wave Hamiltonian (2.9), by setting all of the FM bond matrix couplings to zero. Thus, the large-N Hamiltonian acts on a lattice where all of the frustrating (FM) bonds have been removed, thereby eliminating the branches of zero modes and the harmonic spin-wave degeneracy.

While it is not guaranteed that this prescription would produce the correct ground state (it certainly does *not* in our case), it breaks all degeneracies at the first order in $1/\kappa$, and seems to capture some of the physics involved in ground state selection. On the other hand, when we try to restore the frustrating bonds into the large-N Hamiltonian, we immediately fall back onto the same old Holstein-Primakoff theory.

7.7 Checkerboard and kagomé lattices

The effective Hamiltonian approach that we have outlined in Sec. 7.2 can easily be applied to other lattices. In the checkerboard lattice, the energy is lowest for states that have the most AFM (square) non-trivial plaquettes. Thus, the non-degenerate ground state is clearly the (π,π) state in which *all* plaquettes are AFM [4].

In the kagomé case, all classical ground states are non-collinear. However, if we limit ourselves to coplanar arrangements, we find that Q_{ij} has the same absolute value for *all* of the lattice bonds, but the signs differ depending on the *chirality* of the triangle to which the bond (i, j) belongs. Therefore, the effective Hamiltonian (7.15), with the generalized variables (7.17), prefers classical ground states with negative product of triangle chiralities around all hexagons.

While there are many states for which the product of chiralities around all hexagons are negative, there is only one state among these in which chirality product along all loops of length 10 (the next shortest non-trivial length) is also negative: the $\sqrt{3} \times \sqrt{3}$ state. One can thus conclude that the ground state is the $\sqrt{3} \times \sqrt{3}$ state, as large-N calculations have indeed found [3]. Let us also remark that our method can be generalized to long-range Heisenberg interactions which are relevant in the context of real materials like $Tb_2Ti_2O_7$ [14, 15].

7.8 Small-κ limit

A recent study of the disordered (*small-*κ) limit of the large-N approximation suggests that this for the pyrochlore lattice also has a massive multiplicity of saddle-points [16, 9]. In fact, the authors of these papers suggest that the various saddle-points there is a one-to-one correspondence between the various saddle points and the classical (i.e., large-κ) ground states. In particular, the small-κ saddle points can be parameterized by two angles (θ_i,ϕ_i) at each site, so that the bond variables satisfy Eq. (7.12), up to a change in the normalization $\kappa \to \sqrt{\kappa(\kappa+1)}$. Assuming a uniform saddle-point value λ^c for the field λ_i, the authors of [16] have been able to write a mean-field energy for general κ

$$E_{\mathrm{MF}} = -\frac{N}{2}\frac{\left\{\mathrm{Tr}\left[(|\mathbf{Q}|^2/\mathbf{\Lambda}^2)(\mathbb{1}-|\mathbf{Q}|^2/\mathbf{\Lambda}^2)^{-1/2}\right]\right\}^2}{\mathrm{Tr}\left(|\mathbf{Q}|^2/\mathbf{\Lambda}^2\right)}\,, \tag{7.29}$$

and expand it in powers of κ for several $\mathbf{q}=\mathbf{0}$ ground states (i.e. states with a four-site magnetic unit cell). Naturally, one would like to write an effective Hamiltonian for this problem and use it to systematically search for a ground state.

Starting from the mean field energy (7.29), we were able to write a loop expansion of the form (7.15) and calculate the values of the coefficients K_{2l}, which are, as in the large-κ case, all positive. Thus we were able to reproduce the energies calculated in [16] for some simple (non-collinear) $\mathbf{q}=\mathbf{0}$ states. Furthermore, we can predict that the ground state of the mean-field Hamiltonian would posses the same symmetries as the ground state of our large-κ theory (depicted in Fig. 7.4).

Unfortunately, the validity of our results in this case are questionable, because we have been unable to justify the assumption of uniform λ^c for general ground states. Note that this assumption is certainly reasonable for $\mathbf{q}=\mathbf{0}$ states, studied in [16], since in these states all sites are equivalent.

BIBLIOGRAPHY

[1] N. Read and S. Sachdev, Phys. Rev. Lett. **66**, 1773 (1991).

[2] S. Sachdev and N. Read, Int. J. Mod. Phys. B **5**, 219 (1991).

[3] S. Sachdev, Phys. Rev. B **45**, 12377 (1992).

[4] J.-S. Bernier, C.-H. Chung, Y. B. Kim, and S. Sachdev, Phys. Rev. B **69**, 214427 (2004).

[5] U. Hizi, P. Sharma, and C. L. Henley, Phys. Rev. Lett. **95**, 167203 (2005).

[6] E. F. Shender, Sov. Phys. JETP **56**, 178 (1982).

[7] C. L. Henley, Phys. Rev. Lett. **62**, 2056 (1989).

[8] C. L. Henley, Can. J. Phys. **79**, 1307 (2001).

[9] O. Tchernyshyov, R. Moessner, and S. L. Sondhi (unpublished).

[10] A. Auerbach, in *Interacting electrons and quantum magnetism* (Springer-Verlag, New York, 1994), Chap. 17.

[11] H. A. Ceccatto, C. J. Gazza, and A. E. Trumper, Phys. Rev. B **47**, R12329 (1993).

[12] L. O. Manuel, A. E. Trumper, C. J. Gazza, and H. A. Ceccatto, Phys. Rev. B **50**, R1313 (1994).

[13] P. Sharma (unpublished).

[14] A. P. Ramirez, Annu. Rev. Mater. Sci. **24**, 453 (1994).

[15] *Frustrated spin Systems*, edited by H. T. Diep (World Scientific, Singapore, 2005).

[16] O. Tchernyshyov, R. Moessner, and S. L. Sondhi, Europhys. Lett. **73**, 278 (2006).

Chapter 8

Conclusions

In this thesis, we have presented three different studies of the same problem: the pyrochlore lattice Heisenberg antiferromagnet, in the large-S limit. In each case our aim was to derive an effective Hamiltonian that allows us to systematically search for a ground state.

First, we considered the linear spin-wave theory [1]. Our main findings were the following:

1. The harmonic spin-wave Hamiltonian is exactly invariant under a gaugelike transformation (Sec. 3.4; this was previously shown in Ref. [2]). In particular, this implies that there is a family of exactly degenerate ground states of this Hamiltonian.

2. We analytically derived an effective Hamiltonian in terms of Ising flux variables (Sec. 4.1). We call the ground states of this effective Hamiltonian the π-flux states.

3. We numerically calculated the harmonic energy for a large set of collinear configurations, and find that the energies agree well with the effective Hamiltonian (Sec. 4.2).

4. We find an upper bound on the residual entropy. This bound scales with the system length as $L\,ln L$ (Sec. 4.3). A lower bound has been found in Ref. [2] to scale as $\mathcal{O}(L)$.

It seems to be well-accepted that the spin-wave theory favors collinear states, whenever they are allowed by the classical constraints [3, 4, 5]. We presented, in Sec. 4.4 some circumstantial evidence to support this notion, finding that the collinear states are local minima in the energy landscape. However, we have not

been able to rigorously prove that there cannot be a non-collinear ground state.

We applied our harmonic spin-wave theory to several other models that can support collinear states (Ch. 5), and in each case found the family of ground states and the scaling of entropy with system size. Among these models are the checkerboard lattice, the "capped kagomé" lattice and the $M = 1$ magnetization plateau of the pyrochlore lattice. The latter has been a subject of several recent studies [6, 7] that have given conflicting results.

The second theory that we presented is the anharmonic spin-wave theory of the pyrochlore (Ch. 6, also in Ref. [8]). We develop a self-consistent theory for the quartic order spin-waves, and calculate the energies for the various harmonic ground states. We numerically derive an effective Hamiltonian in terms of a different set loop variables, and find that there is a family of states that are numerically degenerate to our numerical accuracy, resulting in a residual entropy of order $\mathcal{O}(L)$.

We have not been able to prove (or disprove) that the degeneracy among these states is exact, nor have we been able to present an analytical derivation of the anharmonic effective Hamiltonian. More work would be require to resolve these issues.

The third theory that we presented was the large-N mean-field theory, in the semiclassical limit (Ch. 7, also in Ref. [9]). Here, we derived an effective Hamiltonian analytically, and find that it agree well with the numerical calculation for collinear states. While we focused here, once again, on collinear states, it turns out that the large-N effective Hamiltonian is valid for non-collinear states as well, with an appropriate generalization of the variables.

Using the effective Hamiltonian, we performed a Monte Carlo search for the collinear large-N ground state. We find that the large-N ground state is not one

of the harmonic order spin-wave ground states, and therefore, in the $S \to \infty$ limit, the large-N ground state is unphysical. To our knowledge this is the first direct evidence to refute the validity of the widely used large-N theory.

There is an interesting common thread in all three theories that we developed: The local environment at each site is the same among all collinear classical configurations. Therefore, all non-trivial selection effects *must* result from loops in the lattice and thus the effective Hamiltonian, in any theory that possesses the full lattice symmetry, is necessarily a function of loop variables.

What are the experimental implications of our findings? In a system with large spin length S and a predominant Heisenberg interaction, we would expect collinear states to be favored, and a π-flux state as a ground state. In all of the experimental systems that we are aware of, these expectations, based on the harmonic theory, are not fulfilled. For example, out of the most likely Heisenberg candidates, $Tb_2Ti_2O_7$ seems to be paramagnetic at all observable temperatures [10, 11], $Gd_2Ti_2O_7$ (where dipole interactions play a role) there is a noncollinear ordered state [12], and the spinel $ZnCr_2O_4$ undergoes a phase transition into a state of uncoupled fluctuating clusters [13].

A more likely place to search for ordered collinear states in the pyrochlore, is in the field-induced magnetization plateaus discussed in Ch. 5. Indeed, the spin-3/2 Cr ions in $CdCr_2O_4$ and $HgCr_2O_4$ seem, at an appropriate magnetic field, to form a collinear spin arrangement [14, 6, 15]. However, to our knowledge there have been no published reports on neutron scattering experiments on these material, that might resolve the true spin configuration.

BIBLIOGRAPHY

[1] U. Hizi and C. L. Henley, Phys. Rev. B **73**, 054403 (2006).

[2] C. L. Henley, Phys. Rev. Lett. **96**, 047201 (2006).

[3] E. F. Shender, Sov. Phys. JETP **56**, 178 (1982).

[4] C. L. Henley, J. Appl. Phys. **61**, 3962 (1987).

[5] C. L. Henley, Phys. Rev. Lett. **62**, 2056 (1989).

[6] D. L. Bergman, R. Shindou, G. A. Fiete, and L. Balents, cond-mat/0510202 (unpublished).

[7] S. R. Hassan and R. Moessner, cond-mat/0512594 (unpublished).

[8] U. Hizi and C. L. Henley (unpublished).

[9] U. Hizi, P. Sharma, and C. L. Henley, Phys. Rev. Lett. **95**, 167203 (2005).

[10] S.-W. Han, J. S. Gardner, and C. H. Booth, Phys. Rev. B **69**, 024416 (2004).

[11] M. Enjalran and M. J. P. Gingras, Phys. Rev. B **71**, 174426 (2004).

[12] J. D. M. Champion *et al.*, Phys. Rev. B **64**, R140407 (2001).

[13] S.-H. Lee *et al.*, Nature **418**, 856 (2002).

[14] H. Ueda *et al.*, Phys. Rev. Lett. **94**, 047202 (2005).

[15] K. Penc, N. Shannon, and H. Shiba, Phys. Rev. Lett. **93**, 197203 (2004).

Appendix A

calculating Bethe lattice coefficients

In this appendix, we give some of the details that go into the loop expansions for the harmonic spin-waves of Sec. 4.1. In particular, Sec. A.1 corresponds to Sec. 4.1.1 and Sec. A.2 corresponds to Sec. 4.1.3. An analogous loop expansion of the large-N calculation is described in Ch. 7.

A.1 Bethe lattice paths

Consider a Bethe lattice of coordination z, and N_B sites. We shall assume that N_B is infinite so that the translational symmetry of the lattice is conserved. Furthermore, we shall ignore any boundary effects because, in the end, our aim is to map every path on the Bethe lattice to paths on an infinite diamond lattice, where boundary effects play no role. We would like to find the number of paths of length k that start and end at a particular site. Since all sites are equivalent, the total number of paths would just be N_B times this quantity.

Define the following values:

- f_k: The number of paths of length $2k$ starting and ending at a particular site α.
- g_k: Same as f_k, but counting only paths that do not return to the origin until the last step.
- $\tilde{f}_k$: Same as f_k, but the origin α only has $z-1$ nearest neighbors.
- $\tilde{g}_k$: Same as g_k, but the origin α only has $z-1$ nearest neighbors.

The number f_k can be calculated from $\{g_i : i \leq k\}$. E.g.

$$f_3 = g_3 + 2g_1g_2 + g_1^3 \,. \tag{A.1}$$

One way of calculating the coefficients of these expansions in by means of generating functions

$$\mathcal{G} = \sum_{k=1} g_k x^k \,, \qquad \mathcal{F} = 1 + \mathcal{G} + \mathcal{G}^2 + \cdots = \frac{1}{1-\mathcal{G}} \,, \tag{A.2}$$

on the other hand

$$\mathcal{F} = \sum_{k} f_k x^k \,, \qquad f_k = \frac{1}{k!} \left. \frac{\partial^k \mathcal{F}}{\partial x^k} \right|_{x=0} \,. \tag{A.3}$$

$\tilde{f}_k$ can be calculated from $\{\tilde{g}_i : i \leq k\}$ in an identical fashion.

$$\tilde{\mathcal{G}} = \sum_{k=1} \tilde{g}_k x^k \,, \qquad \tilde{\mathcal{F}} = \sum_{k=1} \tilde{f}_k x^k = \frac{1}{1-\tilde{\mathcal{G}}} \,, \tag{A.4}$$

The coefficients g_k, $\tilde{g}_k$, and $\tilde{f}_k$ satisfy the following relations:

$$\tilde{f}_0 = 1 \,, \tag{A.5}$$

$$g_k = z\tilde{f}_{k-1} \qquad \Rightarrow \qquad \mathcal{G} = zx\tilde{\mathcal{F}} \,, \tag{A.6}$$

$$\tilde{g}_k = (z-1)\tilde{f}_{k-1} \qquad \Rightarrow \qquad \tilde{\mathcal{G}} = (z-1)x\tilde{\mathcal{F}} \,. \tag{A.7}$$

Using (A.4) and (A.7) we can solve for $\tilde{\mathcal{F}}$ and obtain

$$\tilde{\mathcal{F}}(t) = \frac{1-\sqrt{1-2t}}{t} \,, \tag{A.8}$$

where we defined a new variable $t = 2x(z-1)$. From (A.6) we obtain

$$\mathcal{G}(t) = \frac{z}{2(z-1)} \left(1 - \sqrt{1-2t}\right) \,, \tag{A.9}$$

from which we can derive g_k

$$g_k = \frac{[2(z-1)]^k}{k!} \left. \frac{\partial^k \mathcal{G}}{\partial t^k} \right|_{x=0} = \frac{(2k-3)!!}{k!} z[2(z-1)]^{k-1} \,. \tag{A.10}$$

The quantity that we actually want to calculate is f_k. Its generating function is

$$\mathcal{F}(t) = \frac{2(z-1)}{z[1+\sqrt{1-2t}]-2}\,. \tag{A.11}$$

While f_k can be easily calculated from (A.10), by summing over products of g_k as in (A.1), it turns out that a close form expression for f_k has been found previously in Ref. [1]

$$f_k = \sum_{r=0}^{k} \left[\begin{pmatrix} 2k \\ r \end{pmatrix} - \begin{pmatrix} 2k \\ r-1 \end{pmatrix} \right] (z-1)^r\,. \tag{A.12}$$

Once $\{f_k\}$ have been found, we calculate the Bethe lattice harmonic energy by the expansion Eq. (4.4) (where the Bethe lattice takes the place of the N_B-site simplex lattice)

$$E_{\rm harm}(\text{Bethe}) = S\sqrt{A}\sum_{n=0} C_n \sum_{k=0}^{n} \frac{(-4)^{n-k}}{A^k} \begin{pmatrix} n \\ k \end{pmatrix} f_k N_B - SN_s\,, \tag{A.13}$$

or similarly for a non-zero magnetization plateau using the expansion Eq. (5.6). $E_{\rm harm}(\text{Bethe})$ is our approximation for the constant term E_0 in the energy.

A.2 Calculating loop coefficients

Here we provide the details of our calculation the coefficient K_{2l} in the effective Hamiltonian (4.6). Consider the terms in the expansion (4.4) that involve loops of length $2l$ and no other loops. In the Bethe lattice approximation, we assume that all of the paths involving a loop, can be viewed as decorated loops, i.e., a loop with self-retracing paths (each equivalent to a Bethe lattice path) emanating from each site. This means that within our approximation, all loops of length $2l$ are equivalent, and therefore, for any k, $\mathrm{Tr}\,\boldsymbol{\mu}^{2k}$ in the expansion is equal to the flux variable Φ_{2l} multiplied by f_k^l, the number of decorated paths of length $2k$

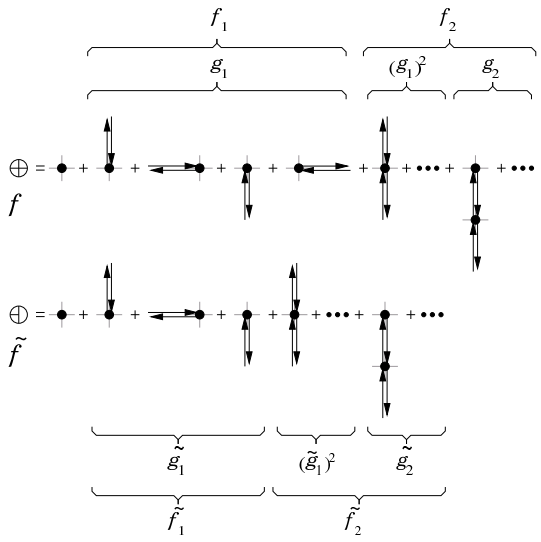

Figure A.1: Diagrammatic representation of the terms in f_k and $\tilde{f}_k$. The difference between the two terms is that whereas f_k is computed on a coordination z Bethe lattice, in $\tilde{f}_k$ the origin has only $z-1$ neighbors, and all other sites have z neighbors.

involving a particular loop of length $2l$. The effective Hamiltonian (4.6) coefficient can therefore be written

$$K_{2l} = S\sqrt{A}\sum_{n=0} C_n \sum_{k=0}^{n} \frac{(-4)^{n-k}}{A^k} \begin{pmatrix} n \\ k \end{pmatrix} f_k^l \,. \tag{A.14}$$

In the case of a large magnetic field of Sec. 5.1, Eq. (A.14) would be replaced by the appropriate expression from the expansion (5.6):

$$K_{2l}(M) = S\sqrt{A}\sum_{n=0}^{\infty} \frac{C_n}{A^n} \sum_{k=0}^{n} \sum_{j=0}^{n-k} \begin{pmatrix} n \\ k\, j \end{pmatrix} \times (M^2 - 4A)^{n-k-j}(-2M)^j f_k^l \,. \tag{A.15}$$

We want to count the number of paths of length $2k$ involving a particular simple loop of length $2l$, and no other loops, such that each site along the loop may be an origin of a self-retracing path (diagrammatically shown in Fig, A.2). As explained in Sec. 4.1.3, in order to avoid double counting, we must consider trees whose

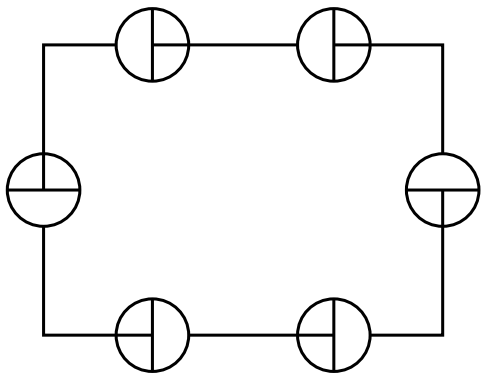

Figure A.2: Diagrammatic representation of the paths included in K_6. Each node along the loop is "dressed" by a Bethe lattice factor, $\tilde{f}k$, as shown in Fig. A.1.

origin has only $z-1$ nearest neighbors. Fortunately, we have already calculated such terms in Sec. A.1, i.e. the terms $\tilde{f}_i$.

All we have to do is to find all of the ways of distributing $k-l$ steps that are not part of the loop, among $2l$ sites, and take the product of $\tilde{f}$ for each of those. In more concrete terms, for a given k, the number of possible paths involving a particular loop of length $2l$ is

$$f_k^l \equiv 4k(k-l)! \sum_{n=1}^{2l} \left(\begin{array}{c} 2l \\ n \end{array} \right) \sum_{\sum i_j = k-l} \frac{\tilde{f}_{i_1}}{i_1!} \frac{\tilde{f}_{i_2}}{i_2!} \cdots \frac{\tilde{f}_{i_n}}{i_n!} \,. \tag{A.16}$$

Here, the factorial factors count the ways of of distributing $k-l$ steps into n Bethe-lattice paths. We have multiplied the sum by $4k$ because we can start anywhere along the path and go in any of two directions. Plugging the results into Eq. (A.14) (or (A.15)), we obtain the effective Hamiltonian coefficients.

BIBLIOGRAPHY

[1] M. Eckstein, M. Kollar, K. Byczuk, and D. Volhardt, Phys. Rev. B **71**, 235119 (2005).

Appendix B

Bond-order calculations

B.1 Collinear spins

The size of a unit-cell used in diagonalization can often be reduced by utilizing the *bond order*. Consider, for example the (π-flux) state shown in Fig. B.1. This state has a tetragonal magnetic unit cell of 32 spins, denoted by the large dashed square. However, it is apparent that the bond order has a smaller, cubic, unit cell of 16 spins. It would certainly be desirable to take advantage of the higher symmetry and smaller unit cell of the bond order. However, in the collinear spin-wave theory that we outlined in Ch. 2, the particular classical spin configuration comes into play via the spin directions η_i. Here we demonstrate how the diagonalization, to find the frequencies $\{\omega_m\}$ and the fluctuations $\{G_{ij}\}$, could be done differently utilizing the bond order.

We would like to change the formalism so that $\{\boldsymbol{\eta}_i\}$ variables would only appear in bond pairs $\eta_{ij} \equiv \eta_i \eta_j$. To do so, we go back to the spin deviation operators $\boldsymbol{\sigma}^{\tilde{x}}$ and $\boldsymbol{\sigma}^{\tilde{y}}$ defined in Eq. (2.7). In the case of collinear spins, the Hamiltonian (2.9) is block diagonal,

$$\mathcal{H}_{\text{harm}} = \vec{\boldsymbol{\sigma}}^{\dagger} \begin{pmatrix} \mathbf{H}^{\tilde{x}} & \mathbf{0} \\ \mathbf{0} & \mathbf{H}^{\tilde{y}} \end{pmatrix} \vec{\boldsymbol{\sigma}} - \frac{S}{2} \, \text{Tr} \left(\mathbf{H}^{\tilde{x}} + \mathbf{H}^{\tilde{y}} \right), \tag{B.1}$$

where $\mathbf{H}^{\tilde{x}} \equiv \boldsymbol{\eta} \mathbf{H} \boldsymbol{\eta}$, and $\mathbf{H}^{\tilde{y}} \equiv \mathbf{H}$, with $\mathbf{H}$ defined in (2.16). Notice that, with the commutation relations (2.8), the spin configuration enters the Hamiltonian only through $\mathbf{H}^{\tilde{x}}$, whose elements are

$$\mathbf{H}^{\tilde{x}}_{ij} = \eta_{ij} \mathbf{H}_{ij} \, . \tag{B.2}$$

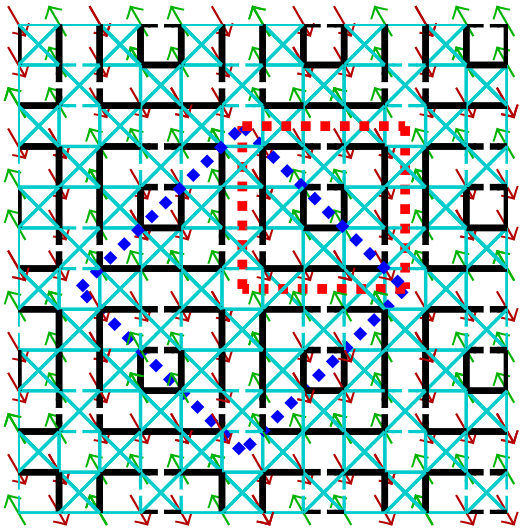

Figure B.1: Bond order unit cell.
Example of reduction of the magnetic unit cell size, by exploiting the bond order. The 32 spin site-order unit cell and the 16 spin bond-order unit cell are shown by the thick dashed lines. We show a {001} slice of the pyrochlore, with dashed bonds connecting to adjacent slices. FM (AFM) bonds are denoted by dark (light) colored lines. In this state, adjacent slice have the same ordering, so that the FM lines spiral in the {001} direction.

Thus, the problem is manifestly defined in terms of bond variables. To diagonalize it, we can repeat the procedure outlined in Ch. 2, taking care not to decompose the bond variable $\eta_{ij} = \eta_i \eta_j$.

To find the spin-wave modes $\tilde{\mathbf{v}}_m$ and their frequencies, we find the eigenmodes of the matrix $\mathbf{H}^{\tilde{y}}\mathbf{H}^{x}x$. The corresponding eigenvalues are λ_m^2. The orthogonality relation that these modes satisfy [analogous to Eq. (2.20)] is

$$(\tilde{\mathbf{v}}_m, \mathbf{H}^{\tilde{x}}\tilde{\mathbf{v}}_n) = \frac{1}{\lambda_m}\tilde{\mathbf{v}}_m^{\dagger}\mathbf{H}\tilde{\mathbf{v}}_n = \tilde{c}_m \delta_{m,n}\,. \tag{B.3}$$

Note with these definitions, even if the site order unit cell is the same as the bond order unit cell, $\tilde{\mathbf{v}}_m$ and $\tilde{c}_m$ are different from $\mathbf{v}_m$ and c_m defined in Ch. 2. The frequency associated with each spin-wave mode is still $\omega_m = 2S|\lambda_m|$. It is easy to obtain, that given these definitions the fluctuations are

$$\langle \boldsymbol{\sigma}^{\tilde{x}} (\boldsymbol{\sigma}^{\tilde{x}})^{\dagger} \rangle = \sum_m \frac{S|\lambda_m|}{2|\tilde{c}_m|} \mathbf{v}_m \mathbf{v}_m^{\dagger}\,, \tag{B.4}$$

where both sides of the equation are $N_s \times N_s$ matrices. The two-point correlation is

$$G_{ij} = \langle \sigma_i^{\tilde{y}} \sigma_j^{\tilde{y}} \rangle = \eta_{ij} \langle \sigma_i^{\tilde{x}} \sigma_j^{\tilde{x}} \rangle\,. \tag{B.5}$$

Thus, we can diagonalize the Hamiltonian and calculate the fluctuations using the bond variables η_{ij} only.

B.2 coplanar spins

In fact, the procedure that we outlined above for bond variables in the collinear case allows us to straightforwardly calculate the harmonic dispersion and fluctuations of any *coplanar* classical ground states.

Consider a coplanar classical ground states, parameterized by angles $\{\theta_i\}$ ($\phi_i = 0$). The harmonic spin-wave Hamiltonian (2.9) becomes block diagonal and can

be written in the form (B.1), with $\mathbf{H}^{\tilde{y}} = \mathbf{H}$, as before, and $\mathbf{H}$ satisfying Eq. (B.2), but the bond variables are no longer Ising variables but rather

$$\eta_{ij} \equiv \cos(\theta_i - \theta_j)\,, \tag{B.6}$$

where $\{\theta_i\}$ are the in-plane spin direction angles. With this substitution, the *entire derivation of Sec. B.1 follows automatically.*

Note that, for the kagomé lattice (or any other bisimplex lattice composed of triangles) the classical constraint (1.3) implies that in all coplanar classical ground states $\theta_i - \theta_j = \pm 120^\circ$ for nearest neighbors, and, from Eq. (B.6), $\eta_{ij} = -1/2$ for *all* coplanar states, and thus all coplanar states are exactly degenerate.

We remark that once we consider non-coplanar states, there is no way to write the spin-wave Hamiltonian in a block diagonal form, and there is no simple way to generalize the procedure described here.

Appendix C

State generation algorithms

In this appendix, we provide the details of the algorithms that we use to automatically generate classical ground states as well as harmonic spin-wave ground state. We also discuss the Monte Carlo algorithm used in Sec. 7.3. All of these algorithms were implemented in the C programming language, and compiled under Linux using the GNU C compiler. The computer programs are a straightforward application of the algorithms described below. They do not employ any fancy programming tricks to reduce memory consumption or running time. As it turns out, this has proven to be sufficient to our purposes.

C.1 Collinear classical ground state generation

The algorithm described here was employed for generating the large number of classical ground states used in Sec. 4.2 and Sec. 7.3. The computer program is called *state_gen.c*. As described in Ch. 2, classical ground states can be generated from other classical ground states by flipping *loops* of spins with alternating directions. Thus the algorithm is based on choosing a random site, and then finding a loop of alternating spins. This is done by moving along a path, randomly choosing a direction (of alternating spin) in each step, until the path intersects itself. Once a loop is closed, we flip the spins along the loop to find a new state. This is done many times to generate new states.

We start by defining an orthorhombic system of dimensions L_x, L_y, L_z, with periodic boundary conditions. The length scale here is such that the lattice constant of the underlying cubic lattice is 2. Thus, in any {001} pyrochlore slice,

there is a unique tetrahedron in for any integer pair (L_x, L_y). We break the lattice into disjoint (even) tetrahedra and we label each even tetrahedron by indices $0 \leq x \leq L_x$, $0 \leq y \leq L_y$, $0 \leq z \leq L_z/2$. The index z only goes to $L_z/2$ so that each integer pair x, y, z would correspond to a valid fcc site, even though the physical z-axis coordinate depends on the parity of $x + y$. The actual tetrahedron coordinate is

$$\mathbf{r} = \left(x, y, 2z + \frac{1 - (-1)^{x+y}}{2} \right) . \tag{C.1}$$

The anisotropy in the indexing in the (x, y) and z directions is necessary to store data for the pyrochlore lattice in a matrix, while maintaining orthorhombic boundary conditions. The states are stored in a *state* matrix of size $L_x \times L_y \times L_z/2 \times 4$. The first three indices in the matrix refer to (x, y, z) and the last index is the sublattice index, taking values 0 to 3.

Since we only store data of (x, y, z) corresponding to even tetrahedra, the odd tetrahedra are only implied, and we have a routine *neighbors* to find, for a given site, its (three) nearest neighbors that belong to different even tetrahedra.

We define a matrix *hex* similar to *state* for the complementary lattice "spins" (described in Ch. 5). We remind the reader that this is the pyrochlore lattice whose sites are the centers of the direct lattice hexagon loops. The Ising spin at a given site in the complementary lattice is the product of the spins along the hexagon whose center is there. Refer to Ch. 5 for further details. The complementary lattice state is useful because it is identical for gauge-equivalent harmonic ground states. Thus, by comparing complementary lattice states, we can ascertain whether two states are in the same gauge family. In order to use this property, we further store a matrix *all_hexs* of all of the distinct complementary lattice states found so far. For diagnostic purposes, we also define the vector *frequencies* in which we store

the number of states we have found in each gauge family that we encountered.

There are three non-trivial functions that we use:

1. The *hex_gen* function generates the complementary lattice state *hex* for a given *state*. We multiply the spin values around each hexagon in *state* and store it in the corresponding location in *hex*.

2. The *same_as* function compares two complementary lattice states to find if they are the same, up to lattice symmetry operations (translations, rotations, axis permutations, mirror planes, inversion of all axes, and global spin flip). This function returns a Boolean number.

3. *random_flip* is the routine that actually generates a new state. We randomly choose an initial site s_1, defined by x, y, z, and sublattice index (between 0 and 3) and flip the corresponding spin (in *state*). Our aim is to now to find a loop of spins in alternating directions and flip all of the spins in it. To do so, we add two spin indices to a list in each step: In each step, call it step number n, we add two more spins to the list: (i) We find the two neighbors of s_{2n-1} that are not within the same (even) tetrahedron, and have the opposite spin as the s_{2n-1}. Randomly choose one of them – s_{2n}– and store it. If we are back to any of the (even) tetrahedra whose sites are already on the list – stop, and flip the loop we found. (ii) Find the two neighbors of s_{2n}, within the same (even) tetrahedron, that have the opposite spin as the s_{2n}. Randomly choose one of them – s_{2n+1}– and store it.

The algorithm that we use for generating classical ground states is shown in Fig. C.1. Essentially, we initialize to a given state (i.e. set the elements of *state* to an allowed combination of ± 1), and in each step run *random_flip*, generate the complementary lattice state for the state we found, and compare (using *same_as*)

to the previously stored complementary lattice states to see if we found a new state. If so, we store the complementary lattice state and print out the η values stored in *state*. We also calculate and print out some properties of the state (both the direct lattice state and the complementary lattice state) that can be later used for numerical fits aimed at finding an effective Hamiltonian. We repeat this procedure, periodically initializing back to the original state.

C.2 Harmonic ground state generation

This algorithm starts from a given harmonic ground state, and generates odd and even gauge transformations on the state. Then, all combinations of the odd and even transformations are applied to find all of the states that are gauge equivalent to the original state. If the original state is a harmonic ground state, we generate other harmonic ground states in this fashion. We have run the program dozens of times with millions of searches in each run and for unit cells of up to approximately 200 sites we always find the same harmonic ground states. This leads us to believe that the search algorithm is exhaustive. This program, called *gauge_gen.c* actually predates *state_gen.c*, which accounts for some of the differences in programming between them.

Since any group of states related by a gaugelike transformation have the same complementary lattice state, there is no point in finding the complementary lattice in this program. We store the transformations that we find in a $L_x \times L_y \times L_z$ matrix of boolean variables (recall that gaugelike transformations amount to flipping entire tetrahedra and not individual spins). We have an array of such matrices (named *gauge*) to store all of the odd and even gaugelike transformations that we find. The current state is stored in the *state* matrix, which is, due to historic reasons slightly

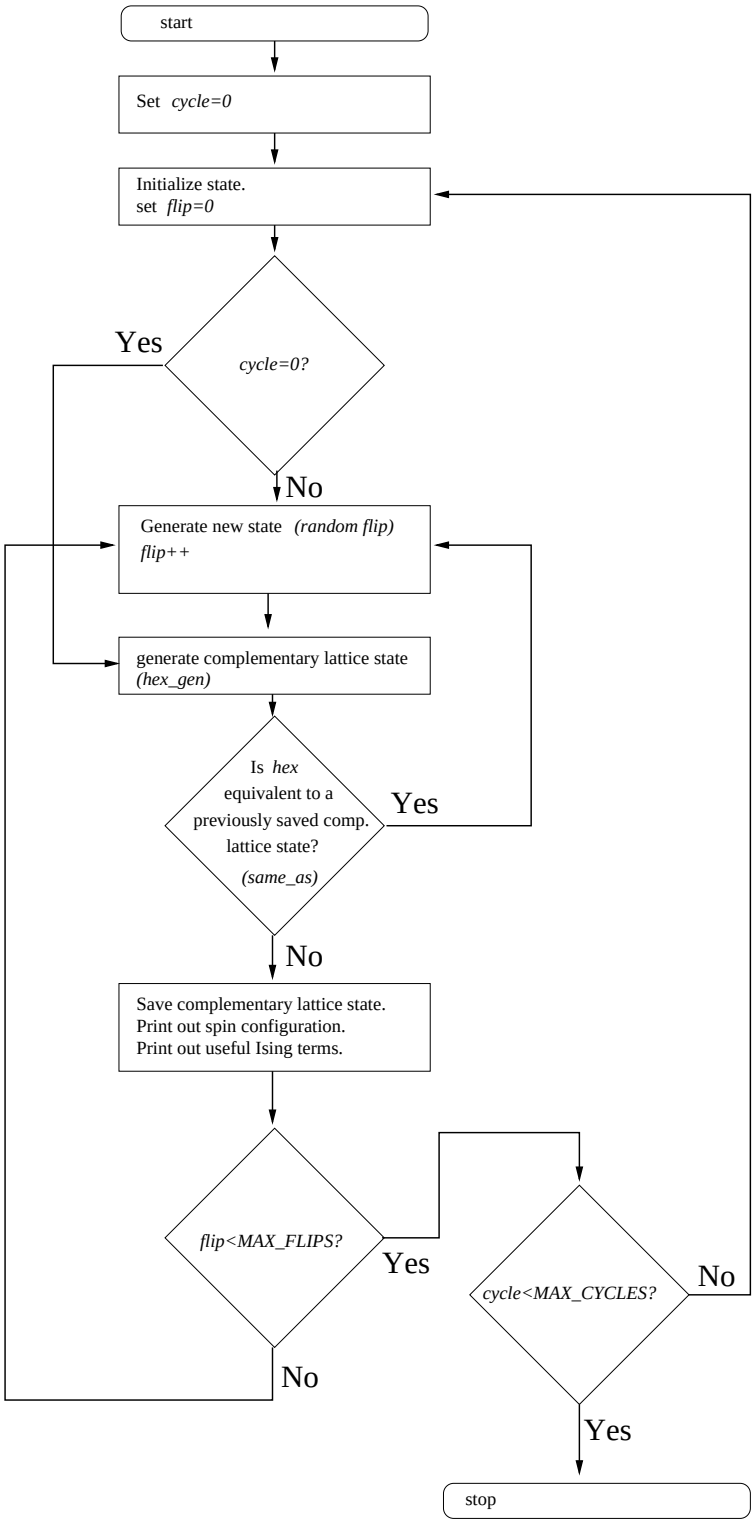

Figure C.1: Flow diagram for *state_gen*.

different than *state* in *state_gen.c*. Here we store both even and odd tetrahedra so that each spin value appears twice in the state matrix. All of the states that we find are in the matrix *all_states*.

The algorithm is composed of three separate parts: (i) generate all even gauge-like transformation for a given states, and save them. The idea here is to flip entire even tetrahedra until a new classical ground state, with no violated odd tetrahedra, remains. As long as only tetrahedra were flipped, we are guaranteed that the new state is related to the old one by a gaugelike transformation. They are saved in a matrix *gauge* of $L_x \times L_y \times L_z/2$ boolean values. (ii) similarly, generate all odd transformations. (iii) apply all combinations of even and odd transformations, and if a distinct state is produced, save and display it.

There are two non-trivial parts to this algorithm:

1. Generating a gauge transformation (*random_gauge* function): suppose that we want to generate an even gauge transformation. We randomly choose an even tetrahedron and flip all of the spins in it. Now we have caused some of the odd tetrahedra to violate the tetrahedron rule. Our plan is to flip more and more even tetrahedra until no more odd tetrahedra are violated. To do so, we check to see if any *odd* tetrahedra now violate the tetrahedron rule, starting from the neighbors of the last (even) tetrahedron we flipped. If we find such a violated odd tetrahedron, we find which of its even neighbors could be flipped to fix the violation. We randomly choose one of those tetrahedra and flip it. We repeat this procedure until there are no more violated odd tetrahedra. In order to avoid flipping the entire sublattice, we bias the "coin flip" to give preference to flips that propagate in one certain direction. I.e., if the first flipped tetrahedron was at $\mathbf{r}_1 \equiv 0$ and the second one at $\mathbf{r}_2$, we give preference to flips $\mathbf{r}_i$ with large $|\mathbf{r}_i \cdot \mathbf{r}_2|$. Note that, from Sec. 3.4

we know that the flipped cluster must be unbounded in, at least, one direction.

2. Finding all distinct states (*find_distinct_states* function): if we find *gauge_count[0]* even transformations and *gauge_count[1]* odd transformations, then the total number of transformations to apply is

$$(gauge\_count[0] + 1) \times (gauge\_count[1] + 1)\,.$$

Here we included the null transformation as well as the generated transformations. We do not consider the global spin flip (which is both odd and even) as a valid transformation. We compare each new state to previously found ones by employing lattice symmetry operations (essentially identical to the function *same_as* in *state_gen.c* as described in C.1, but on the direct lattice). We save and display any distinct state found.

C.3 Monte Carlo algorithm for the large-N calculation

We use a Metropolis algorithm to search for large-N ground states. This is based on the *state_gen* program described in C.1: we start from an initial state, and generate new states by flipping random loops (using the *random_flip* function). At each step we evaluate the large-N energy $E_{\rm new}$ using the effective Hamiltonian (7.15), and decide whether to keep the state or not based on the Metropolis rule: we accept the state if a random number between 0 and 1 is smaller than $\exp[-\beta(E_{\rm new} - E_{\rm old})]$, where $E_{\rm old}$ is the energy of the previously accepted state, and β is a dimensionless inverse temperature, which we can set either to a constant (typically between 10^4 and 10^6 for the large-N problem), or we can anneal, i.e. start from high temperature (small β) and then incrementally reduce the temperature until no more changes occur. Thus we always keep states that lower the

energy, and occasionally keep states whose energy is slightly above the previous energy. In all cases, we print out all of the accepted energies and states to see if we encountered any interesting states along the way. With a good choice of temperature we generally find the ground state for a given unit cell within a few thousand loop flips.

Appendix D

Decoupling the quartic Hamiltonian

The anharmonic Hamiltonian $\mathcal{H}_{\rm quart}$ [Eq. (6.2)] contains quartic terms whose expectation value we would like to calculate. Since we only know how to calculate two-operator correlations of the form $\langle \sigma_i^{x/y} \sigma_j^{x/y} \rangle$ (within a harmonic theory), we should decouple the expectation of quartic terms to products of two-point correlations.

$$\langle \sigma_i^a \sigma_j^b \sigma_k^c \sigma_l^d \rangle = \langle \sigma_i^a \sigma_j^b \rangle \langle \sigma_k^c \sigma_l^d \rangle + \langle \sigma_i^a \sigma_k^c \rangle \langle \sigma_j^b \sigma_l^d \rangle + \langle \sigma_i^a \sigma_l^d \rangle \langle \sigma_j^b \sigma_k^c \rangle \,, \tag{D.1}$$

We are allowed to write Eq. (D.1) because two conditions are satisfied [1]:

1. The spin deviation operators $\{\sigma_i^x\}$ and $\{\sigma_i^y\}$ are linear combinations of the canonical boson operators $\{a_i\}$ and $\{a_i^\dagger\}$.

2. The expectation values are taken with respect to a harmonic Hamiltonian [in our case, the variational Hamiltonian $\mathcal{H}_{\rm var}$, given by the matrix (6.6)].

There is one subtlety to this decomposition: In order for Eq. (D.1) to be correct, we must define some "normal ordering" of the operators with respect to their indices [1]. Since the spin deviation operators commute with respect to their site indices [i,j,k,l in (D.1)], we need only order the spatial index, i.e. $a \leq b \leq c \leq d$ (where by convention $x < y$).

However, in the case of the quartic Hamiltonian (6.2), any additional terms that arise from bringing $\mathcal{H}_{\rm quart}$ to normal order have zero expectation value. For example

$$\begin{aligned} \langle \sigma_i^x \sigma_j^y \sigma_j^x \sigma_j^y \rangle &= \langle \sigma_i^x \sigma_j^x \left(\sigma_j^y\right)^2 \rangle - iS\eta_j \langle \sigma_i^x \sigma_j^y \rangle \\ &= \langle \sigma_i^x \sigma_j^x \left(\sigma_j^y\right)^2 \rangle = \langle \sigma_i^x \sigma_j^x \rangle \langle \left(\sigma_j^y\right)^2 \rangle \,. \end{aligned} \tag{D.2}$$

Thus we are free to decouple the quartic Hamiltonian $\mathcal{H}_{\text{quart}}$ to the form (6.2) as if the operators σ_i^x and σ_i^y commuted.

BIBLIOGRAPHY

[1] X.-G. Wen, in *Quantum field theory of many-body systems* (Springer-Verlag, New York, 1994), Chap. 3.

Appendix E

The functional form of Γ_{ij}

In Ch. 6, we write the mean-field Hamiltonian in terms of bond variables $\{\Gamma_{ij}\}$, defined as

$$\Gamma_{ij} \equiv G_{ii} - \eta_i \eta_j G_{ij} \,, \tag{E.1}$$

where $G_{ij} = \langle \sigma_i \sigma_j \rangle$. We also asserted, that for any state, the dominant term in Γ_{ij} (due to the bare Harmonic Hamiltonian) has the form

$$\Gamma_{ij} = \Gamma^{(0)} + \eta_i \eta_j \Gamma^{(2)} \,. \tag{E.2}$$

[Recall that this was used in Sec. 6.1.4 to argue for a particular form of the self-consistent variational Hamiltonian.]

Here, we motivate Eq. (E.2) by calculating the contribution to Γ_{ij} that comes from *ordinary modes*.

E.1 Ordinary modes reminder

The concept of ordinary modes was first introduced in Sec. 3.1. Here we review the ideas that are relevant to our current derivation. An ordinary mode $\mathbf{v}_m$, is a mode that can be written (in matrix notation) as

$$\mathbf{v}_m = \boldsymbol{\eta} \mathbf{W}^\dagger \mathbf{u}_m \,. \tag{E.3}$$

Here $\mathbf{W}$ is the $N_s/2 \times N_s$ matrix whose (α, i) element is 1 if site i belongs to tetrahedron α, and 0 otherwise. $\mathbf{u}_m$ is a *diamond-lattice spin-wave mode*. It is an eigenvector of length $N_s/2$ of the diamond-lattice spin-wave equation

$$\mathbf{W} \boldsymbol{\eta} \mathbf{W}^\dagger \mathbf{u}_m = \lambda_m \mathbf{u}_m \,. \tag{E.4}$$

Recall that by writing the spin-wave equation on the diamond-lattice we ignore half of the spin-wave modes that have 0 frequency (the *generic zero modes*), but retain the divergent-zero-modes (which, along with modes close to them, dominate correlations G_{ij} (and Γ_{ij}).

The reason that we focus on ordinary modes is that, unlike generic zero-modes, we know how they transform under gaugelike transformation. This, as we shall see below, is the key to determining the correlations. Furthermore, there is reason to believe that close to the divergence lines, the zero modes' correlations mirror the ordinary modes' correlations and therefore do not affect the form of Γ_{ij}.

The correlation function G_{ij} was shown in Sec. 2.3 to be written as a sum over the spin-wave modes

$$G_{ij} = \sum_m \frac{S}{2|c_m|} v_m(i) v_m(j)\,. \tag{E.5}$$

Here c_m is the "norm" of $\mathbf{v}_m$: $c_m = \mathbf{v}_m^\dagger \boldsymbol{\eta} \mathbf{v}_m$. Limiting ourselves to the contribution of ordinary modes (denoted henceforth by a prime) we find

$$\begin{aligned} G'_{ij} &= \sum_m{}' \frac{S}{2|c_m|} \eta_i \eta_j [u_m(\alpha_{\rm odd}(i)) + u_m(\alpha_{\rm even}(i))][u_m(\alpha_{\rm odd}(j)) + u_m(\alpha_{\rm even}(j))] \\ &= \eta_i \eta_j \left\langle (\sigma_{\alpha_{\rm odd}(i)} + \sigma_{\alpha_{\rm even}(i)})(\sigma_{\alpha_{\rm odd}(j)} + \sigma_{\alpha_{\rm even}(j)}) \right\rangle \end{aligned} \tag{E.6}$$

Where $\alpha_{\rm even}(i)$, $\alpha_{\rm odd}(i)$ are the even and odd tetrahedra to which site i belongs, respectively. We defined, in analogy with (E.5)

$$\langle \sigma_\alpha \sigma_\beta \rangle = \sum_m{}' \frac{S}{2|c_m|} u_m(\alpha) u_m(\beta)\,. \tag{E.7}$$

We are only interested in correlations of the form (E.1), for nearest-neighbors (ij). We assume, without loss of generality that $\alpha_{\rm even}(i) = \alpha_{\rm even}(j) \equiv \beta$, and obtain

$$\begin{aligned} \Gamma'_{ij} &= \left\langle (\sigma_{\alpha_{\rm odd}(i)} + \sigma_\beta)^2 \right\rangle - \left\langle (\sigma_{\alpha_{\rm odd}(i)} + \sigma_\beta)(\sigma_{\alpha_{\rm odd}(j)} + \sigma_\beta) \right\rangle \\ &= \langle \sigma^2_{\alpha_{\rm odd}(i)} \rangle + \langle \sigma_{\alpha_{\rm odd}(i)} \sigma_\beta \rangle - \langle \sigma_{\alpha_{\rm odd}(j)} \sigma_\beta \rangle - \langle \sigma_{\alpha_{\rm odd}(i)} \sigma_{\alpha_{\rm odd}(j)} \rangle\,. \end{aligned} \tag{E.8}$$

Note that the last line includes one on-(diamond)-site correlation function (on $\sigma_{\alpha_{\rm odd}(i)}$), two nearest neighbor terms, and one second-neighbor term ($\sigma_{\alpha_{\rm odd}(i)}\sigma_{\alpha_{\rm odd}(j)}$).

E.2 Using the gaugelike symmetry

Although we have been considering one particular classical configuration, we can make use of the concept of gaugelike transformations (discussed in Sec. 3.4). The important points are the following:

1. Under a gaugelike transformation that $\boldsymbol{\tau}$ ($\tau_\alpha = \pm 1$) the diamond-lattice spin-wave modes transform $u_m(\alpha) \to \tau_\alpha u_m(\alpha)$.

2. Under a gaugelike transformation $\eta_i \to \tau_{\alpha_{\rm odd}(i)}\tau_{\alpha_{\rm even}(i)}\eta_i$.

3. States that have the same products of $\{\eta_i\}$ ("flux") around each loop in the lattice are related by a gauge-transformation.

4. In particular, for states with a uniform flux arrangement, i.e., the π-flux states or the 0-flux states, there is a gauge transformation that can perform *any* lattice-symmetry operation.

5. The "norm" c_m is gauge-invariant

$$\begin{aligned} c_m &= \sum_i \eta_i (v_m(i))^2 = \sum_i \eta_i (u_{\alpha_{\rm odd}(i)} + u_{\alpha_{\rm even}(i)})^2 \\ &= \sum_i \eta_i (u^2_{\alpha_{\rm odd}(i)} + u^2_{\beta_{\rm odd}(i)} + 2u_{\alpha_{\rm odd}(i)} u_{\beta_{\rm odd}(i)}) \,. \end{aligned} \tag{E.9}$$

   The first two terms in the last line are zero (upon summation on each tetrahedron), and the last term is manifestly gauge-invariant.

The consequences of these points is that, for the π-flux states (recall that most of our interest in the anharmonic theory is to break the degeneracy among the

harmonic ground state – the π-flux states) or other states where the fluxes don't break the lattice symmetry

$$\Gamma^{(0)} \equiv \langle \sigma_\alpha^2 \rangle \qquad \text{is independent of } \alpha, \tag{E.10}$$

(since a gaugelike transformation would take α to β for any two diamond-sites α and β). Similarly, it is easy to find that for nearest neighbor (diamond) sites (sharing site i):

$$\Gamma^{(1)} \equiv \eta_i \langle \sigma_{\alpha_{\rm odd}(i)} \sigma_{\alpha_{\rm even}(i)} \rangle \qquad \text{is independent of } i, \tag{E.11}$$

and for next-nearest-neighbor (diamond) sites, connected by bond (ij):

$$\Gamma^{(2)} \equiv -\eta_i \eta_j \langle \sigma_{\alpha_{\rm odd}(i)} \sigma_{\alpha_{\rm odd}(j)} \rangle \qquad \text{is independent of } (ij), \tag{E.12}$$

Here, the sign was set so that $\Gamma^{(2)}$ would be positive. Plugging these into (E.8), we obtain

$$\Gamma'_{ij} = \Gamma^{(0)} + (\eta_i - \eta_j)\Gamma^{(1)} + \eta_i \eta_j \Gamma^{(2)} \,. \tag{E.13}$$

Since Γ'_{ij} must be invariant under a global spin-flip, we must have $\Gamma^{(1)} = 0$ and we obtain Eq. (E.2). It should be noted that $\Gamma^{(0)}$ and $\Gamma^{(2)}$ are both infinite in the bare harmonic theory. We can regularize them using a variational Hamiltonian, as in Sec. 6.1, which would add an additional, bond-dependent term (see Eq. (6.15)), but the dominant contribution would remain of the form (E.2).

E.3 Quartic breaking of gaugelike symmetry?

In the previous section, we used the properties of the gauge transformation to study the relations between correlations on different sites or bonds, in the same state. We could attempt to use the same ideas to study the relation between different

gauge-equivalent states. After all, $\Gamma^{(0)}$ and $\Gamma^{(2)}$ were argued above to be gauge invariant. Unfortunately, we could not break the harmonic degeneracy in this way – the mean-field energy (6.9) is trivially gauge-invariant, if one plugs (E.2) into it.

$$\begin{aligned} E_{\mathrm{MF}} &= -\sum_{\langle ij \rangle} \eta_i \eta_j \left(\Gamma_{ij} + \Gamma_{ji} - \frac{1}{S^2} \Gamma_{ij} \Gamma ji \right) \\ &= -\sum_{\langle ij \rangle} \left[\left(2\Gamma^{(0)} - \frac{\Gamma^{(0)})^2 + (\Gamma^{(2)})^2}{S^2} \right) \eta_i \eta_j \right. \\ &\quad \left. +2 \left(\Gamma^{(2)} - \frac{\Gamma^{(0)} \Gamma^{(2)}}{S^2} \right) \right] \\ &= N_s \left(2(\Gamma^{(0)} - 3\Gamma^{(2)}) - \frac{\Gamma^{(0)})^2 + (\Gamma^{(2)})^2 - 6\Gamma^{(0)} \Gamma^{(2)}}{S^2} \right) \end{aligned} \tag{E.14}$$

So what breaks the gauge invariance? We have not been able to obtain a good analytic understanding of this, but we believe that the reason is that, as the variational Hamiltonian is not gauge-invariant, the regularization introduces small gauge-dependent terms into $\Gamma^{(0)}$ and $\Gamma^{(2)}$. Further study would be required to understand this effect.

Note that in the entire discussion, we have ignored the generic zero modes. These modes may be as important as the ordinary modes in studying subtle degeneracy breaking phenomena.

Appendix F

Upper and lower bounds on $\mathcal{P}_6$

In Ch. 6, we found an effective Hamiltonian in terms of the loop variables $\{\mathcal{P}_l\}$, where $\mathcal{P}_l$ is the number of loops of length l, whose bonds are AFM (i.e. the Ising variables $\{\eta_i\}$ alternate along the loop). We found empirically that the quartic spin-wave energy is lowest, among the harmonic ground states (π-flux states), for $\mathcal{P}_6 = N_s/3$ and highest for $\mathcal{P}_6 = N_s/6$. In the following we will show, that for π-flux states, these are rigorous bounds for $\mathcal{P}_6$.

First, we must note that for a given hexagon (in a π-flux state), the number of AFM bonds can be 6 (for spins $\uparrow\downarrow\uparrow\downarrow\uparrow\downarrow$), 4 ($\uparrow\uparrow\downarrow\downarrow\uparrow\downarrow$), or 2 ($\uparrow\uparrow\uparrow\uparrow\uparrow\downarrow$ or $\uparrow\uparrow\uparrow\downarrow\downarrow\downarrow$). If we call the fraction of these respective arrangements n_6 (equal to $\mathcal{P}_6/N_s$, where N_s is the number of lattice sites) n_4, and n_2, then these number must satisfy

$$n_2 + n_4 + n_6 = 1\,. \tag{F.1}$$

Also, because the number of AFM bonds in any arrangement is twice the number of FM bonds, and each bond belongs to the same number (2) of hexagons

$$n_2 = n_6\,. \tag{F.2}$$

The hexagons in the lattice are arranged in supertetrahedra. If one tries to construct all of the possible (π-flux) bond arrangements, one finds that a single supertetrahedron can have one of four arrangements:

(a) Two AFM hexagons and two hexagons with 4 AFM bonds.

(b) One AFM hexagon and three hexagons with 4 AFM bonds.

(c) One AFM hexagon, one hexagon with 4 AFM bonds, and two hexagons with 2 AFM bonds.

(d) Two Hexagons with 2 AFM bonds and two hexagons with 4 AFM bonds.

We choose a subset of non-overlapping supertetrahedra (i.e. choose half of the supertetrahedra, such that they do not share any hexagons)[1] and call the number of the supertetrahedra (within this subset), of types (a), (b), (c), (d) $n_a \times N_s$, $n_b \times N_s$, $n_c \times N_s$, and $n_d \times N_s$, respectively. These number must satisfy the relations

$$n_a + n_b + n_c + n_d = \frac{1}{4}\,, \tag{F.3}$$

and

$$2n_c + 2n_d = n_2 = n_6 = 2n_a + n_b + n_c\,. \tag{F.4}$$

Examining the constraints (F.3) and (F.4), it is not hard to find that the maximum value of n_6 is $1/3$ (for $n_c = 1/6$, $n_a = 1/12$, and $n_b = n_d = 0$) and the minimum value is $N_6 = 1/6$ (for $n_d = 1/12$, $n_b = 1/6$, and $n_a = n_c = 0$). Thus we find that, for π-flux states

$$\frac{N_s}{6} \leq \mathcal{P}_6 \leq \frac{N_s}{3}\,. \tag{F.5}$$

What if we looked for bounds on $\mathcal{P}_6$ among all collinear configurations, not just π-flux states? The lower bound is clearly $\mathcal{P}_6 = 0$, since the 0-flux states have no AFM hexagons. As for the upper bound, we can repeat the arguments above, limiting ourselves to supertetrahedra that have at least one AFM hexagon. Thus we set n_d, as well as other, new arrangements with no AFM hexagons to zero. All of the supertetrahedron arrangement that have AFM hexagons still fall into type (a), (b) or (c) above, and thus, just as before $\mathcal{P}_6 = N_s/3$ is the maximum possible value. This is in agreement with the empirical findings in Ch. 7 (recall that in the large-N theory we use slightly different variables, but for hexagons $\tilde{\mathcal{P}}_6 \equiv \mathcal{P}_6$).

[1]Recall that the hexagon centers form a pyrochlore lattice (the complementary lattice), and thus the supertetrahedra centers form a diamond lattice. Choosing a non-overlapping subset corresponds to working with only one of the two diamond sublattices.